

國立臺灣大學工學院材料科學與工程學系(所)

博士論文

Department of Materials Science and Engineering

College of Engineering

National Taiwan University

Doctoral Dissertation

以含有弱介面之韌化相韌化脆性陶瓷之研究
Study on Toughening Brittle Ceramic by Using
Reinforcements with Weak Interfaces



靳元良

Chin, Yuan-Liang

指導教授：段維新 博士

Advisor: Tuan, Wei-Hsing, Ph.D.

中華民國一百年三月

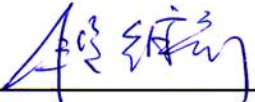

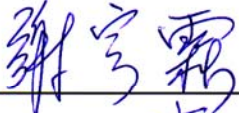


March, 2011

國立臺灣大學博士學位論文 口試委員會審定書

論文中文題目：以含有弱介面之韌化相韌化脆性陶瓷之研究

論文英文題目：Study on Toughening Brittle Ceramic by Using Reinforcements with Weak Interfaces

本論文係靳元良君 (D94527004) 在國立臺灣大學材料科學與工程學系、所完成之博士學位論文，於民國 100 年 03 月 21 日承下列考試委員審查通過及口試及格，特此證明

口試委員：段維新 
(指導教授)
黃肇瑞 
謝宗霖 
郭錦龍 
林博文 

系主任、所長 高振宏  (簽名)

致謝

時光荏苒，在台大五年多的時光即將告一個段落。漫長的學生生涯終於走到了終站。這一路以來的經歷有高有低，卻實難用簡短的篇幅述說自己的感受於萬一。首先要致上最誠摯的感謝於我的指導教授：段維新教授。老師總是在研究上給予我最大的包容以及幫助，在研究上遇到瓶頸的時候也適時的提點我。另外，因為老師的支持，讓我在博士班求學期間能有兩度前往德國進行研究的機會，更加開闊了我的視野。即便學業方面告了一段落，但老師的學者風範是我們身為學生一輩子的學習榜樣。

在博士論文計畫與學位口試期間，承蒙恩師黃肇瑞教授、謝宗霖教授、郭錦龍教授、林博文博士諸多的提點與建議，學生在此獻上無限的感激。2006年在德國柏林實習期間，感謝我的長官 Mr. Udo Brückner 各方面的照顧。2009-10年在德國漢堡的研究期間就像用不同發酵法所釀造的啤酒一樣有甘有苦，感謝指導教授 Prof. Dr. Gerold Schneider 給我的諸多磨練與指導。也要感謝那段日子幫忙我非常多的同事 Dr. Hans Jelitto, Hüso, Henry, Fung，以及國科會駐德科技組彭雙俊組長，張揚展秘書，劉綺君小姐在生活上的各項幫忙。Vielen Dank!

在研究生活中，如果沒有 CMC Lab.的各位一同打拼與互相幫忙是舉步維艱的。感謝一直以來非常關心與幫助我的學長姐劭儒、炤佑、雅任、秀菁、書廷、育祐、盈樺，好戰友昌儒，以及學弟妹劭寬、哲原、岳翰、仲瑀、宇晴、鈞禾、

浩緯、琬純、喬瑋、昕愷、君郁。也非常感謝系辦林由莉小姐、張瑛梅小姐、呂碧玲小姐、周麗美小姐，金相實驗室吳福訓先生、張順章先生、李玉玲小姐的一切幫忙。另外，由於實驗的關係常常需要南下借用儀器，感謝 CCLab.的老伙伴文蹟、尚南的諸多幫忙與建議；常常讓我借住與協助一系列 Nano-indentation 分析的建龍；幫忙進行熱壓燒結的京桓；以及常常充當司機的老室友政學、敦文。

謝謝！

回到台北的這五年多以來，特別感謝怡音學姐、家禹學長與台北當代室內合唱團的伙伴們，我們一起經歷了這個團的點點滴滴將會永存我心。感謝龍杰、道仁、瑋芳、子苡與和平教會希慢詩班、社青團契的所有兄弟姐妹們一同萬事互相效力，叫愛神的人得益處。能在這段期間認識上帝，是我一輩子最寶貴的事。這趟旅程的艱辛雖然不一定能被外人所瞭解，但聖經上有云：『你們務要堅固，不可搖動，常常竭力多作主工，因為知道你們的勞苦，在主裡不是徒然的。』未來的日子裡，仍要憑著這份信心，在家庭中與職場上繼續作光作鹽。

最後，要將這份得來不易的成果與養育我的父母親、家人們、親愛的J以及今年榮歸天家的外公一同分享。將一切的感恩與榮耀歸於天父上帝。

靳元良 28.03.2011 于台大

摘要

為了改善陶瓷材料先天的脆性，在過往二、三十年陶瓷基複合材料研究當中，起初添加金屬強化相作為研究，但因金屬材料的熔點較低而限制了其應用面。在陶瓷韌化材方面，一般添加強度、硬度較高的顆粒、鬚晶及板晶等，但韌性的提升效果有限。本研究主要為提供一個新的陶瓷韌化概念，以強度相較於基地相較低，但含有弱介面之層狀陶瓷韌化材作為第二相，利用其層間弱介面的特性，使得脆性的陶瓷材料在破壞時破壞能量由此韌化材的層間弱介面吸收而產生韌化。

本研究使用三種材料系統，分別以氧化鋁與硼矽酸鹽玻璃基低溫共燒陶瓷 (LTCC) 作為基材，添加積層陶瓷電容 (MLCC) 以及碳化鈦矽 (Ti_3SiC_2) 層狀陶瓷作為韌化相進行無壓或熱壓燒結成試樣，進行強度與韌性的量測，確立強韌化機制，並輔以理論計算。此外，也以 X 光與奈米壓痕技術分析試樣內部的應力對於強度韌性之影響。有別於一般陶瓷基複合材料在基地相與第二相間的裂縫轉折或架橋，此一特殊的韌化機制的設計使得裂縫在含有弱介面的第二相內部產生轉折而吸收破壞能，可更進一步的改善陶瓷材料的韌性。

關鍵字：陶瓷基複合材料；弱介面；韌化機制；破壞能。

Abstract

Since ceramic materials have various advantages to demonstrate their functions, they can be applied in many areas. However, ceramics are brittle and show catastrophic failure. The objective of many researches on structural ceramics is the development of materials with high reliability. Low-cost ceramic composite materials that exhibit excellent mechanical properties have attracted considerable interest for advanced engineering applications. For such materials, toughening remains one of the most important issues in enhancing the reliability.

In the present study, three different kinds of ceramic-matrix composites are used as model systems to demonstrate the feasibility of using toughening agents with weak interfaces as a new approach. The reinforcements, such as BaTiO₃ platelet containing weak interfaces and Ti₃SiC₂ compound can be incorporated to toughen the composite. The material selection is based on the higher thermal expansion coefficient and the lower elastic modulus of the reinforcement than those of the matrix. The toughening mechanism and the energy dissipation during crack propagation are investigated via different skills, such as residual stress analysis and nano-indentation. The role of the shape of the reinforcement and the effect of pullout during toughening is also discussed with theoretical calculation.

Keywords: Weak interface; BaTiO₃ platelet; Ti₃SiC₂; Residual stress;

Nano-indentation; Pullout.



Content

致謝	
摘要	I
Abstract	II
List of Tables	VI
List of Figures	VII
Chapter 1: Objective and Outline	1
Chapter 2: General Theory	4
2.1 Biomimetic concept	4
2.2 Toughening mechanisms of ceramic-matrix composites	7
2.3 Fracture toughness measurement	11
2.3.1 Single edge notched beam (SENB) method	13
2.3.2 Single edge V-notched beam (SEVNB) method	15
2.3.3 Indentation method	19
2.4 X-ray residual stress analysis [30]	19
2.4.1 Introduction of residual stress	19
2.4.2 Principles of X-ray stress measurement	21
Chapter 3: Feasibility Study of Using Multilayer Platelet as Toughening Agent	27
3.1 Introduction	27
3.2 Experimental Procedures	28
3.2.1 Raw material	29
3.2.2 $Al_2O_3/BaTiO_3$ -platelet composite	29
3.3 Results	32
3.4 Discussion	39
3.5 Conclusions	44
Chapter 4: Crack Extension Resistance Behaviour in Lamellae Inclusions Toughened Ceramic-Matrix Composite	46
4.1 Introduction	46
4.2 Experimental Procedures	47
4.2.1 Raw material	47
4.2.2 LTCC/ $BaTiO_3$ -platelet composite	47
4.3 Results	48
4.4 Discussion	50
4.5 Conclusions	59
Chapter 5: Toughening Alumina with Layered Ti_3SiC_2 Inclusions	61

5.1 Introduction.....	61
5.2 Experimental Procedures	65
5.2.1 Samples preparation	65
5.2.2 Phase and structure analysis	65
5.2.3 Bulk mechanical properties	66
5.2.4 Nanoindentation tests.....	67
5.2.5 Crack-extension-resistance behaviour(R-curve) tests	69
5.3 Results.....	70
5.3.1 Phase analysis and physical properties	70
5.3.2 Mechanical properties	72
5.3.3 Residual stress analysis	78
5.3.4 Nanoindentation results	82
5.3.5 R-curve measurements	90
5.4 Discussion	93
5.4.1 Strengthening mechanism	93
5.4.2 Toughening mechanism	94
5.4.3 Contribution of plastic deformation of Ti_3SiC_2 to the crack deflection in the Al_2O_3/Ti_3SiC_2 composites	98
5.4.4 Contribution of crack-deflection-induced pullouts to the toughening effect in Al_2O_3/Ti_3SiC_2 composite	105
5.5 Conclusions.....	115
Chapter 6: Conclusions	119
Chapter 7: Future Work	122
References.....	124
Curriculum Vitae.....	136

List of Tables

Table 3-1. The EDX results for positions 1, 2, and 3 in Fig. 3-3 and the corresponding phases.....	36
Table 3-2. Elastic modulus, hardness and fracture energy (W_{tot}) for the phases in the $Al_2O_3/7$ wt% $BaTiO_3$ -platelet composite as determined by using the nano-indentation technique.....	38
Table 3-3. Residual stress, strength and toughness of $Al_2O_3/BaTiO_3$ -platelet composites. The elastic modulus and Poisson's ratio used to calculate the residual stress are also shown.	41
Table 3-4. Anisotropic toughening effect near a platelet.....	45
Table 4-1. Apparent density, elastic modulus and Poisson's ratio of LTCC and LTCC/ $BaTiO_3$ -based platelet composites.....	51
Table 4-2. The value of the indent load to the corresponding crack size for the composites sintered at $900^\circ C$	58
Table 5-1. Reported toughness increase values for the $Al_2O_3/20$ vol% Ti_3SiC_2 composite [55-57].	64
Table 5-2. Relative density, elastic constants and residual stress of monolithic Al_2O_3 and Al_2O_3/Ti_3SiC_2 composites.....	73
Table 5-3. Localized elastic modulus, hardness and fracture energy of the Al_2O_3 matrix and Ti_3SiC_2 inclusion in the composites as determined by nano-indentation.	84
Table 5-4. Microstructure characteristics and mechanical properties of monolithic Al_2O_3 and Al_2O_3/Ti_3SiC_2 composites. The specimens were hot-pressed at $1450^\circ C$	99

List of Figures

Fig. 2-1. A model of biocomposites. (a) A schematic diagram of staggered mineral crystals embedded in protein matrix. (b) A simplified model showing the load-carrying structure of the mineral–protein composites. Most of the load is carried by the mineral platelets whereas the protein transfers load via the high shear zones between mineral platelets. [6]	6
Fig. 2-2. Resistance-curve behavior characteristically encountered in tough ceramics: K_R is the fracture resistance and Δa is the crack advance. [15].....	8
Fig. 2-3. Seven different kinds of toughening mechanisms. [16-17].....	10
Fig. 2-4. Deflection of crack by particle($\alpha_p > \alpha_m$) and associated matrix stress. Crack moving in plane particle will first be deflected (compressive hoop stress axis in matrix is normal to crack plane). As crack moves around particles, it can be attracted to particle interface (normal to tensile radial stress axis in matrix). [19].....	12
Fig. 2-5. Schematic of the single edge notch beam toughening test.....	14
Fig. 2-6. A microscopic photograph of a notch produced by SEVNB technique.....	16
Fig. 2-7. Schematic arrangement of the sample in a four-point bending cell.....	18
Fig. 2-8. Orientation of crystal planes with respect to sample coordinate system: rotation φ about S3 and ψ about L2. [30]	25
Fig. 3-1. Morphology of dummy platelets.	30
Fig. 3-2. XRD pattern of Al_2O_3 /14 wt% $BaTiO_3$ -platelet composite hot-pressed at $1400^\circ C$	34
Fig. 3-3. (a) A typical $BaTiO_3$ -platelet in an Al_2O_3 / $BaTiO_3$ -platelet composite. (b) Interactions between an indentation-induced crack and platelet.	35
Fig. 3-4. Residual strains of monolithic Al_2O_3 and Al_2O_3 / $BaTiO_3$ platelet composites hot-pressed at $1400^\circ C$	40
Fig. 3-5. Interactions between a major crack and a weak platelet.	43
Fig. 4-1. Biaxial strength of LTCC/ $BaTiO_3$ -based platelet composites as function of platelet content.....	49
Fig. 4-2. Fracture surfaces of LTCC/ $BaTiO_3$ -based platelet composites: (a) optical microscopy for over-view, (b) SEM for close-view inside one platelet. The black arrow indicates the position of Ni electrode.	52
Fig. 4-3. Plot of indentation-fracture-strength versus indentation load for LTCC/ $BaTiO_3$ -based platelet composites.....	53

Fig. 4-4. Plot of indentation-fracture-strength versus indentation load for LTCC/BaTiO ₃ -based platelet composites compared with the former results from Chantikul et al [47]. The black solid lines are from the present work and the dotted lines are from ref. 47.	55
Fig. 4-5. Toughness curves for monolithic LTCC and LTCC/4 wt% BaTiO ₃ -based platelet composite as a function of indentation load.	57
Fig. 5-1. Morphology of the Ti ₃ SiC ₂ particles.	68
Fig. 5-2. XRD patterns for the starting Ti ₃ SiC ₂ powder and Al ₂ O ₃ /20%Ti ₃ SiC ₂ composites after hot-pressing at 1400 C and 1450°C.	71
Fig. 5-3. Typical SEM micrograph for the Al ₂ O ₃ /10%Ti ₃ SiC ₂ composite.	74
Fig. 5-4. Flexural strength of Al ₂ O ₃ /Ti ₃ SiC ₂ composites as function of Ti ₃ SiC ₂ content.	75
Fig. 5-5. Hardness of Al ₂ O ₃ /Ti ₃ SiC ₂ composites as function of Ti ₃ SiC ₂ content.	76
Fig. 5-6. Fracture toughness of Al ₂ O ₃ /Ti ₃ SiC ₂ composites as function of Ti ₃ SiC ₂ content.	77
Fig. 5-7. Fracture surface of (a) monolithic Al ₂ O ₃ and (b) (c)Al ₂ O ₃ /10 vol.%Ti ₃ SiC ₂ composites.	79
Fig. 5-8. Interactions between crack induced by indentation and Ti ₃ SiC ₂ inclusions.	80
Fig. 5-9. Relationship of residual strain and the sin ² ψ of the monolithic Al ₂ O ₃ and Al ₂ O ₃ /Ti ₃ SiC ₂ composites hot-pressed at 1400°C and 1450°C. (a) Hot-pressing at 1400°C with 10 and 20 vol.% Ti ₃ SiC ₂ addition, and (b) Hot-pressing at 1450°C with 10 and 20 vol.% Ti ₃ SiC ₂ addition.	81
Fig. 5-10. Typical load-displacement curves for (a) Al ₂ O ₃ matrix and (b) Ti ₃ SiC ₂ inclusion in the composite prepared by hot-pressing at 1450°C.	83
Fig. 5-11. Load–displacement results of Ti ₃ SiC ₂ phase in the Al ₂ O ₃ /20 vol.%-Ti ₃ SiC ₂ composite with the load from 50 mN to 1500 mN. (a) hot-pressed at 1400°C, (b) hot-pressed at 1450°C.	86
Fig. 5-12. Elastic moduli of Ti ₃ SiC ₂ phase in the Al ₂ O ₃ /20 vol.%-Ti ₃ SiC ₂ composites measured by nanoindentation with the load from 50 mN to 1500 mN, respectively.	87
Fig. 5-13. Fracture energy of Ti ₃ SiC ₂ phase in the Al ₂ O ₃ /20 vol.%-Ti ₃ SiC ₂ composite hot-pressed at 1400°C and 1450°C measured by nanoindentation with the load from 50 mN to 1500 mN. (a) W_{tot} , (b) W_e and (c) W_p , respectively.	89
Fig. 5-14. Crack-growth-resistance curves of Al ₂ O ₃ and Al ₂ O ₃ /20 vol.%-Ti ₃ SiC ₂ composite hot-pressed at 1450°C under stable-crack-growth behavior. The crack-tip toughness of alumina [71,72] are also added as references.	91
Fig. 5-15. Schematic for the interactions between crack and the reinforcement with weak internal layers. The crack is deflected within the reinforcement.	97

Fig. 5-16. Schematic for the interaction between crack and a Ti_3SiC_2 particle. The dislocations, kink-band and delamination may present within the Ti_3SiC_2 particle before the reach of the crack. The presence of delamination allows the crack to change its propagation direction. 104

Fig. 5-17. A schematic to demonstrate the pullout effect inside the rectangular lamellae structure for toughening. Left-hand side: before a crack passes; right-hand side: after a crack passes, the pullouts of lamellae consume the fracture energy and the composite is thus toughened. 108

Fig. 5-18. Microstructure of pullouts inside the $\text{Al}_2\text{O}_3/\text{Ti}_3\text{SiC}_2$ composite during crack propagation. 109

Fig. 5-19. Comparison with the theoretically expected toughness increase of $\text{Al}_2\text{O}_3/\text{Ti}_3\text{SiC}_2$ composite with 10 to 50 vol.% Ti_3SiC_2 content and the experimental results from Vickers indentation and SEVNB method with 20 vol.% Ti_3SiC_2 content. 111

Fig. 5-20. Calculation of theoretical toughness increase with constant Γ_I influenced by varying particle size g and ligament width d . Each hypothetic line includes different values of g with fixed d 113

Fig. 5-21. Microstructure of non-pullouts inside the $\text{Al}_2\text{O}_3/\text{Ti}_3\text{SiC}_2$ composite when the orientation of Ti_3SiC_2 particle is parallel to the fracture direction. 114

Fig. 5-22. A schematic of non-toughening effect inside the lamellae structure. 116

Chapter 1: Objective and Outline

The applications of ceramic materials are often limited by their brittleness. Even the toughness of ceramics can be improved by incorporating hard and strong particles, whiskers or fibers; the damage tolerance remains poor afterwards. The objective of this study is to develop a new concept of adapting reinforcement within weak interfaces into ceramic matrix in order to characterize the toughening effects and the crack resistance behavior via microstructure, internal stress analysis and nano-indentation measurements. The materials of reinforcements used for this study all contain lamellae structure, such as platelet with multilayer structure, Ti_3SiC_2 and conventional multilayer ceramic capacitor (MLCC) with inner Ni electrodes.

Chapter 2 introduces the basic toughening mechanisms of ceramic-matrix composites, the theory of residual stress analysis and also different methods of measuring the fracture toughness which were used in the present study.

Chapter 3 focuses on the first model system of $\text{Al}_2\text{O}_3/\text{BaTiO}_3$ -platelet composite. We tried to use the BaTiO_3 platelet as reinforcement to toughen the alumina matrix. The hot-pressed composite was carefully investigated by mechanical properties, residual stress analysis and also the elastic properties. Although this concept was successfully developed, due to the limit of reinforcement size, the crack branching

toughening phenomena cannot reflect the global increment of toughness. We discuss the advantages and also the disadvantages of this system in chapter 2.

In chapter 4, the BaTiO₃ platelet within Ni electrode was selected for the reinforcement added into glass ceramic matrix. The sintering temperature is lower than the former one. The difference is there is no reaction on the interface between matrix and reinforcement. The indentation-fracture-strength method is used to investigate the R-curve behavior under biaxial strength measurement.

In chapter 5, the metal-like Ti₃SiC₂ was added into alumina matrix as the toughening agent. According to its high toughness and also high elastic modulus, the toughening effects in this model are very obvious. The special toughening mechanisms of crack deflection inside the Ti₃SiC₂ and pull-outs of the lamellae ligaments in this composite are discussed from microstructure and also residual stress analysis in this chapter in detail. Due to the special nano-lamellae structure of Ti₃SiC₂ reinforcement and the radial tensile stress on Al₂O₃/Ti₃SiC₂ interface after hot-pressing, the crack will penetrate into the Ti₃SiC₂ grain and be deflected between the ligaments during crack propagation. The aspect ratio analysis of Ti₃SiC₂ grains was also investigated. The plastic deformation inside the ductile Ti₃SiC₂ grain has a minor influence on the energy absorption (dissipation) and decrease the crack propagation ability.

At last, in chapter 6, we summarize our present research and make several conclusions. Several possible future research directions are also briefly suggested in chapter 7.



Chapter 2: General Theory

2.1 Biomimetic concept

As existing structural materials reach their performance limits, one of the major scientific challenges for the 21st century is the development of new stronger and tougher lightweight structural materials to support advances in diverse application fields from building to transportation or energy. This is a challenge that can only be reached through an understanding of the relationships between materials architecture and mechanical response, spanning not only the microstructure but also the influence of structural parameters acting at multiple length scales, from the atomic to the macro levels, and their interactions. The design of this new and superior structural materials can be done by mimicking the architecture of natural/biological materials and structures [1,2]. The natural materials usually combine both inorganic ceramics and organic protein, which typically exhibit poor macroscale mechanical properties individually, to produce far stronger and tougher composites, such as enamel dentin, nacre and bone. Their superb mechanical properties have been related to their unique hierarchical structure [3,4] by shielding an extending crack from an applied load inside this hierarchical structure. From a fracture mechanics perspective, they

generate a characteristic crack resistance curve (R-curve) behavior where the fracture resistance actually increases with crack extension. In other words, this layered hierarchical structure develops the majority of its toughening during crack growth and not during crack initiation [5], which can be adapted to toughen the brittle materials, such as ceramics. A model of this kind of bio-composites is illustrated in Fig.2-1 [6].

There are two approaches to mimic the structure and to synthesize the materials. The first approach starts with the evaluation of the benefit of using natural-produced structure as engineering material, and then to find engineering solution to re-produce it (the “bottom-up” approach). However, this approach is generally difficult for making synthetic materials in practical sizes with severe time constraints. Although there are several outstanding examples of materials fabricated in the laboratory by applying physicochemical principles taken from the growth of natural composites, these are invariably limited to thin films or microscopic samples [7-11]. To solve this problem comes to the second approach (the “top-down” approach). Namely, it is to produce a biomimetic structure through novel processing first, then to determine the performance of such structure [12], but only a few systems are successful. Among these successful attempts, the freeze casting technique has attracted much attention [3,4,12,13]. This technique is capable to produce a laminated structure with layer spacing as small as only 3 μm . By using the technique, the fracture energy of an

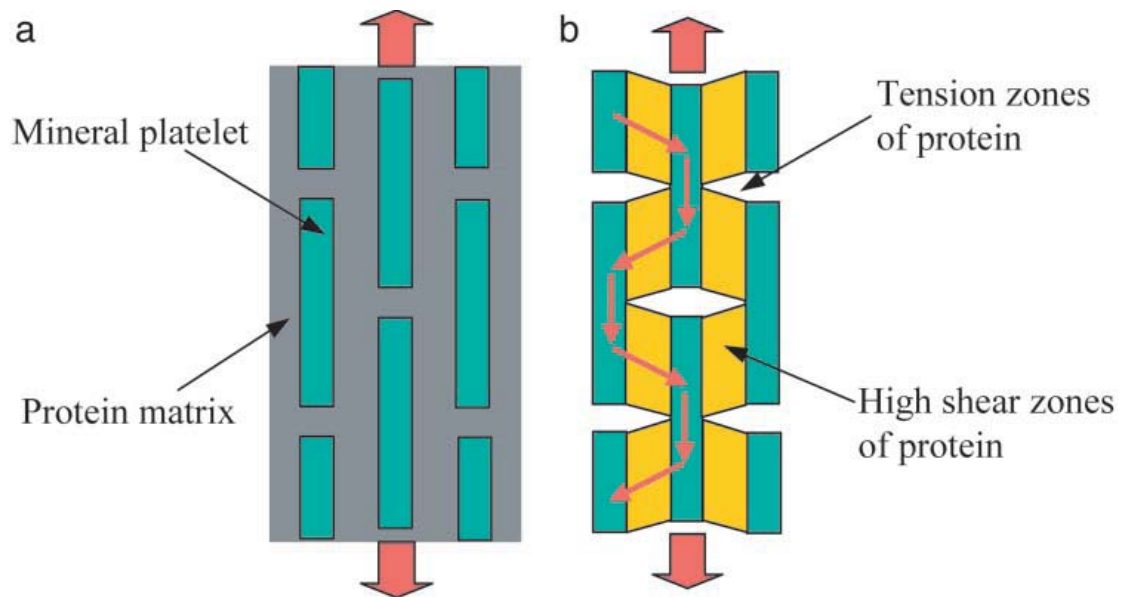


Fig. 2-1. A model of biocomposites. (a) A schematic diagram of staggered mineral crystals embedded in protein matrix. (b) A simplified model showing the load-carrying structure of the mineral–protein composites. Most of the load is carried by the mineral platelets whereas the protein transfers load via the high shear zones between mineral platelets. [6]

$\text{Al}_2\text{O}_3/\text{PMMA}$ laminate reaches 300 times that of Al_2O_3 alone, and the fracture toughness of an $\text{Al}_2\text{O}_3/\text{Al-Si}$ laminate reaches $40 \text{ MPa}\sqrt{\text{m}}$ [3,4-12-14]. In the present study, the second approach is adapted by designing different kinds of reinforcements with layered structure as toughening agents to improve brittle ceramic matrix.

2.2 Toughening mechanisms of ceramic-matrix composites

The objective of research concerned with structural ceramics is the generation of materials having high reliability. To achieve this objective, there are two fundamentally different approaches: flaw control and toughening. The flaw control approach accepts the brittleness of the material and attempts to control the large extreme of processing flaws. The toughening approach attempts to create microstructures that impart sufficient fracture resistance (Fig. 2-2), and the strength becomes insensitive to the size of flaws. [15]

The resistance of brittle solids to the propagation of cracks can be strongly influenced by their microstructure and by the use of various reinforcements. For most cases, toughening results in resistance-curve characteristics (Fig. 2-2), wherein the fracture resistance systematically increases with crack extension. The resulting material strengths then depend on the details of the resistance curve and the initial

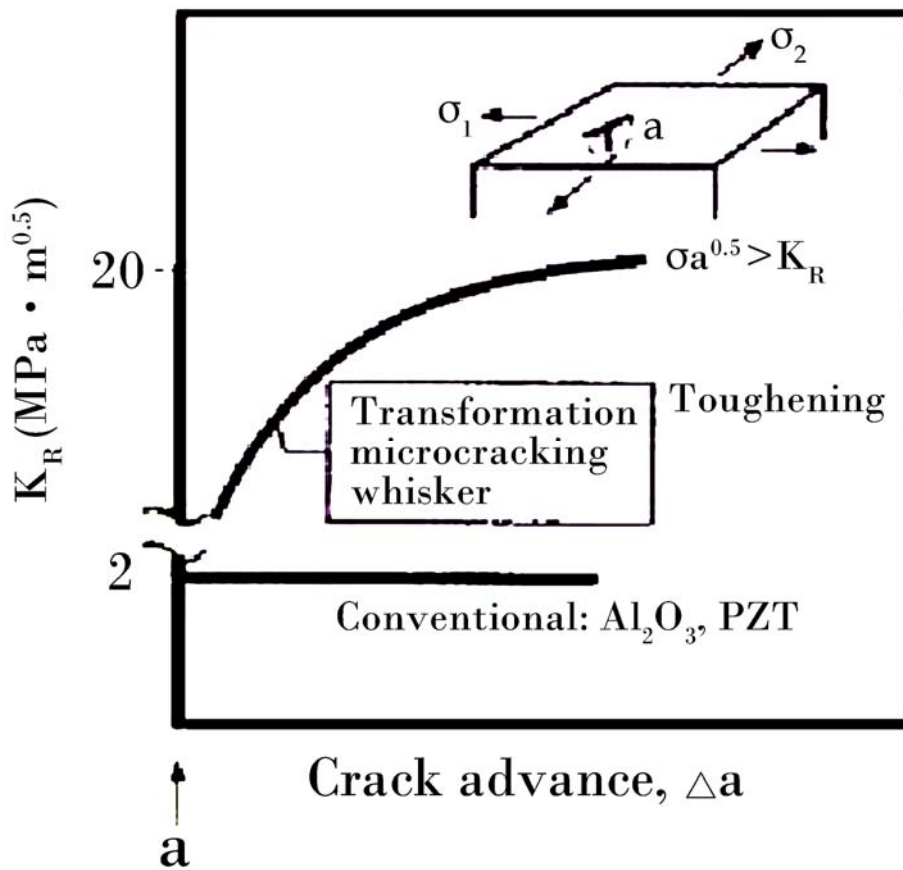


Fig. 2-2. Resistance-curve behavior characteristically encountered in tough ceramics: K_R is the fracture resistance and Δa is the crack advance. [15]

crack lengths [16-17], such that toughness and strength optimization usually involve different choices of microstructure. The general toughening mechanisms of ceramic-matrix composites include: (1) microcrack, (2) crack branching, (3) crack deflection, (4) crack bridging, (5) crack pinning, (6) transformation and (7) load transfer, which can be schematically described in Fig. 2-3. For the normal cases, several different kinds of toughening effects are involved during one toughening process. The total toughness of composite can be expressed as:

$$K^c_{IC} = K^m_{IC} + \Delta K^T_{IC} \quad (2-1)$$

Where K^c_{IC} is the total toughness of composite, K^m_{IC} is the toughness of matrix material and ΔK^T_{IC} is the sum of toughness increment by each existing toughening mechanism.

Due to the thermal expansion coefficients (CTEs) and elastic moduli for matrix and reinforcement of the composite are different, the internal stress between matrix and reinforcement will be generated after sintering process. Wei and Becher [18] addressed that the residual thermal stress inside the composite will deflect the crack. If the CTE of reinforcement is higher than that of matrix, it will produce the tensile radial stress field inside the matrix around the reinforcements. And the compressive

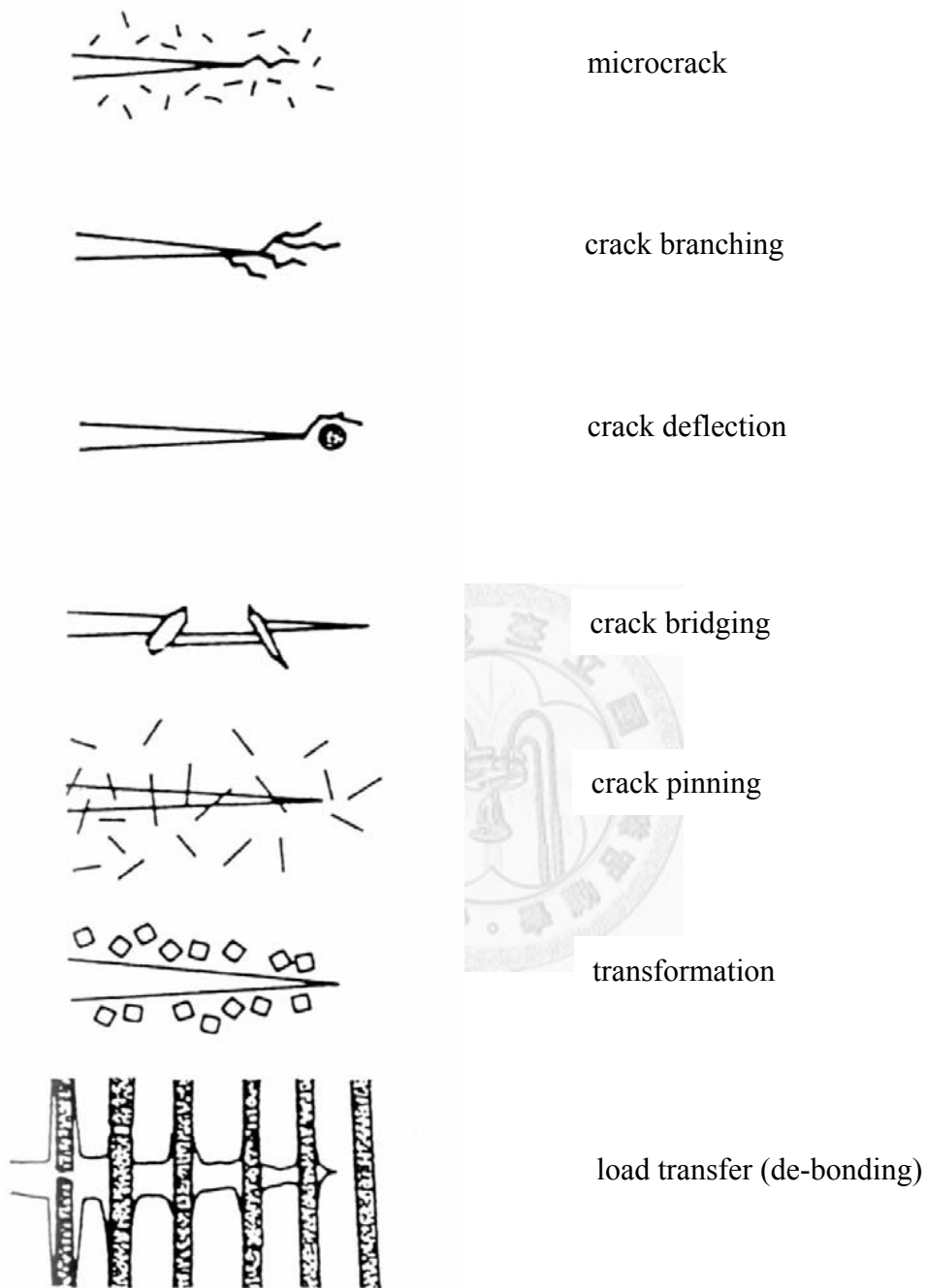
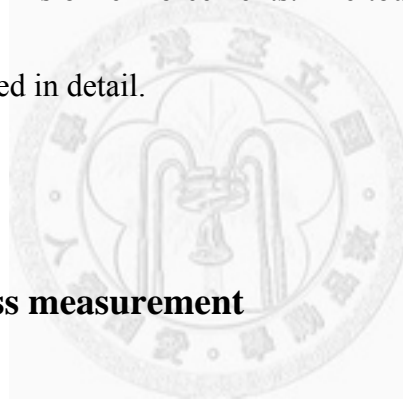


Fig. 2-3. Seven different kinds of toughening mechanisms. [16-17]

hoop stress field will penetrate through the reinforcements. When a crack propagates close to the reinforcement, it will be attracted by the tensile stress field and be deflected around the reinforcement, which is shown in Fig. 2-4. During the crack propagation, the roughness of fracture surface increases because of the deflection. This phenomenon causes the change of crack propagating direction and decreases the ability of crack extension. [19]

In the present study, we use three different kinds of ceramic-matrix composites which all include higher CTEs of reinforcements. The toughening mechanisms of the composites will be discussed in detail.



2.3 Fracture toughness measurement

Fracture toughness is an important parameter for the ability of crack-growth resistance. For brittle materials like ceramics, the value of fracture toughness is normally determined by crack length, shape and the loading system of the surface or inside the material. The following section will introduce three kinds of fracture toughness measurement methods which were used in the present study for different ceramic-matrix composite systems.

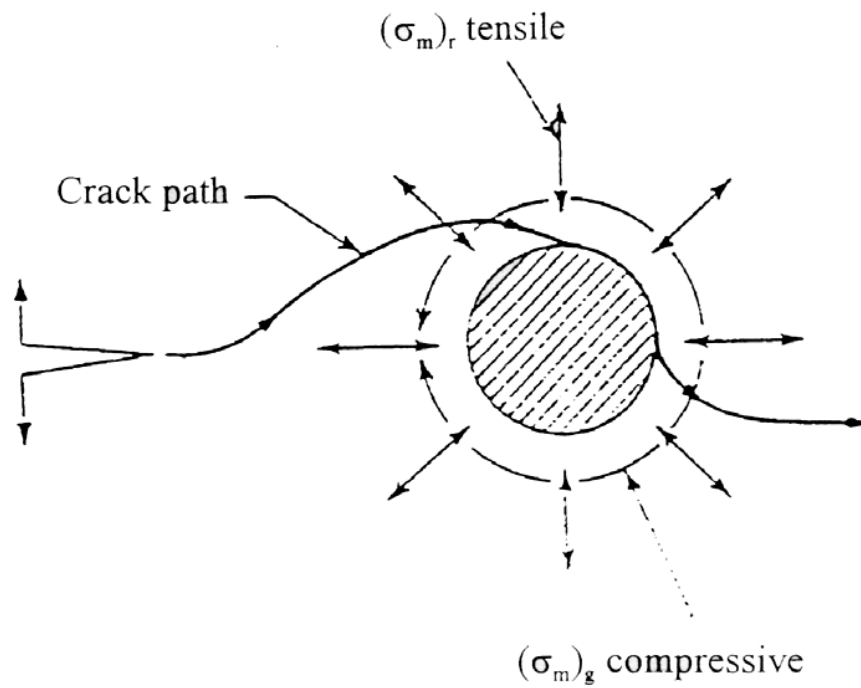


Fig. 2-4. Deflection of crack by particle ($\alpha_p > \alpha_m$) and associated matrix stress. Crack moving in plane particle will first be deflected (compressive hoop stress axis in matrix is normal to crack plane, $(\sigma_m)_g$). As crack moves around particles, it can be attracted to particle interface (normal to tensile radial stress axis in matrix, $(\sigma_m)_r$). [19]

2.3.1 Single edge notched beam (SENB) method

The most widely used fracture toughness test configuration is the single edge notched beam (SENB). The compact tension specimen has the advantage that it requires less material, but is more expensive to machine and more complex to test compared with the SENB specimen. Also, special requirements are needed for temperature control (e.g. use of an environmental chamber). The SENB specimens are typically immersed in a bath for low temperature tests. Although the compact specimen is loaded in tension, the crack tip conditions are predominantly bending (high constraint). If limited material is available, it is possible to fabricate SENB specimens by welding extension pieces (for the loading arms) to the material sample. (Electron beam welding is typically used, because the weld is narrow and causes little distortion).

The sample size for SENB test is 3 mm*4 mm*45 mm. After grinding and polishing process, a 0.15 mm thick diamond saw is used to notch the sample on the center position of tension surface during 4-pt bending test. The depth of the notch was approximately 1 mm. The width of the notch was approximately 0.3 mm. The schematic of the SENB toughening test is shown in Fig. 2-5. The fracture toughness, which measured by 4-pt-bending with rectangular shape samples, is calculated by using the following equation:

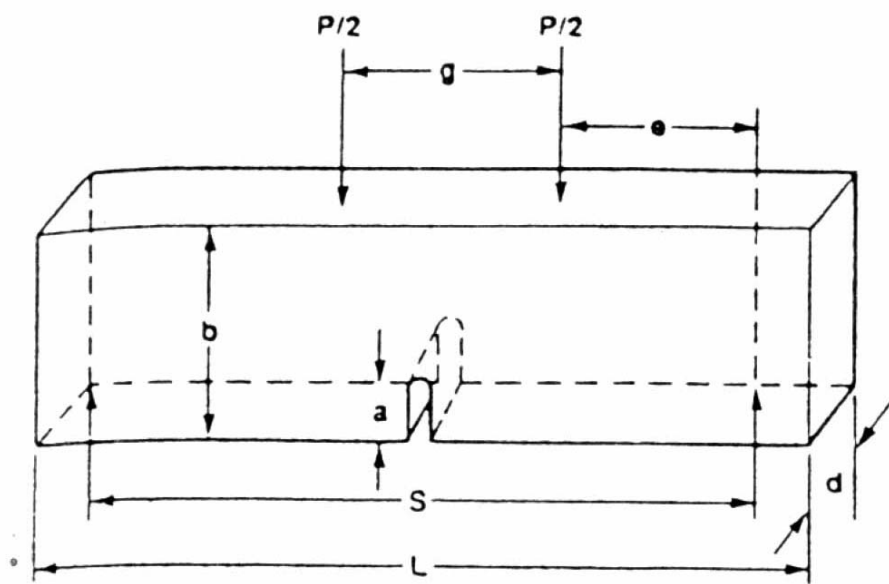


Fig. 2-5. Schematic of the single edge notch beam toughening test.

$$K_{IC} = Y\sigma\sqrt{\pi a} \quad (2-2)$$

with $Y = 1.99 - 2.47(a/b) + 12.97(a/b)^2 - 3.17(a/b)^3 + 24.8(a/b)^4$

a is the length of pre-crack, σ is the strength, Y is the shape factor and b is the height of the sample, respectively.

2.3.2 Single edge V-notched beam (SEVNB) method

The investigation made by the Christian Doppler Laboratorium für Hochleistungskeramik, Leoben, Austria, using five different fracture toughness testing methods pointed that the single edge notched beam-saw cut (SENB-S) technique seems to provide the most reproducible result [20], which involves using small beam samples, sawing a suitable notch to depth a_0 and then loading to fracture in four-point bending test.

The single edge V-notched beam (SEVNB) technique is a further modification of this method. The notch preparation is expanded with a razor blade and several kinds diamond pastes (6 μm , 3 μm and 1 μm) to sharpen the notch, as specified by Kübler [21-22], (Fig. 2-6). Therefore the notch tip radii of less than 10 μm can be produced with this technique.

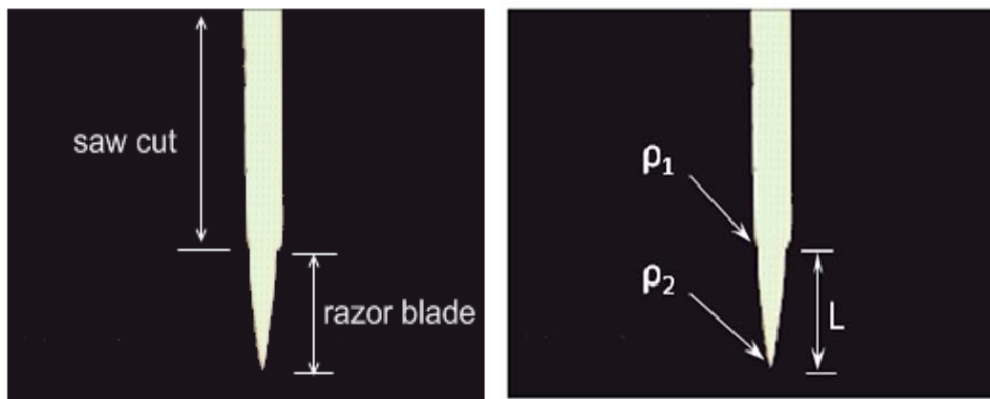


Fig. 2-6. A microscopic photograph of a notch produced by SEVNB technique.

It is important to note that the depth L produced with the razor blade and diamond pastes should be at least 1.5 times the notch radius ρ_1 produced by saw cut (Fig. 2-6, right) during the sample preparation. Otherwise, the measured toughness will be influenced not only by the notch radius ρ_2 , but possibly also by ρ_1 . After the preparation, specimens are tested in a four-point bending cell. Fig. 2-7 shows schematically the associated arrangement.

The fracture toughness, which measured by four-point-bending with rectangular profile samples, is calculated by using the following equation [23]:

$$K_{IC} = \frac{3F \Delta s \sqrt{\alpha} \Gamma_M(\alpha)}{2bh^{3/2}(1-\alpha)^{3/2}} \quad (2-3)$$

with $\Gamma(\alpha)_M = 1,1215\sqrt{\pi} \left[\frac{5}{8} - \frac{5}{12}\alpha + \frac{1}{8}\alpha^2 + 5\alpha^2(1-\alpha)^6 + \frac{3}{8} \exp\left(-6,1342 \frac{\alpha}{(1-\alpha)}\right) \right]$

$$\alpha = \frac{a}{h}$$

s is the difference of the support roller distance, b is the width, and h the height of the specimen. $\Gamma_M(\alpha)$ the geometric factor. This equation can be used to determine both the fracture toughness K_{IC} after unstable fracture, stable crack growth, and the actual stress intensity K_I at a crack length a .

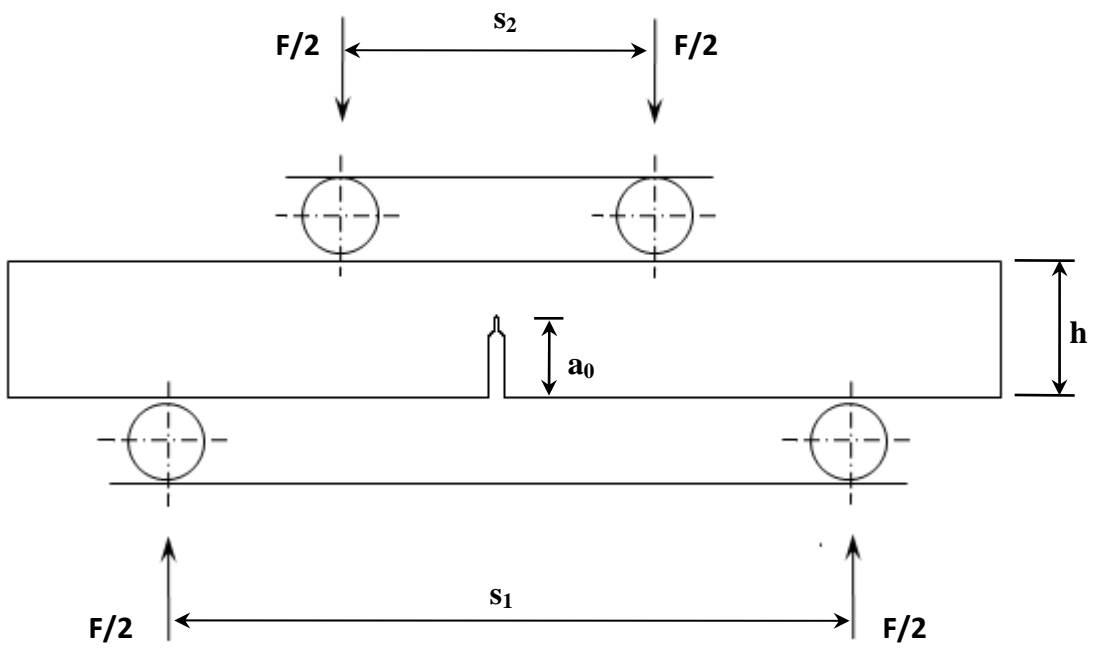


Fig. 2-7. Schematic arrangement of the sample in a four-point bending cell.

2.3.3 Indentation method

Indentation has already become the simplest technique for fracture toughness determinations for over two decades [24]. Surface cracks generated by Vickers indentation are now used extensively as model surface flaws in fracture research of brittle materials such as ceramics and glasses [25-28]. Plastic deformed zone at the center of these cracks exerts a residual crack-opening force. Such a residual stress plays an important role in the determination of the fracture toughness of brittle ceramics with indentation method. The following equation was used to calculate the toughness, K_{IC} , from one crack length as [29]:

$$K_{IC}\phi / H\sqrt{a} = 0.15k(c/a)^{\frac{3}{2}} \quad (2-4)$$

Where ϕ , k are respectively constant of 3 and 3.2, H is the hardness, a is half the indent impression length and c is the length of one crack.

2.4 X-ray residual stress analysis [30]

2.4.1 Introduction of residual stress

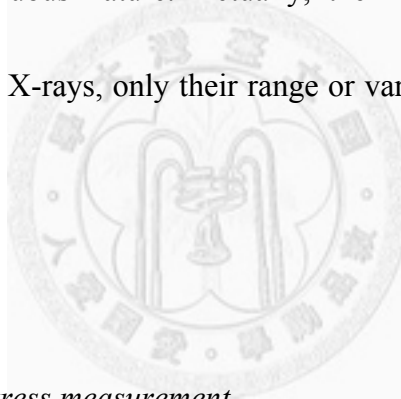
Residual stresses are those stresses that are contained in a body which has no external traction (excluding gravity or another source such as a thermal gradient). Residual stresses belong to the larger group of internal stresses which apply to a body even while it is externally loaded. The two are often used interchangeably because both may be determined with X-ray diffraction, indirectly, from a measurement of the existing strains. To obtain the value of stress, a calculation is always necessary, which requires knowledge of elastic constants of the material and a calibration procedure.

The residual stress was generally defined as three types. The first type, termed macroscopic, is long range in nature extending over regions millimeters in dimension. Macro residual stresses and applied stresses add algebraically at least up to the elastic limit and are thus important in determining load carrying capabilities. These stresses may develop from mechanical processes such as surface working, forming and assembly, thermal processes such as heat treatments, casting and welding and chemical processes such as oxidation, corrosion and electro-polishing. This class of stresses is measurable by mechanical means (by examining distortions after removing layers or boring, for example, often with strain gages) and also gives rise to shifts of peaks in an X-ray diffraction pattern.

The second kind of residual stress exists over dimensions of microns and is termed a micro-stress. It may be caused by yield anisotropy between grains or by a

difference in the mechanical properties of different phases or regions in a material (such as the surface and the interior). While not detected by mechanical methods, these stresses give rise to both a peak shift and if they vary from point to point, line broadening in X-ray patterns.

The third kind, which ranges over dimensions of 1-1000Å, gives rise to X-ray line broadening only. These stresses arise from the varying stress fields of individual dislocations, dislocation pile-ups, kink boundaries and other microstructural phenomena with discontinuous nature. Actually, the magnitude of these stresses cannot be determined with X-rays, only their range or variance from Fourier analysis of diffraction peak.



2.4.2 Principles of X-ray stress measurement

Each form of identical planes of atoms in a polycrystalline material has an average interplanar spacing, d_{hkl} , which, when acted upon by an elastic stress, changes to a new value dependent on the direction and magnitude of that stress. A change, Δd_{hkl} , in the interplanar spacing will cause a corresponding change, $\Delta\theta$, in the Bragg angle of diffraction by the planes (Bragg's law: $\lambda = 2d\sin\theta$, where λ is the wavelength of the incident X-rays). The strain $\Delta d/d$, can be measured by the change in the

diffraction angle and the stress is obtained from the strain with formulae usually derived from linear isotropic elasticity theory.

The principal stresses σ_1 , σ_2 (usually assumed to lie in the surface) and σ_3 (perpendicular to the surface) in the solid are defined as a coordinate system. It's assumed that the axes of a sample define as S1, S2 (on the sample surface) and S3 (perpendicular to the sample surface). The Axes of the X-ray diffraction are defined as L1 (σ_1), L2 (σ_2) and L3 (σ_3). L3 (σ_3) is perpendicular to the (h k l) plane. The included angle between L3 (σ_3) and S3 is defined as Ψ , and the included angle between L2 (σ_2) and S2 on the sample surface is Φ , which can be found in Fig. 2-8. The ε'_{ij} represents the strain of the coordinate system. Assume that the stress-free condition of d-spacing, d_0 , is known.

$$(\varepsilon'_{33})_{\phi\psi} = (d_{\phi\psi} - d_0) / d_0$$

The correlation between the strain and the coordinates of the sample is:

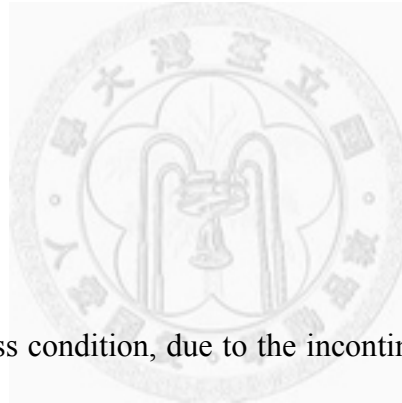
$$\begin{aligned} (\varepsilon'_{33})_{\phi\psi} = & (\varepsilon_{11} \cos^2 \phi \sin^2 \psi + \varepsilon_{12} \sin 2\phi \cos^2 \psi \\ & + \varepsilon_{22} \sin^2 \phi \sin^2 \psi + \varepsilon_{33} \cos^2 \psi \\ & + \varepsilon_{13} \cos \phi \sin 2\psi + \varepsilon_{23} \sin \phi \sin 2\psi \end{aligned} \quad (2-5)$$

The elastic theory of material assumes that the material is a homogeneous isotropic continuum material. Then $(\varepsilon'_{33})_{\phi\psi}$ can be substituted into:

$$\begin{aligned}
 (\varepsilon'_{33})_{\phi\psi} = & \frac{1+\nu}{E} \{ \sigma_{11} \cos^2 \phi + \sigma_{12} \sin 2\phi \\
 & + \sigma_{22} \sin^2 \phi + \sigma_{33} \} \sin^2 \psi + \left(\frac{1+\nu}{E} \right) \sigma_{33} \\
 & - \frac{\nu}{E} (\sigma_{11} + \sigma_{22} + \sigma_{33}) + \left(\frac{1+\nu}{E} \right) (\sigma_{13} \cos \phi + \sigma_{23} \sin \phi) \sin 2\psi
 \end{aligned} \tag{2-6}$$

E: Young's modulus

ν : Poisson's ratio



To consider the plane stress condition, due to the incontinuity of the material surface in the vertical direction, σ_{33} and all the shear stresses should be zero. Therefore, the equation (2-6) can be simplified as:

$$(\varepsilon'_{33})_{\phi\psi} = \frac{1+\nu}{E} \{ \sigma_{11} \cos^2 \phi + \sigma_{22} \sin^2 \phi \} \sin^2 \psi - \frac{\nu}{E} (\sigma_{11} + \sigma_{22}) \tag{2-7}$$

Owing to $\varepsilon_{33} = -\frac{\nu}{E} (\sigma_{11} + \sigma_{22})$ and $\sigma_{11} \cos^2 \phi + \sigma_{22} \sin^2 \phi = \sigma_{\phi}$

($\psi = 90^\circ$), the Eq. 2-7 can be replaced as:

$$\sigma_{\phi} = -\frac{E}{(1+\nu)\sin^2\psi} \{(\mathcal{E}'_{33})_{\phi\psi} - \mathcal{E}_{33}\} \quad (2-8)$$

$$(\mathcal{E}'_{33})_{\phi\psi} - \mathcal{E}_{33} = \frac{d_{\phi\psi} - d_z}{d_0} \sim \frac{d_{\phi\psi} - d_z}{d_z}; d_z \text{ is the actual plane-spacing along the S3}$$

direction. The Eq. 2-8 can be replaced as:

$$\begin{aligned} \sigma_{\phi} &= \left(\frac{d_{\phi\psi} - d_z}{d_z}\right) \frac{E}{(1+\nu)\sin^2\psi} = (2\theta_z - 2\theta_{\psi}) \times \frac{\cot\theta_z}{2} \left(\frac{E}{1+\nu}\right) \frac{1}{\sin^2\psi} \left(\frac{\pi}{180^\circ}\right) \\ &= K' \cot\theta_z (2\theta_z - 2\theta_{\psi}) \end{aligned} \quad (2-9)$$

θ_z is the X-ray diffraction angle when $\psi = 0^\circ$ and θ_{ψ} is the X-ray diffraction angle when $\psi = \psi^\circ$.

$$K' = \frac{1}{2\sin^2\psi} \left(\frac{E}{1+\nu}\right) \left(\frac{\pi}{180^\circ}\right) \quad (2-10)$$

Hence, it's necessary to measure two or more different ψ angles of d-spacing to obtain σ_{ψ} (one is at $\psi = 0$, and the other is over 45°). The incident X-ray beam is directed toward the specimen surface at a fixed angle from the surface normal, and the bisector angle of the plane normals corresponding to the two measuring directions are measured for d_{hkl} . If one measures the Bragg angle at two positions on the cone by recording the cone on film, the diffraction ring will be asymmetric if the interplanar

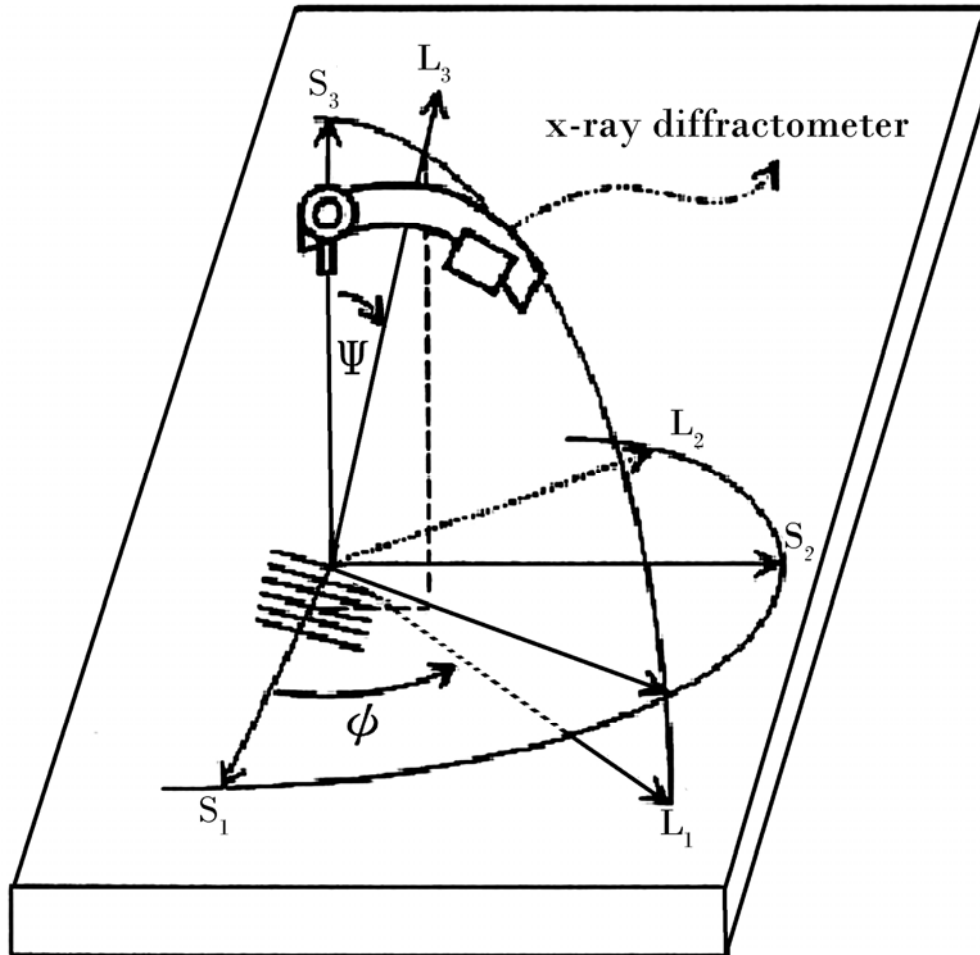
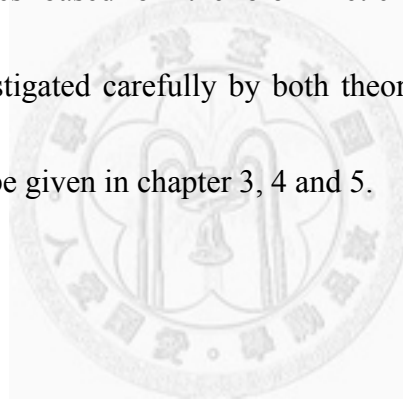


Fig. 2-8. Orientation of crystal planes with respect to sample coordinate system: The principal stresses σ_1 , σ_2 (usually assumed to lie in the surface) and σ_3 (perpendicular to the surface) in the solid are defined as a coordinate system. The axes of a sample are defined as S_1 , S_2 (on the sample surface) and S_3 (perpendicular to the sample surface). The Axes of the X-ray diffraction are defined as L_1 (σ_1), L_2 (σ_2) and L_3 (σ_3). L_3 (σ_3) is perpendicular to the (h k l) plane. The included angle between L_3 (σ_3) and S_3 is defined as Ψ , and the included angle between L_2 (σ_2) and S_2 on the sample surface is Φ . [30]

spacings of the diffracting crystallites are different as a result of residual strains. Since we do not know the directions of S1 and S2, if we want to obtain the values of σ_{11} and σ_{22} , we can use the axis of S3 (perpendicular to the surface) and pick S1 randomly for the values of σ_ϕ , $\sigma_{\phi+45}$ and $\sigma_{\phi+90}$. According to $\sigma_\phi = \sigma_{11} \cos^2 \phi + \sigma_{22} \sin^2 \phi$, the value of σ_ϕ residual stress can be obtained. In the present study, we pick 6 values of ψ angles for each composition of different composites to obtain the residual stress.

In the present work, we try to build a new landscape of toughening in the ceramic matrix composites based on the biomimetic concept. Several different material systems are investigated carefully by both theoretically and experimentally methods. The details will be given in chapter 3, 4 and 5.



Chapter 3: Feasibility Study of Using Multilayer Platelet as Toughening Agent

3.1 Introduction

The brittle nature of ceramics imposes limits on their applications as structural components. To improve the toughness of ceramics is therefore a long-standing pursuit for many ceramists. One approach adopting the addition of toughening agents, such as ceramic whiskers or platelets, has attracted a lot of attention. A triple enhancement on the toughness of alumina ceramics by adding SiC whiskers has been reported [31]. However, the health issue associated with the large aspect-ratio whiskers has prohibited further research on using of ceramic whiskers. There is no health concern for the use of ceramic platelets. Several reports had demonstrated that the toughness of ceramic matrix is improved by 10 to 50% after the addition SiC platelets or Al₂O₃ platelets, despite that the strength of the platelet-toughened ceramics is usually compromised [32-34]. However, the strength of the platelet-toughened ceramics was usually lower than that of matrix alone. Furthermore, due to the anisotropic shape of platelet, the microstructure anisotropy as well as the toughness anisotropy were observed. The shortcoming of using ceramic platelets is its

sources are very limited. The cost of the SiC and Al₂O₃ platelets is therefore relatively high.

Many passive components, such as ceramic capacitors, are in the shape of platelet. Due to the demand on the miniaturization of electronic components, the passive components nowadays are usually manufactured by employing multilayer technology [35-36]. The size of the multilayer components decreases from 1206 (0.12 inch in length and 0.06 in width; ~3.2x1.6x1.5 mm) to 0201 (~0.6x0.3x0.3 mm) in the last decade. Even smaller components, such as 01005 (~0.3x0.2x0.2 mm) components are now available. Such downsizing trend does not show any slowing down. It demonstrates that the processing technology for manufacturing multilayer components is moving forward very quickly. Furthermore, the price of multilayer components is also decreasing. To give a specific comparison, the price of 0402 (1.0x0.5x0.5 mm) multilayer capacitors (with Ni inner electrodes) per unit weight is in fact lower than that of SiC platelets. These multilayer components are in the shape of platelet, it is therefore of interest to investigate the feasibility of using multilayer components as the toughening agents.

3.2 Experimental Procedures

3.2.1 Raw material

An alumina powder (TM-DAR, Taimei Chem. Co. Ltd., Tokyo, Japan) was used to prepare the ceramic matrices in the present study. A BaTiO₃-based ceramic powder was mixed with several solvents and binders to prepare green tapes. Several tapes were laminated together and subsequently cut into small platelets. The dimensions of the green platelets were 1.28 x 0.64 x 0.41 mm, which is demonstrated in Fig. 3-1.

3.2.2 Al₂O₃/BaTiO₃-platelet composite

The Al₂O₃ powder and green dummy platelets (without inner electrodes) were dry mixed together in a PE jar for 1h. The amount of green platelets was 3, 7 and 14 wt%. The mixture was then hot-pressed in vacuum at 1400°C under a load of 25 MPa for 1 h (High-multi-5000, Fujidempa Kogyo Co., LTD., Japan). The dimensions of the hot-pressed specimens were 50 mm in diameter and roughly 4.5 mm in thickness. The phase of Al₂O₃/BaTiO₃-platelet composite was characterized with a synchrotron X-ray source (Beam-line BL-17B1 in the National Synchrotron Radiation Research Center, NSRRC, Hsinchu, Taiwan). The diffraction angle (2θ) varied from 20° to 50°. The microstructure was observed with SEM (Philips XL-30, Netherlands). Artificial

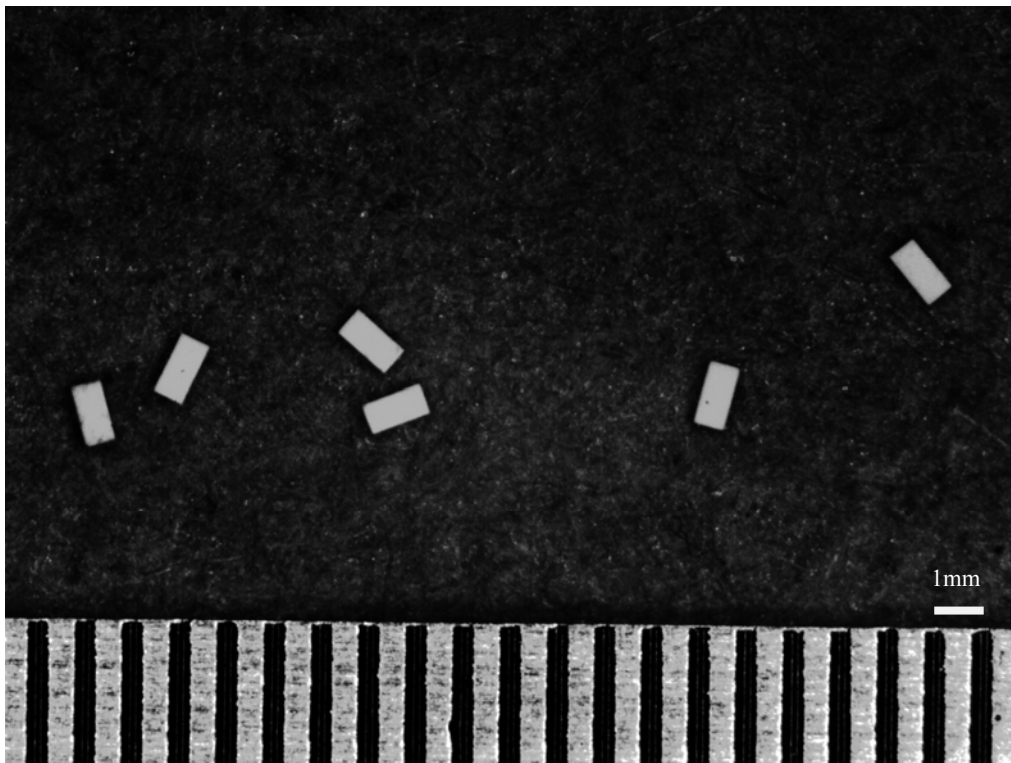


Fig. 3-1. Morphology of dummy platelets.

cracks were generated by Vickers hardness tester (AKASHI AVK-A, Japan) under a load of 98N. A nano-indenter (UNAT[®], ASMEC, Germany) was also used in the present study to determine the elastic modulus, hardness and fracture energy of each phase in the composite. The tip was a Berkovich type nano-indenter (radius = 200 nm). The load was 50 mN. The 4-point bending and single-edge-notched beam (SENB) techniques were used to determine the flexural strength and toughness of Al₂O₃/BaTiO₃-platelet composites, respectively. The indentation technique [29] was also used to determine the toughness anisotropy. The details and the used equation can be found in section 2.3.3.

The values of elastic modulus and Poisson's ratio of the bulk composites were measured by the ultrasonic reflection method [37]. A frequency of 5MHz was applied (Wavepro 7000, LeCroy Co., USA); the longitudinal velocity (V_s) and transverse (V_p) velocity within the specimens were determined as follows:

$$V_p = \sqrt{\frac{\lambda + 2\mu}{\rho}} \quad (3-1)$$

$$V_s = \sqrt{\frac{\mu}{\rho}} \quad (3-2)$$

$$E = \frac{\mu \cdot (3\lambda + 2\mu)}{\lambda + \mu} \quad (3-3)$$

$$\nu = \frac{\lambda}{2(\lambda + \mu)} \quad (3-4)$$

where λ and μ are Lamé's constants (GPa), and ρ is the density (g/cm^3); E and ν are the elastic modulus and Poisson's ratio of the bulk material.

The residual stress of the composite was measured by an X-ray diffractometer (Siemens D-5000, Germany) using the $\sin^2\Psi$ method [30]. The residual stress was calculated based on the displacement of plane spacing for different orientations of X-ray beams relative to the specimen. In the present study, several orientations including 0° , 18.43° , 26.56° , 33.21° , 39.23° , 45° were chosen and the residual stress was calculated by the following equation [30] as:

$$\sigma = \left[\frac{E}{(1+\nu)} \right] \left(\frac{\partial \varepsilon}{\partial (\sin^2 \Psi)} \right) \quad (3-5)$$

where E is the Young's modulus, ν is Poisson's ratio and ε is the lattice strain of the material. The (4 1 6) plane of the Al_2O_3 matrix was chosen to measure the residual stress due to its high diffraction angle and high diffraction intensity.

3.3 Results

Fig. 3-2 shows the XRD pattern of the $\text{Al}_2\text{O}_3/\text{BaTiO}_3$ -platelet composite after hot-pressing at 1400 °C for 1 hr. Apart from Al_2O_3 and a small amount of BaTiO_3 , two reaction phases, $\text{Ba}_4(\text{Ti}_{0.833}\text{Al}_{0.167})_{12}\text{O}_{27}$ and $\text{BaAl}_{13.2}\text{O}_{20.8}$ are found. A typical platelet within the Al_2O_3 matrix after hot pressing is shown in Fig. 3-3(a). A reaction layer is present between Al_2O_3 matrix and BaTiO_3 platelet. Within the platelet, there are two phases: a white phase and a gray phase (Fig. 3-3(b)). The energy-dispersive X-ray (EDX) analysis was conducted to determine the composition of each phase, which listed in Table 3-1. By combining the XRD and EDX results, the reaction layer (denoted with 1 in Fig. 3-3(b)) between matrix/platelet is a $\text{BaAl}_{13.2}\text{O}_{20.8}$ phase. The gray phase within the platelet is a $\text{Ba}_4(\text{Ti}_{0.833}\text{Al}_{0.167})_{12}\text{O}_{27}$ phase (denoted with 2 in Fig. 3-3(b)), the white one is the residual BaTiO_3 phase (denoted with 3 in Fig. 3-3(b)). The amount of BaTiO_3 phase is the lowest.

Two Vickers indentations were introduced near the platelet. The indentation at the left-hand side of the platelet (Fig. 3-3(b)) induces four cracks at each indent corner. One crack goes straight into the platelet then disappears within the platelet. The indentation at the right-hand side of the platelet is much closer to the platelet. The indentation also produces four major cracks in the matrix. One matrix crack penetrates into the interfacial reaction layer, and then forms many small crack branches within the platelet, Fig. 3-3(b).

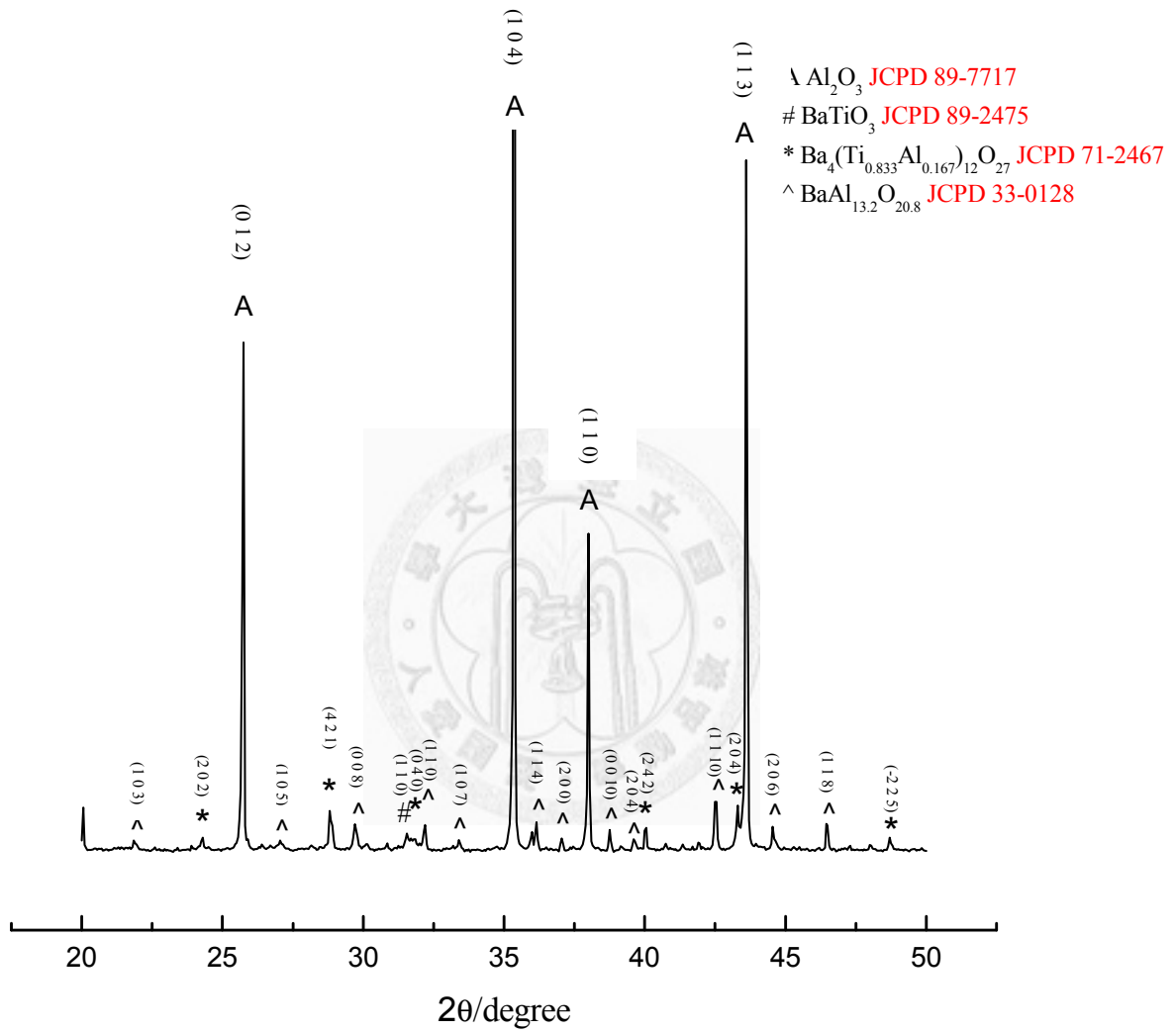
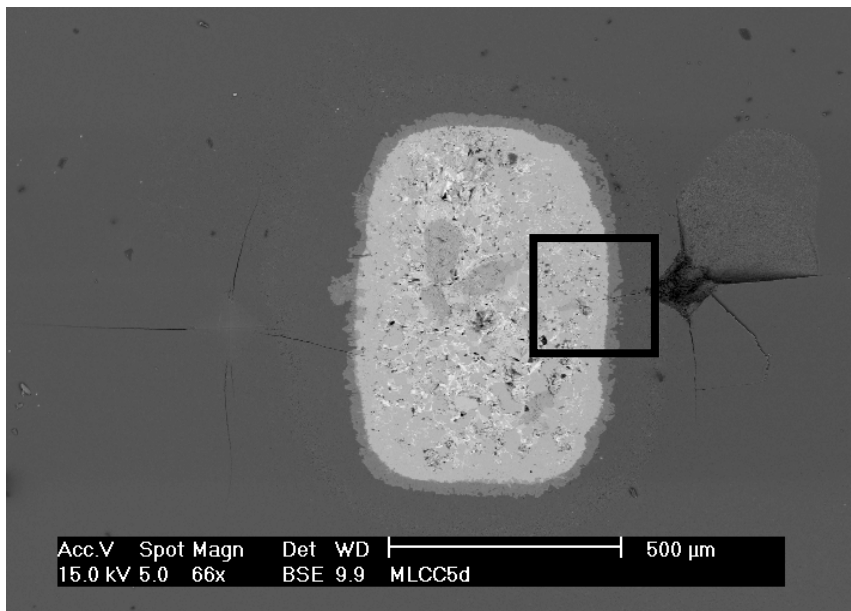
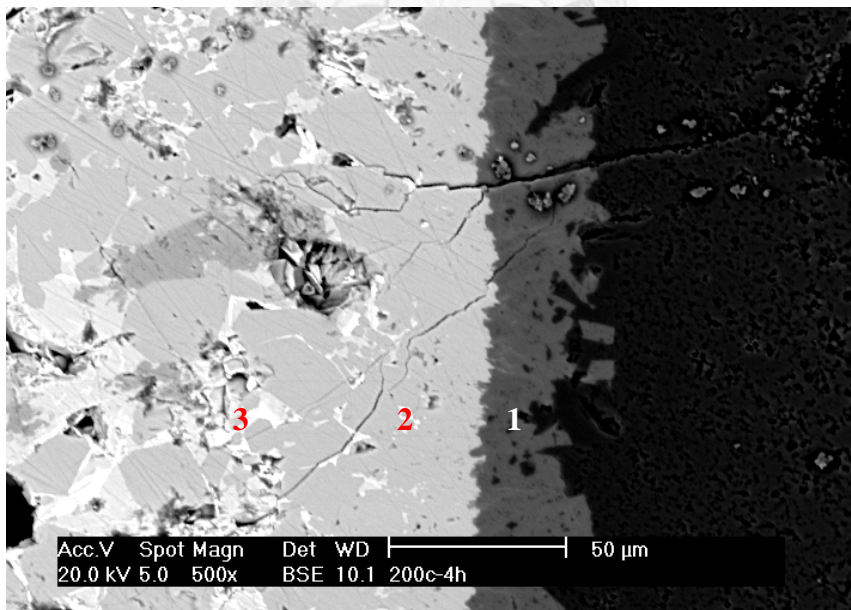


Fig. 3-2. XRD pattern of Al_2O_3 /14 wt% BaTiO_3 -platelet composite hot-pressed at 1400°C .



(a)



(b)

Fig. 3-3. (a) A typical BaTiO₃-platelet in an Al₂O₃/BaTiO₃-platelet composite. (b) Interactions between an indentation-induced crack and platelet.

Table 3-1. The EDX results for positions 1, 2, and 3 in Fig. 3-3 and the corresponding phases.

Element (at%)	Position 1	Position 2	Position 3
O	29.8	38.6	59.3
Al	38.7	44.0	6.7
Ba	2.5	10.9	5.2
Ti	0.3	4.9	27.0
Phase	$\text{BaAl}_{13.2}\text{O}_{20.8}$	$\text{Ba}_4(\text{Ti}_{0.833}\text{Al}_{0.167})_{12}\text{O}_{27}$	BaTiO_3

Table 3-2 shows the characteristics of each phase within the composites. These values are determined by using the nano-indentation technique at a very small load of 50 mN. No crack was observed after the nano-indentation, though micro-cracks may still be formed under the surface [38]. This technique allows us to determine the in-situ physical characteristics of each phase in the composite. The measured elastic modulus of Al_2O_3 and BaTiO_3 and is 411 GPa and 180 GPa, respectively. The measured value for Al_2O_3 is close to the values reported in literature [39]. The measured elastic modulus of BaTiO_3 is 180 GPa, which is higher than the reported values for barium titanate (107~120 GPa [40]). It may partly due to that the BaTiO_3 phase is surrounded by the rigid Al_2O_3 matrix. It may also result from the solution of Al ions into BaTiO_3 grain.

The values in Table 3-2 demonstrate that the hardness of each phase follows the order as $\text{Al}_2\text{O}_3 > \text{BaAl}_{13.2}\text{O}_{20.8} > \text{Ba}_4(\text{Ti}_{0.833}\text{Al}_{0.167})_{12}\text{O}_{27} > \text{BaTiO}_3$. Previous study also indicated that the strength of BaTiO_3 is lower than that of Al_2O_3 [41]. Differ from the previous studies on SiC-platelet toughened Al_2O_3 [32-34], the platelet used in the present study is much weaker than the matrix. Furthermore, a dense reaction phase is formed at the interface. However, the fracture energy (W_{tot}) as calculated from the area under the stress-strain curve during nano-indentation shows a different trend with that of hardness. It suggests that the Ba-containing phases are weak and easily to be

Table 3-2. Elastic modulus, hardness and fracture energy (W_{tot}) for the phases in the $\text{Al}_2\text{O}_3/7 \text{ wt}\% \text{BaTiO}_3$ -platelet composite as determined by using the nano-indentation technique.

	Al_2O_3	$\text{BaAl}_{13.2}\text{O}_{20.8}$	$\text{Ba}_4(\text{Ti}_{0.833}\text{Al}_{0.167})_{12}\text{O}_{27}$	BaTiO_3
Elastic modulus /GPa	411±13	286±11	253±3	180±11
Hardness /GPa	19.2±2.7	16.8±0.4	14.5±0.8	9.7±0.7
W_{tot} /nJ	5.8±0.2	6.9±0.4	7.5±0.2	10.3±0.5

fractured. The fracture energy is high due to the possible formation of many microcracks.

Fig. 3-4 demonstrates the residual strains of Al_2O_3 and $\text{Al}_2\text{O}_3/\text{BaTiO}_3$ platelet composites hot-pressed at 1400°C measured by XRD. Table 3-3 shows the calculated residual stress in the alumina phase of composites. A very small residual stress is present in the monolithic alumina specimen. Such residual stress may be induced by the surface grinding process. As the platelets were added to form the Ba-containing phases, tensile residual stresses were found in the alumina matrix. It is due to that the thermal expansion coefficient of the Ba-containing phases (11 ppm/K for BaTiO_3) [42] is higher than that of alumina (8 ppm/K). Compressive hoop stresses and tensile radial stresses are expected to form at the interface. The crack could deflect around the interface. The nano-indentation analysis demonstrates that the toughening agent used in the present study is softer than that of the matrix. The crack is thus attracted to the platelets because they are elastically softer than the alumina matrix.

3.4 Discussion

The interactions between crack and platelet are demonstrated in Fig. 3-3. As a major crack penetrates into the dense $\text{BaAl}_{13.2}\text{O}_{20.8}$ interphase, many crack branches

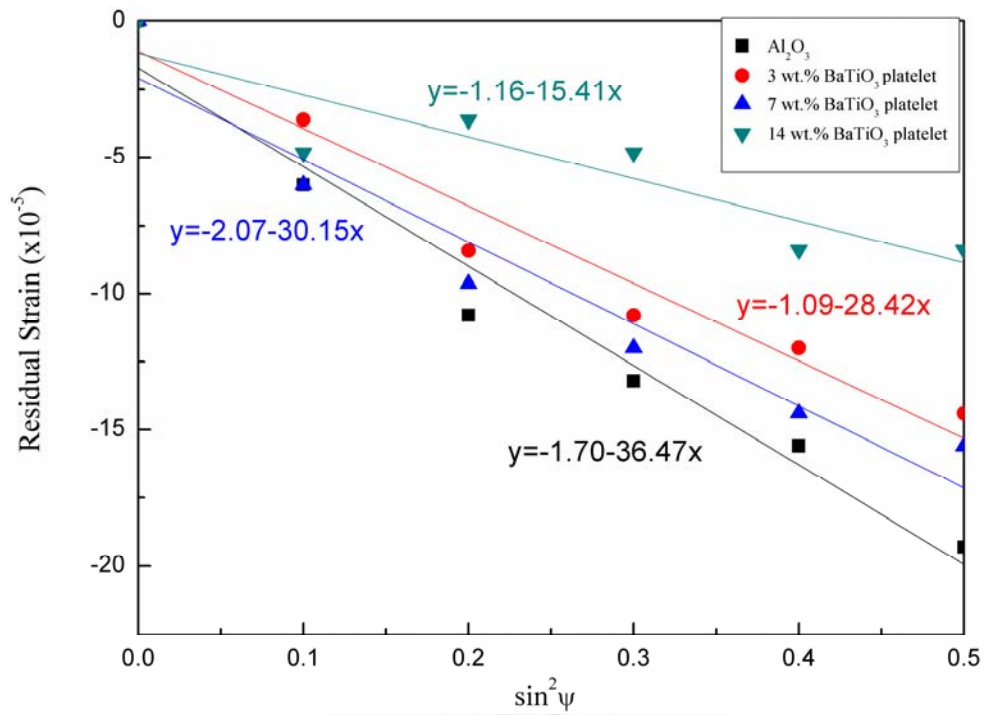


Fig. 3-4. Residual strains of monolithic Al₂O₃ and Al₂O₃/BaTiO₃ platelet composites hot-pressed at 1400°C.

Table 3-3. Residual stress, strength and toughness of Al₂O₃/BaTiO₃-platelet composites. The elastic modulus and Poisson's ratio used to calculate the residual stress are also shown.

	Monolithic Al ₂ O ₃	3 wt.% BaTiO ₃ -platelet	7 wt.% BaTiO ₃ -platelet	14 wt.% BaTiO ₃ -platelet
Elastic modulus ^b /GPa	400	355	257	231
Poisson's ratio ^b	0.24	0.27	0.14	0.15
Residual stress ^a /MPa	-14	25	36	73
Strength ^c /MPa	378±19	185±14	161±19	87±7
Toughness /MPa*m ^{1/2}	4.8±0.3	3.8±0.3	4.0±1.1	2.8±0.6

^a note: determined by X-ray $\sin^2\psi$ technique.

^b note: determined by ultrasonic technique.

^c note: determined by 4-point bending technique.

* note: “-“ denotes compressive stress.

are formed to consume the fracture energy. The crack resistance of the composite is expected to be high. A schematic to demonstrate the toughening behavior is shown in Fig. 3-5. The flexural strength of the composites decreases with the increase of platelet content, Table 3-3. It is mainly due to that the size of the platelet is far too large (length > 500 μm). The presence of such large second phase acts as a stress concentrator, or flaw, to the composites. The strength of the composite is therefore lower than that of monolithic alumina.

The fracture energy for the weak materials in the platelet is higher than that of the matrix, Table 3-2, the toughness of the platelet composite is expected to be higher. However, as the single edge notched beam (SENB) technique was used to determine the global toughness of the composites. The toughness is not meaningful due to that the crack induced from the notch seldom interacts with any platelet. It is mainly due to that the size of multilayer platelet used in the present study is large and the number of platelets is low. It is thus difficult to determine the global toughness of the composites by using the SENB technique. The Vickers indentation technique is thus employed instead to determine the localized toughening behaviour. Each indentation introduces 4 cracks at the tips of the indentation (see Fig. 3-3). By placing the indentation close to the multilayer platelet, the interactions between crack and platelet can then be investigated. By using the crack length induced by Vickers indentation

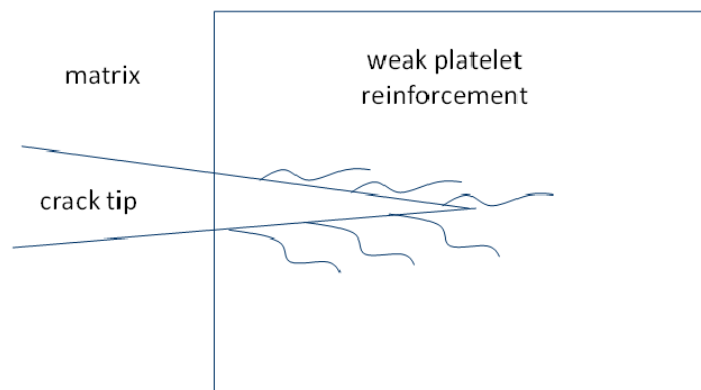
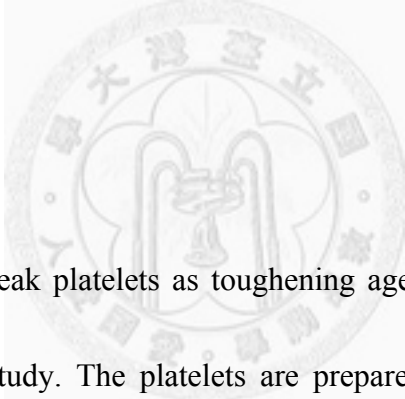


Fig. 3-5. Interactions between a major crack and a weak platelet.

and Eq. 2-4, the toughness anisotropy is observed. Table 3-4 shows the toughness by using the crack length induced by Vickers indentation. The toughness as calculated from the crack toward the BaTiO₃ platelet is much higher than that calculated from the crack moves away from the platelet. It demonstrates that the addition of BaTiO₃ platelets do consume more fracture energy. The platelets with much smaller size should be available from market soon. The use of small dummy platelets as toughening agent is expecting.

3.5 Conclusions



The feasibility of using weak platelets as toughening agent for brittle matrices was evaluated in the present study. The platelets are prepared by using the techniques employed for the manufacture of multilayer components. Many interfaces are presented within the platelets. Though the platelets are soft and may be reactive with the matrix, the major cracks can be attracted by the platelets. The crack is then stopped within the platelet by forming many minor cracks. The shape of MLCCs is similar to that of ceramic platelets. The benefit of such MLCC platelet is its availability.

Table 3-4. Anisotropic toughening effect near a platelet.

	Crack in monolithic Al ₂ O ₃	Crack moves away from platelet	Crack moves toward platelet
Crack length / μm	190 \pm 10	275 \pm 25	127 \pm 20
Fracture toughness ^a / MPam ^{0.5}	4.8 \pm 0.3	3.1 \pm 0.2	7.8 \pm 0.5

^a note: determined by indentation technique.

Chapter 4: Crack Extension Resistance Behaviour in Lamellae Inclusions Toughened Ceramic-Matrix Composite

4.1 Introduction

All tough ceramics exhibit crack extension resistance curves (R-curve). There are three main effects which can lead to a rising R-curve: interaction of the crack borders in the wake of the advancing crack, phase transformation around the crack tip of the advancing crack, and an increase in the size of the process zone due to micro-cracking [43-45]. In addition to the increase in flaw tolerance due to higher fracture toughness, toughened ceramics with R-curves also have the potential to exhibit greater reliability due to smaller strength variability. There is a strong incentive, therefore, to develop and characterize structural ceramics with pronounced R-curve behavior. Recently, Lawn et al. used indentation-fracture-strength method with controlled indentation flaws in different kinds of ceramic materials [46-48] to demonstrate that the R-curve strongly stabilizes crack growth, such that the critical flaw may extend several times its original dimension prior to failure [49].

In the present study, we investigate the indentation-fracture-strength of LTCC matrix with 0, 2, 4 and 10 wt% additions of BaTiO₃-based platelets to determine the

flaw tolerance and toughness-curve characteristics. Microstructural observations for the fracture surface are also presented to demonstrate the toughening mechanism by crack propagation during fracture.

4.2 Experimental Procedures

4.2.1 Raw material

The glass consists of a borosilicate powder (major phase) and alumina fillers (minor phase). A BaTiO₃-based ceramic powder was mixed with several solvents and binders to prepare green tapes. A Ni paste was applied onto the green tape by using screen-printing technique. Several tapes were laminated together and subsequently cut into small platelets. The dimensions of the green platelets were 1.28 x 0.64 x 0.41 mm.

4.2.2 LTCC/BaTiO₃-platelet composite

The glass powder and sintered platelets (with inner electrodes) were dry mixed together in a PE jar for 1 h. The amounts of sintered platelets to glass powder were 2, 4 and 10 wt%. The cylindrical discs were prepared by die-pressing, and pressureless

sintered at 900 °C for 2 h. The dimensions of the sintered specimens were 20.6 ± 0.1 mm in diameter, around 3.7 ± 0.1 mm in height. The apparent density of the specimens after sintering was determined by using the Archimedes water immersion method. The hardness was measured by a Vickers hardness tester (AKASHI AVK-A, Japan). The values of elastic modulus (E) of the specimens were determined by using the ultrasonic reflection method [37]. Prior to the measurement of strength, the disc surface was polished to 1 μm with diamond slurry. After polishing, the specimens were indented at their center of the tensile surface with a Vickers diamond pyramid at contact loads of 0 N, 10 N, 50 N and 100 N. The biaxial strength of the composites was determined by using the one-ball-on-three-ball testing technique (MTS-810, MTS Co., USA). After the strength test, the fracture surface was observed by an optical microscope and a conventional scanning electron microscope (SEM, Philips XL-30, the Netherlands).

4.3 Results

Fig. 4-1 shows the biaxial strength of monolithic LTCC and composites with 2, 4 and 10 wt% addition of platelets. A summary on all the parameters used to calculate

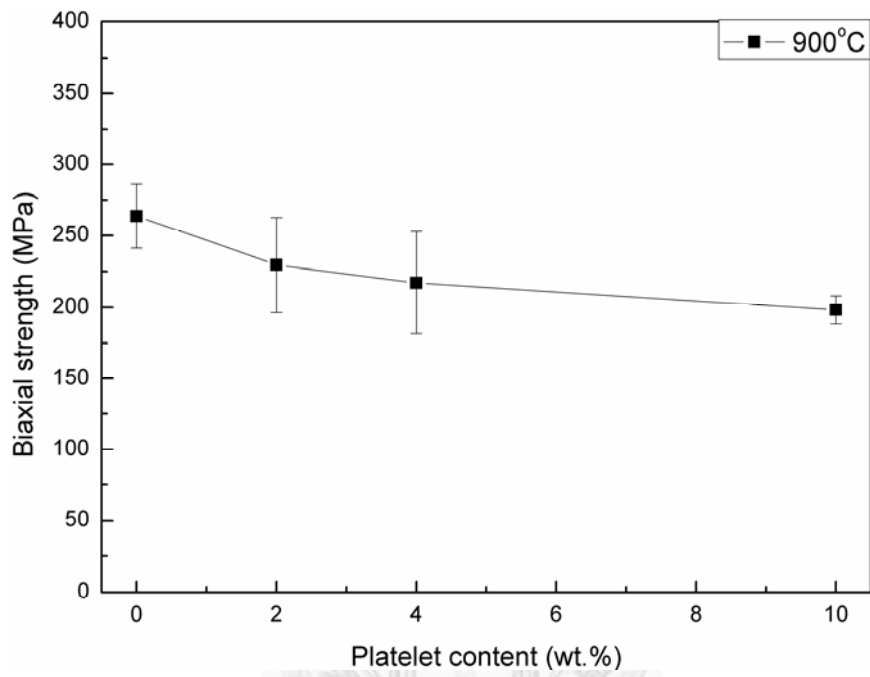


Fig. 4-1. Biaxial strength of LTCC/BaTiO₃-based platelet composites as function of platelet content.

the biaxial strength is given in Table 4-1. The biaxial strength of the composites decreases with the increase of platelet content. Fig. 4-2(a) shows the fracture surface of LTCC/4wt%-platelet composite as observed by optical microscope. The fracture is not taken place at the interface between matrix and reinforcement but at the interface between the inner Ni electrode and the BaTiO₃ tape inside the platelet. More obvious evidence is shown in Fig. 4-2(b) observed by SEM. Since the interface between matrix and reinforcement is relatively stronger than that between the inner Ni electrode and the BaTiO₃ tape inside the platelet, the cleavage within the platelet is thus occurred during fracture (see Fig. 4-2).

Fig. 4-3 plots the measured biaxial strengths as a function of indentation load for the composite with different addition of platelets. Each datum point represents the mean and standard deviation of an average five indentation-flaw failures. The strength decreases with increasing indentation load for monolithic LTCC. The decreasing trend seems to be alleviated by adding the platelets within lamellae structure. After the addition of platelet up to 4 wt%, the strength appears to be a constant with the indentation load up to 100 N.

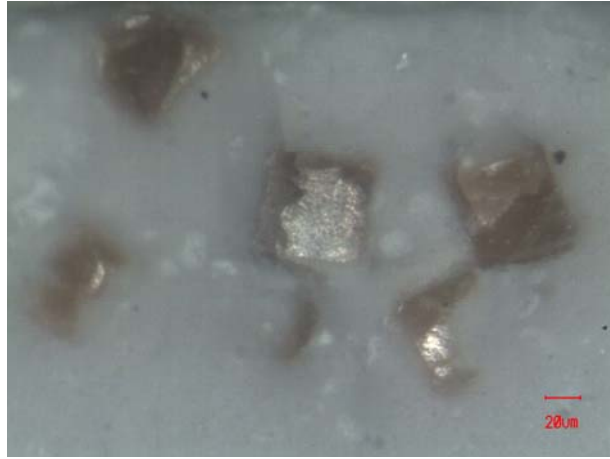
4.4 Discussion

Table 4-1. Apparent density, elastic modulus and Poisson's ratio of LTCC and LTCC/BaTiO₃-based platelet composites.

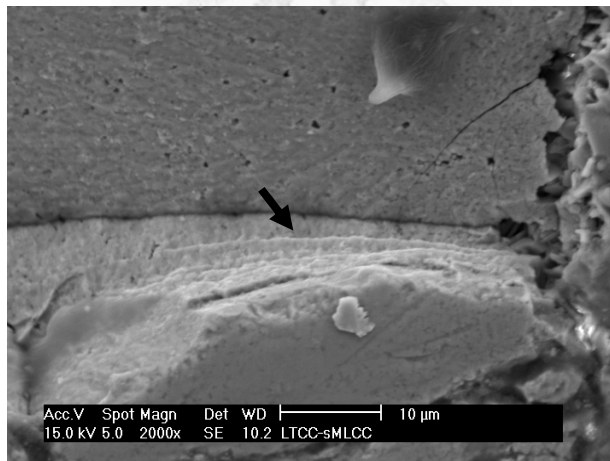
	LTCC	LTCC/2 wt% platelet	LTCC/4 wt% platelet	LTCC/10 wt% platelet
Density* (g/cm ³)	2.69 ± 0.02	2.71 ± 0.01	2.77 ± 0.02	2.84 ± 0.01
Elastic modulus** (GPa)	71	73	74	80
Poisson's ratio**	0.09	0.1	0.11	0.14

*note: determined by Archimedes water immersion method.

**note: determined by ultrasonic reflection technique at 5 MHz.



(a)



(b)

Fig. 4-2. Fracture surfaces of LTCC/BaTiO₃-based platelet composites: (a) optical microscopy for over-view, (b) SEM for close-view inside one platelet. The black arrow indicates the position of Ni electrode.

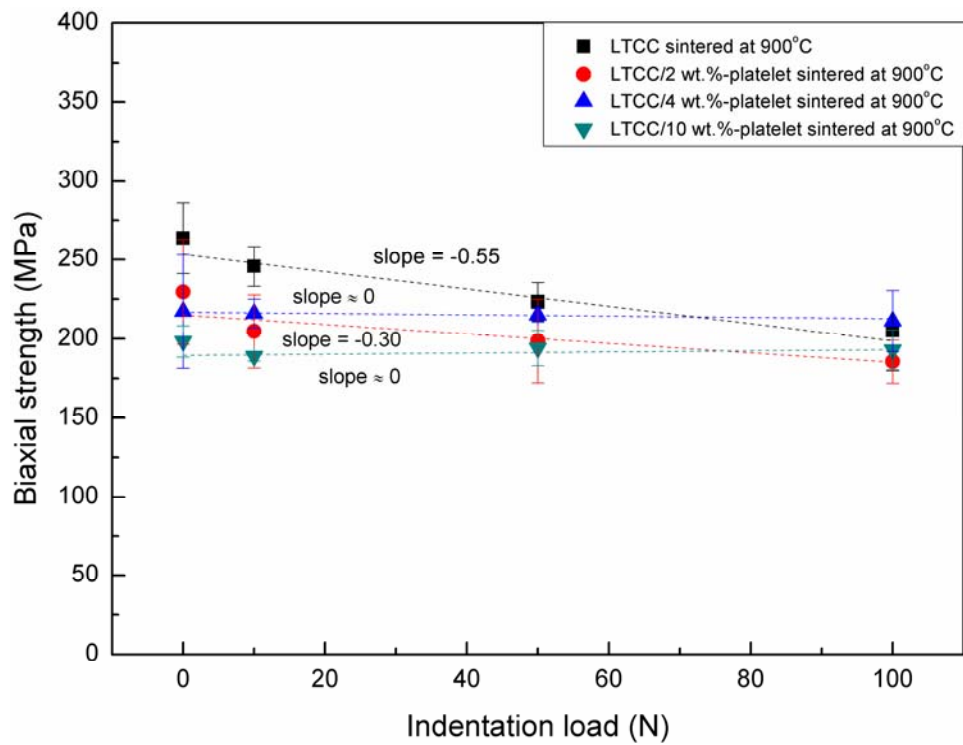


Fig. 4-3. Plot of indentation-fracture-strength versus indentation load for LTCC/BaTiO₃-based platelet composites.

In Fig. 4-2, the ultra-large size of the platelet (length > 500 μm) plays the major role in the presence of a stress concentrator, or flaw, to the composites. The strength of the composite is therefore lower than that of monolithic LTCC. One thing should also be noticed that the thermal expansion coefficient of LTCC (~ 5.5 ppm/k [50]) is lower than BaTiO₃-based platelet (11 ppm/k [42]), therefore, the compressive hoop stresses and tensile radial stresses are expected to form on the matrix/reinforcement interfaces. The fracture route should be deflected on the interface. Instead, the observed fracture surface in Fig. 4-2 reveals that the fracture route penetrate through the matrix/reinforcement interface and be deflected within the lamellae structure of the platelet.

Chantikul et al. indicated that the tendency of indentation-fracture-strength is a manifestation of the R-curves for materials [47]. Since the R-curve behaviour for glass ceramics is still lack of literature, the present results are compared with the former results from Chantikul [47] and are shown in Fig. 4-4. The R-curve behavior of LTCC/BaTiO₃-platelet system is close to the grain size range between 47.6 μm and 79.8 μm of monolithic alumina, which indicates the crack extension resistance of LTCC material is significantly improved by the addition of platelets within weak interfaces.

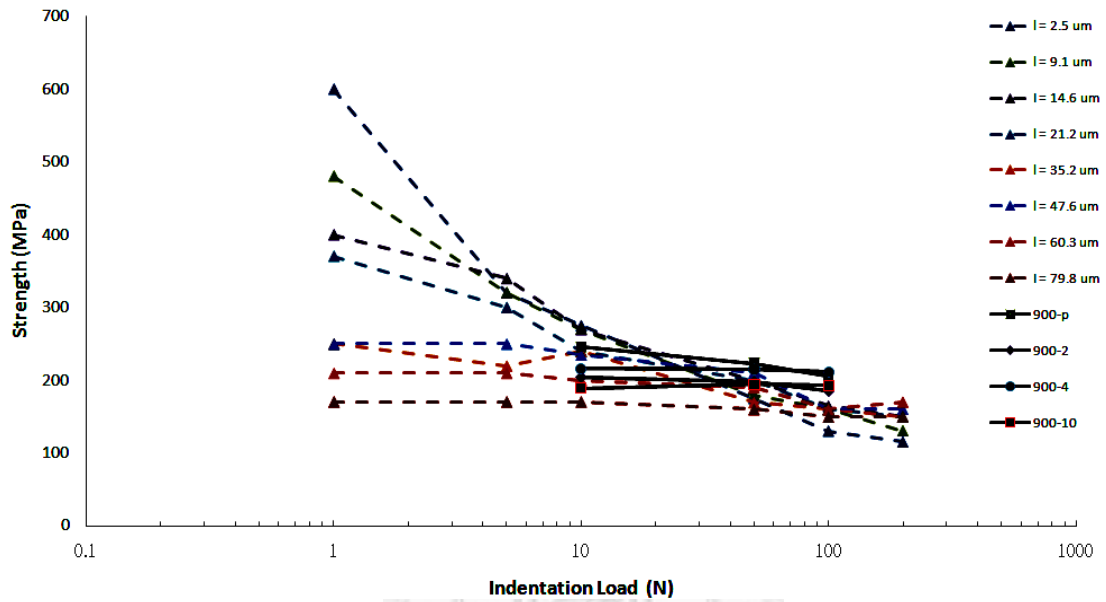


Fig. 4-4. Plot of indentation-fracture-strength versus indentation load for LTCC/BaTiO₃-based platelet composites compared with the former results from Chantikul et al [47]. The black solid lines are from the present work and the dotted lines are from ref. 47.

In order to have a further insight for the toughening effect in LTCC/BaTiO₃-based platelet composites, the strength equation corresponding to flaws induced by indenters of given geometry takes the form from [46]:

$$\sigma = [K_c^4 \left(\frac{H}{E}\right)^{1/2}]^{1/3} / P^{1/3} \quad (4-1)$$

Where σ is the measured strength, K_c is the toughness, H is the hardness, E is the elastic modulus and P is the indentation load. The toughness curve can thus be obtained by indentation-fracture-strength with different indentation loads. In the present study, the monolithic LTCC and the composition of LTCC with 4 wt% BaTiO₃ platelets are taken as representatives for this calculation. The measured hardness of monolithic LTCC is 5.8 ± 0.1 GPa and that of composite is 6.5 ± 0.3 GPa.

The toughness curves are thus shown in Fig. 4-5, which indicates that the toughening effect increases with increasing indentation load up to 90 N (the length of indent diagonal = 225 μ m) for monolithic LTCC and this increasing trend is postponed by the platelet addition with the load to over 110 N (the length of indent diagonal > 250 μ m). To trace back the fitting curves to the flaw-free point (without indent), the crack-tip toughness of LTCC is about 3.8~4 MPa \sqrt m and will be increased up to 7.5 MPa \sqrt m by adding 4 wt% platelets. The value of the indent load to the corresponding

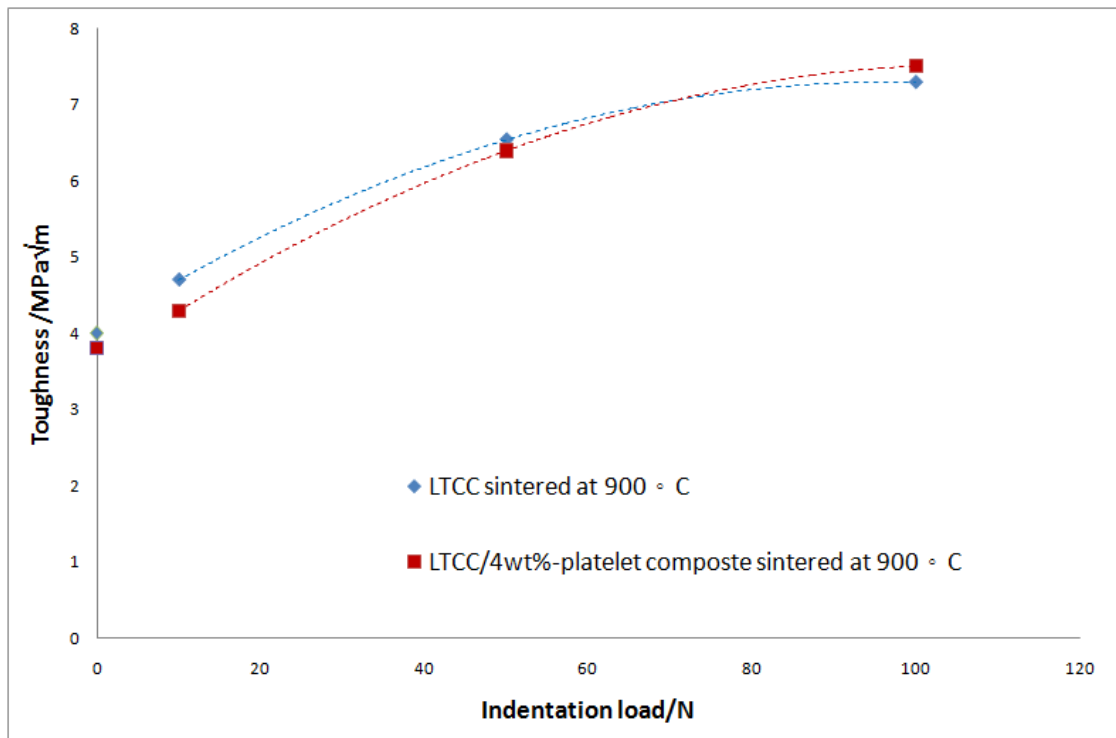


Fig. 4-5. Toughness curves for monolithic LTCC and LTCC/4 wt% BaTiO₃-based platelet composite as a function of indentation load.

Table 4-2. The value of the indent load to the corresponding crack size for the composites sintered at 900°C.

Material Load (N)	LTCC	LTCC/2wt% platelet	LTCC/4wt% platelet	LTCC/10wt% platelet
0	-	-	-	-
10	$40 \pm 4 \mu\text{m}$	$41 \pm 1 \mu\text{m}$	$37 \pm 7 \mu\text{m}$	$36 \pm 3 \mu\text{m}$
50	$150 \pm 12 \mu\text{m}$	$131 \pm 11 \mu\text{m}$	$150 \pm 3 \mu\text{m}$	$132 \pm 7 \mu\text{m}$
100	$241 \pm 11 \mu\text{m}$	$199 \pm 6 \mu\text{m}$	$235 \pm 3 \mu\text{m}$	$245 \pm 26 \mu\text{m}$

crack size for the composites sintered at 900°C is listed in Table 4-2. The lower load (10 N) shows a decreasing trend of crack size from 40 μm to 36 μm with increasing the addition of BaTiO₃-platelets up to 10 wt%. The reason is due to the presence of the second phase will stop the crack propagation. On the other hand, when increasing the indent load, there's no obvious trend for the different addition of platelets. The reason is supposed to be the influence of the ultra-large size of the platelet. Moreover, after the yield point, the slope of the decreasing part of composite for the toughness curve is smaller than that of monolithic LTCC. Another evidence is also given from the microstructure of fracture surface in Fig. 4-2. The trans-reinforcement fracture was occurred within the lamellae structure of platelets. The fracture energy can be dissipated by crack deflection inside the reinforcement. Therefore, the flaw tolerance of the material can thus be improved.

4.5 Conclusions

The crack extension resistance of lamellae inclusions toughened ceramic is characterized by indentation-fracture-strength method. The LTCC/BaTiO₃-based platelet with inner Ni electrode system is used as the model system. Many inner weak interfaces are present between the BaTiO₃ and inner Ni electrodes within the platelets.

The cleavages of such inner weak interfaces can dissipate more fracture energy than that of the brittle matrix. Furthermore, the fracture route is deflected within the platelets. The toughness of LTCC is therefore enhanced. The glass/BaTiO₃-based platelet composites are prepared to demonstrate the feasibility of using such reinforcement to improve the toughness of brittle ceramics. The damage resistance of glass is considerably improved after the addition of platelets.



Chapter 5: Toughening Alumina with Layered Ti_3SiC_2

Inclusions

5.1 Introduction

The application of ceramics is often limited by their poor toughness. To improve the toughness of ceramics is therefore a long-standing pursuit for many ceramists. The addition of hard and strong ceramic whiskers or platelets can usually enhance the toughness of ceramics. For example, the toughness of Al_2O_3 is tripled as 25 wt.% SiC whiskers were added [31], or enhanced by 10-50% after the addition of 5-30 vol.% SiC platelets [33]. The strength and hardness of these reinforcements are high. However, the paradox of using these reinforcements is that the hardness and strength of reinforcement affect little on the toughening behavior. Instead, a weak interface between matrix and reinforcement plays the most important role on the toughness enhancement.

For the ceramic matrix composite containing hard and strong reinforcement, the reinforcement can carry partly the load from the matrix before fracture. Once a major crack is introduced, the hardness and strength of the reinforcement are no longer required. The interface between matrix and reinforcement should be de-bonded before

the reach of a major crack [51]. Major crack can then either deflect from or propagate along the weak interface. The toughness is then enhanced. Due to the weak interface is essential to the toughness enhancement, any reaction or sintering between the matrix and reinforcement should be avoided. Such requirement limits the choice of reinforcement. However, if the weak interface is located within the reinforcement, such reinforcement can then be added into any brittle matrices. Even when the reinforcement is reacted with the matrix to form a strong bonding, crack can still be deflected by the weak interface within the reinforcement.

Titanium silicon carbide (Ti_3SiC_2) is a ternary compound consisting of three planes of Ti-C separated by layers of Si [52]. Unlike other transition metal carbides, Ti_3SiC_2 is relatively ductile due to the presence of weak internal layers. Many kink bands and delamination cracks are formed within the Ti_3SiC_2 crystal under an external load [52]. In the present study, the Ti_3SiC_2 particles are used as the reinforcement for alumina. Since the thermal expansion coefficient (α) of Ti_3SiC_2 ($\alpha = 8.9 \times 10^{-6} \text{ K}^{-1}$ [53]) is very close to that of Al_2O_3 ($\alpha = 8.9 \times 10^{-6} \text{ K}^{-1}$ [53-54]), the residual stress is expected to be small. The Al_2O_3 - Ti_3SiC_2 composite can thus be treated as a model system. Several research groups had determined the mechanical properties of the Ti_3SiC_2 -toughened Al_2O_3 [55-57]. A summary on the previous reported toughness values is given in Table 5-1. The Table demonstrates that the addition of Ti_3SiC_2

particles can indeed enhance the toughness of Al_2O_3 . Luo et al had suggested that the toughening is contributed by the pull-out and plastic deformation of Ti_3SiC_2 particles [55-57]. However, no direct evidence on the plastic deformation was given. The toughness increase as resulted from crack deflection also depends strongly on the shape of the second phase particles. However, the shape factor is not considered in the previous studies. Furthermore, it is common that more than one toughening mechanism may be active during the fracturing of one composite. In a recent study, Sarkar et al. also analyzed the fracture mechanism and characteristic R-curve of monolithic Ti_3SiC_2 [58]. It indicates that delamination along the weaker basal planes leads to the creation of microlamellae within a single grain and consequently, the deformation and distortion of such lamellae provides a potent contribution to toughening. When a crack propagates through bulk Ti_3SiC_2 , crack deflection occurred along the weak interface between lamellae ligaments continually, leading to a fluctuating crack path, and correspondingly an extended effective crack length is formed which absorbed more fracture energy. In the present study, the toughening mechanism for the $\text{Al}_2\text{O}_3/\text{Ti}_3\text{SiC}_2$ composites is investigated carefully. The role of plastic deformation of Ti_3SiC_2 on toughening is also estimated by using different theories.

Table 5-1. Reported toughness increase values for the Al₂O₃/20 vol%Ti₃SiC₂ composite [55-57].

Process	Sintering temp. / °C	Measurement method for toughness	ΔK_{Ic} / MPa \sqrt{m}	Toughening mechanism	References
SPS*	1300	Indentation	2.5	Pull-out, micro-plastic deformation	55
HP**	1600	SENB***	3	Same as above	56
HP**	1600	SENB***	3	Same as above	57

* note: SPS denotes spark plasma sintering, the technique is also termed as pulse electrical current sintering.

** note: HP denotes hot pressing.

*** note: SENB denotes single-edge-notched beam.

5.2 Experimental Procedures

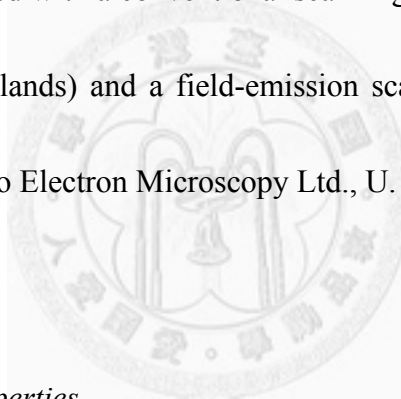
5.2.1 Samples preparation

The raw materials used were Al₂O₃ (TM-DAR, $d_{50} = 0.2 \mu\text{m}$, Taimei Chem. Co. Ltd., Tokyo, Japan) and Ti₃SiC₂ powders ($d_{50} = 4.0 \mu\text{m}$). The preparation procedures for the Ti₃SiC₂ powder can be found in a previous study [59]. Fig. 5-1 shows the morphology of the Ti₃SiC₂ particles. The Al₂O₃ and Ti₃SiC₂ powders were dry-mixed for 1 hr and then sieved. The amount of Ti₃SiC₂ powder added was 10 vol.% or 20 vol.%. After sieving, the powder mixture was hot-pressed at 1400°C and 1450°C in a graphite mould under a load of 25 MPa for 1 hr (High-multi-5000, Fujidempa Kogyo Co., LTD., Japan) in Ar. The temperatures were chosen to avoid the decomposition of Ti₃SiC₂ at higher temperature [59-61]. The dimensions of the hot-pressed specimens were 50 mm in diameter and roughly 4.5 mm in thickness. The hot-pressed specimens were cut into rectangular bars with a diamond saw. The rectangular specimens were then ground longitudinally with a 44 μm grit resin-bonded diamond wheel at cutting depths of 5 μm /pass. The final dimensions of the specimens were 4 x 3 x 45 mm.

5.2.2 Phase and structure analysis

The X-ray diffractometry (XRD, PW1830, Philips Co., Netherlands) was used for phase analysis. The XRD was operated at 35 kV and 20mA with a scanning rate of $3^\circ 2\theta/\text{min}$. The densities of the specimens after sintering were determined by using the Archimedes water replacement method. The relative density of composite was calculated by using 3.98 g/cm^3 for Al_2O_3 [62] and 4.53 g/cm^3 for Ti_3SiC_2 [59].

In order to carry out the microstructure observation, the specimens were ground with SiC abrasive papers and polished with $0.1\mu\text{m}$ diamond particles. The microstructure was observed with a conventional scanning electron microscope (SEM, Philips XL-30, the Netherlands) and a field-emission scanning electron microscope (FE-SEM, model 1530, Leo Electron Microscopy Ltd., U. K.).



5.2.3 Bulk mechanical properties

The flexural strength of the specimens was determined by four-point bending technique with the upper and lower spans of 10 and 30 mm, respectively (MTS-810, MTS Systems Co., USA). The rate of loading was 0.48 mm/min. The hardness was measured by a Vickers hardness tester (AKASHI AVK-A, Japan). The indentation technique [29] was used to determine the toughness of $\text{Al}_2\text{O}_3/\text{Ti}_3\text{SiC}_2$ composites. The values of elastic modulus and Poisson's ratio of the bulk composites were measured by the ultrasonic reflection method [37].

The residual stress of the composite was measured by X-ray diffractometer (Siemens D-5000, Germany) using the $\sin^2\psi$ method [30]. The ψ was the angle between the diffraction plane normal and specimen surface normal. In the present study, the chosen ψ values were 0° , 18.43° , 26.56° , 33.21° , 39.23° and 45° . The Al_2O_3 (416) plane was used for its high diffraction angle and relatively high diffraction intensity [39]. The shift of the Al_2O_3 (416) plane was used to estimate the residual strain, ϵ . The residual stress can then be calculated by Eq. 3-5.

5.2.4 Nanoindentation tests

The Ti_3SiC_2 particles were dispersed within the Al_2O_3 matrix. Since the plastic deformation behaviour of a ductile phase under constraint was different from that of its constrain-free state [63], the load-deformation behaviours of Ti_3SiC_2 particles within Al_2O_3 matrix were determined by using a nano-indenter (UNAT[®], ASMEC, Germany). The tip of the nano-indenter was Berkovich type (radius = 200 nm). The elastic modulus of the constrained Ti_3SiC_2 particles was derived from the contact stiffness during the unloading process, following the standard Oliver and Pharr method [64] as following:

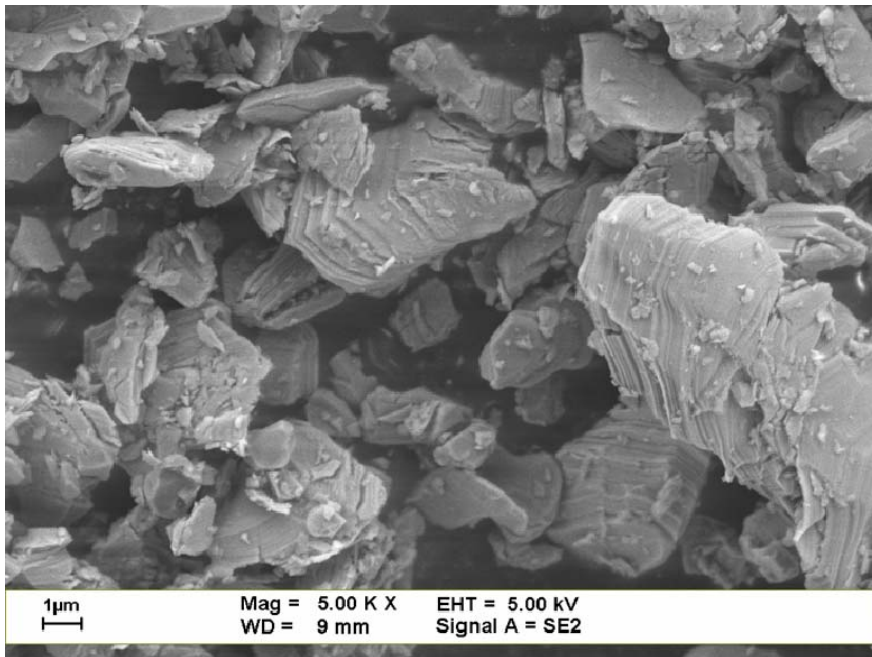


Fig. 5-1. Morphology of the Ti₃SiC₂ particles.

$$S = \beta \frac{2}{\pi} E_{eff} \sqrt{A} \quad (5-1)$$

and

$$\frac{1}{E_{eff}} = \frac{1-\nu^2}{E} + \frac{1-\nu_i^2}{E_i} \quad (5-2)$$

where S was the measured unloading stiffness; A was the projected contact area at onset of unloading; β was the indenter geometry dependent dimensionless parameter; E and ν were the elastic modulus and Poisson's ratio of the test material (Ti_3SiC_2); E_i and ν_i were the elastic modulus and Poisson's ratio of the indenter material (diamond). For diamond, the E_i and ν_i were 1140 GPa and 0.07, respectively.

5.2.5 Crack-extension-resistance behaviour (*R-curve*) tests

In the present work, we determined the *R-curve* of $\text{Al}_2\text{O}_3/\text{Ti}_3\text{SiC}_2$ composite with Single Edge V-Notch Beam (SEVNB) method in 4-point bending with stable crack growth. The V-notches were cut into the rectangular samples with a diamond saw and sharpened with a razor blade as specified by the SEVNB technique [65] (also see section 2.3.2). The tip radius of pure alumina was about 12.5 μm , and that of the composite was about 20 μm . The prepared initial crack lengths were about 1.9 mm. The polished surfaces of all specimens were sputtered with 100 nm thick gold

coatings, which significantly improve the optical observation of the crack. The toughness $K_{R}(\alpha)$ was calculated according to [66] and the details can be found in section 2.3.2 and Eq. 2-3. The mechanical experiments were performed in a very stiff displacement controlled 4-point bending device, where the support rollers have distances of 10 mm and 20 mm [67]. Stable crack growth was conducted semi-automatically via a computer aided control system [68]. This technique, based on a force-displacement evaluation, enabled stable crack growth even without visible crack advance on the sample surface [69].



5.3 Results

5.3.1 Phase analysis and physical properties

Fig. 5-2 shows the XRD patterns of starting Ti_3SiC_2 powder and of the $\text{Al}_2\text{O}_3/20\%\text{Ti}_3\text{SiC}_2$ composites after hot-pressing at 1400°C and 1450°C for 1hr. The XRD results reveal that the major phase of the starting powder is a hexagonal- Ti_3SiC_2 , the minor phases are TiO_2 , TiC and Ti_5Si_3 . Two minor phases, TiO_2 and TiC , remain in the $\text{Al}_2\text{O}_3/\text{Ti}_3\text{SiC}_2$ composites after hot pressing. The Ti_5Si_3 phase is no longer existed after hot-pressing.

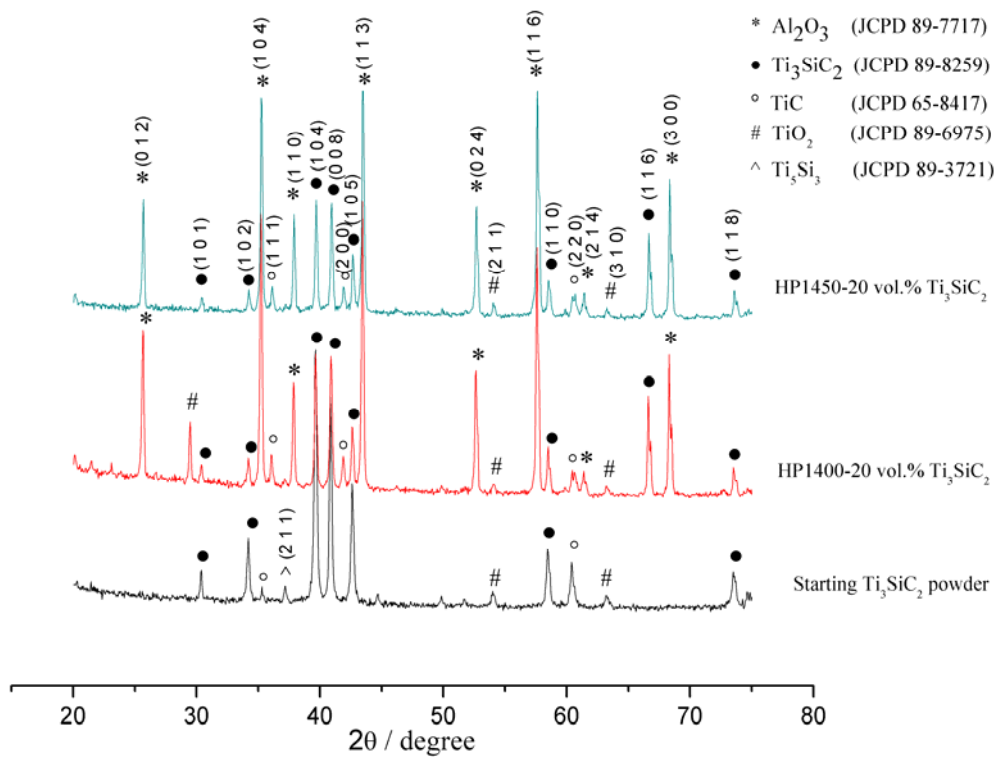


Fig. 5-2. XRD patterns for the starting Ti_3SiC_2 powder and $\text{Al}_2\text{O}_3/20\%\text{Ti}_3\text{SiC}_2$ composites after hot-pressing at 1400 C and 1450°C.

The relative density of all the composites is higher than 96% (Table 5-2). The addition of Ti_3SiC_2 particles reduces slightly the final density. A typical SEM micrographs of the sintered composite prepared by hot-pressing at 1450°C is shown in Fig. 5-3. The brighter phase is Ti_3SiC_2 and the grey matrix is Al_2O_3 . The Ti_3SiC_2 inclusions distributed uniformly within the Al_2O_3 matrix and their size is about 4~5 μm . Pores are hardly observed on the cross-section.

5.3.2 Mechanical properties

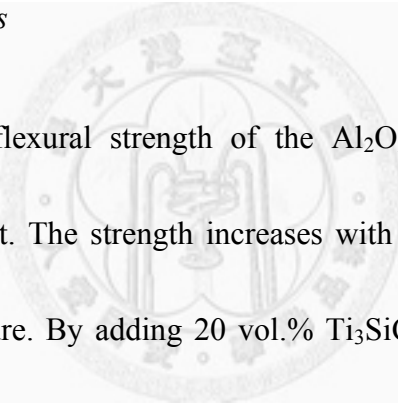


Fig. 5-4 shows the flexural strength of the $\text{Al}_2\text{O}_3/\text{Ti}_3\text{SiC}_2$ composites as a function of Ti_3SiC_2 content. The strength increases with increasing Ti_3SiC_2 content and hot-pressing temperature. By adding 20 vol.% Ti_3SiC_2 particles into Al_2O_3 , the strength is increased by around 15%. Fig. 5-5 and Fig. 5-6 show the Vickers hardness and fracture toughness of the $\text{Al}_2\text{O}_3/\text{Ti}_3\text{SiC}_2$ composites as a function of Ti_3SiC_2 content, respectively. As far as the hardness is concerned, the addition of Ti_3SiC_2 reduces slightly the hardness of alumina. Nevertheless, the toughness of Al_2O_3 is enhanced after the addition of Ti_3SiC_2 inclusions. For the specimen prepared by hot-pressing at 1450°C , a 40% toughness enhancement is observed for the composite containing 20 vol.% Ti_3SiC_2 .

Table 5-2. Relative density, elastic constants and residual stress of monolithic Al₂O₃ and Al₂O₃/Ti₃SiC₂ composites.

Hot-pressing temperature / °C	1400°C			1450°C		
	Al ₂ O ₃	Al ₂ O ₃ /10 vol.% Ti ₃ SiC ₂	Al ₂ O ₃ /20 vol.% Ti ₃ SiC ₂	Al ₂ O ₃	Al ₂ O ₃ /10 vol.% Ti ₃ SiC ₂	Al ₂ O ₃ /20 vol.% Ti ₃ SiC ₂
Relative density / %	99	98	96	99	98	97
Elastic modulus* / GPa	400	386	371	390	375	366
Poisson's ratio*	0.24	0.18	0.24	0.24	0.19	0.19
Residual stress** / MPa	-14	2	8	-11	-13	-21

* note: determined by ultrasonic method

** note: “-“ denote compressive stress, determined by the X-ray $\sin^2\psi$ method

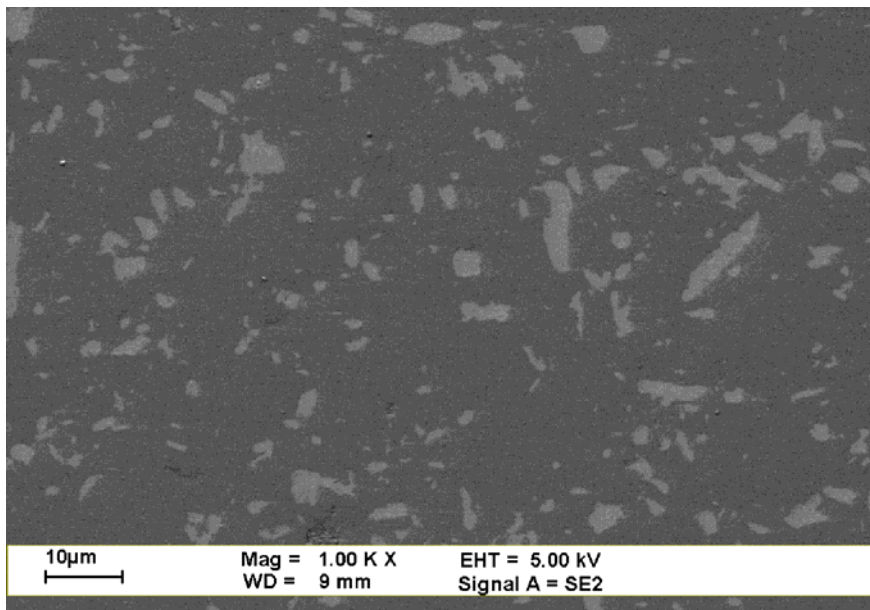


Fig. 5-3. Typical SEM micrograph for the Al₂O₃/10%Ti₃SiC₂ composite.

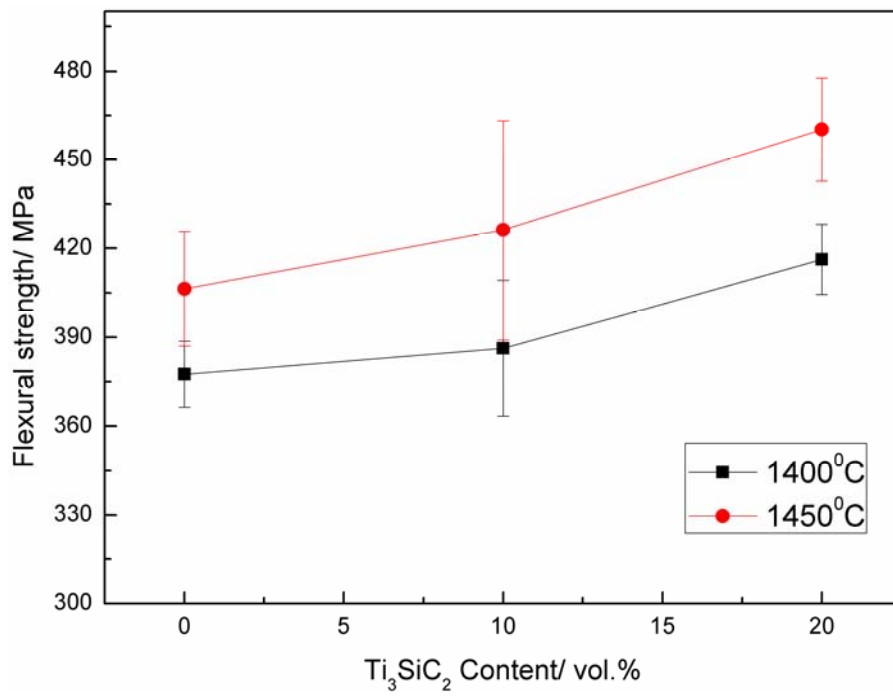


Fig. 5-4. Flexural strength of Al₂O₃/Ti₃SiC₂ composites as function of Ti₃SiC₂ content.

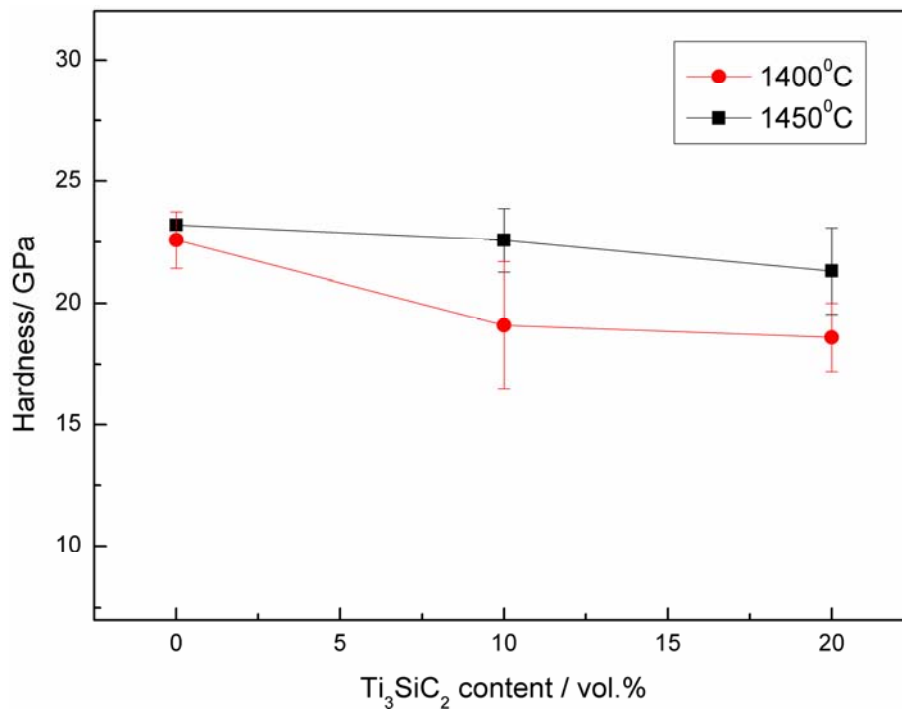


Fig. 5-5. Hardness of $\text{Al}_2\text{O}_3/\text{Ti}_3\text{SiC}_2$ composites as function of Ti_3SiC_2 content.

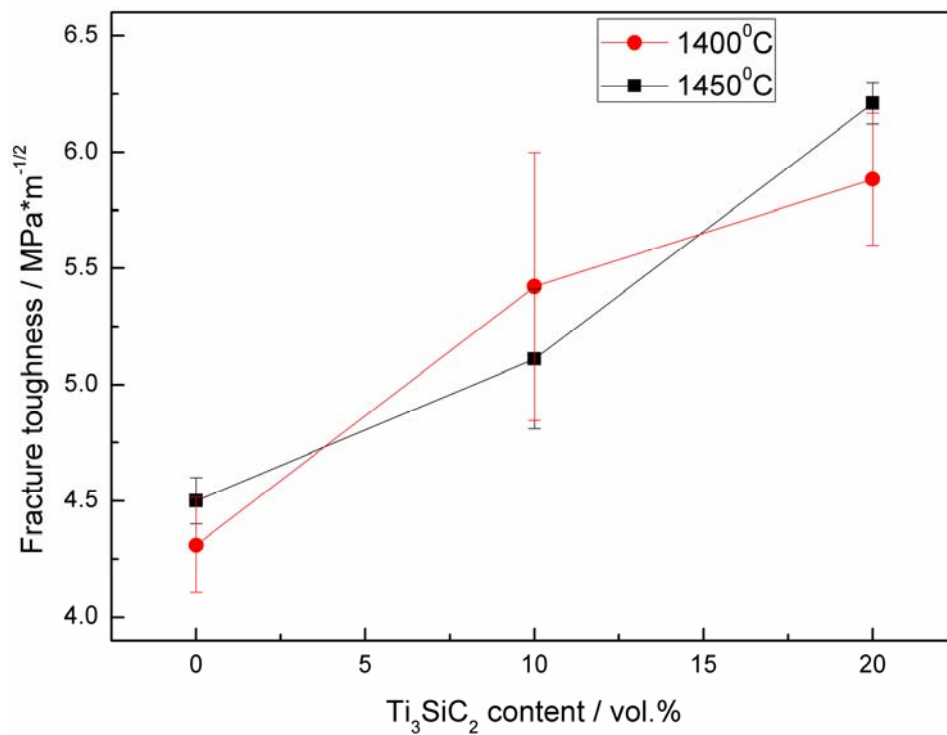
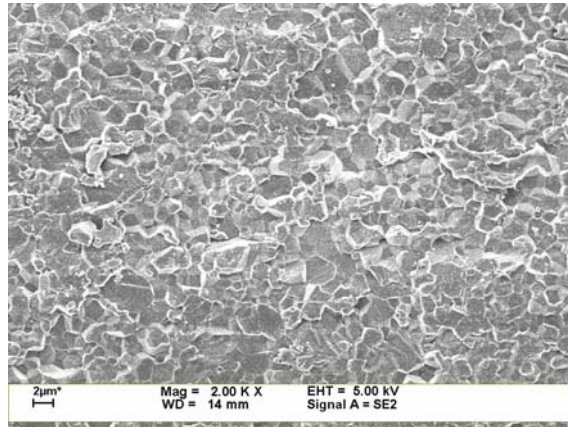


Fig. 5-6. Fracture toughness of $\text{Al}_2\text{O}_3/\text{Ti}_3\text{SiC}_2$ composites as function of Ti_3SiC_2 content.

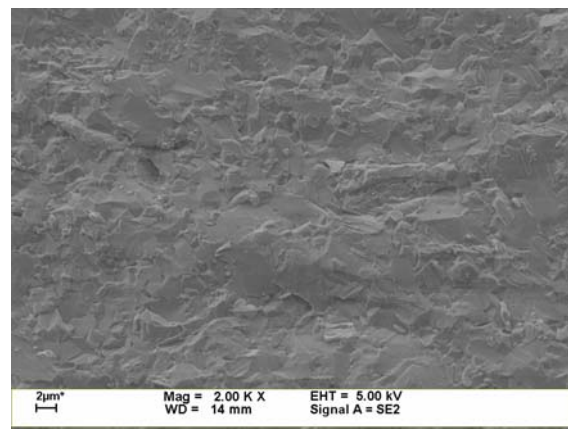
Fig. 5-7 shows the fracture surfaces of monolithic Al_2O_3 and $\text{Al}_2\text{O}_3/10\%\text{Ti}_3\text{SiC}_2$ composite prepared by hot-pressing at 1450°C for 1hr. The fracture mode of monolithic Al_2O_3 is an intergranular type, which is shown in Fig. 5-7(a). The fracture mode is changed to transgranular mode as Ti_3SiC_2 inclusions are added, which is shown in Fig. 5-7(b). Many cleavages within Ti_3SiC_2 inclusions are observed in Fig. 5-7(c). Since many fracture facets within Ti_3SiC_2 inclusions are observed, indicating that the cleavage is taken place at the weak layers within the Ti_3SiC_2 crystal. The interactions between a major crack induced by Vickers indentation and Ti_3SiC_2 inclusions are demonstrated in Fig. 5-8. Crack is mainly passing through the Ti_3SiC_2 inclusions, and occasionally propagating along the $\text{Al}_2\text{O}_3/\text{Ti}_3\text{SiC}_2$ interface.

5.3.3 Residual stress analysis

Fig. 5-9 shows the residual strain as measured from the shift of Al_2O_3 (4 1 6) peak as a function of $\sin^2\psi$. The slope of the fitted lines, reflects the magnitude of residual stress (see Eq. 3-5), is very close to each other. It suggests that the residual stress in monolithic Al_2O_3 is very close to that in $\text{Al}_2\text{O}_3/\text{Ti}_3\text{SiC}_2$ composite. Table 5-2 shows the elastic modulus and Poisson ratio as determined by the ultrasonic methods. These values are then used to calculate the residual stress with Eq. 3-5. The calculated residual stress is also shown in the Table. Compressive stress is found in both monolithic Al_2O_3 and $\text{Al}_2\text{O}_3/\text{Ti}_3\text{SiC}_2$ composites. These compressive stresses are



(a)

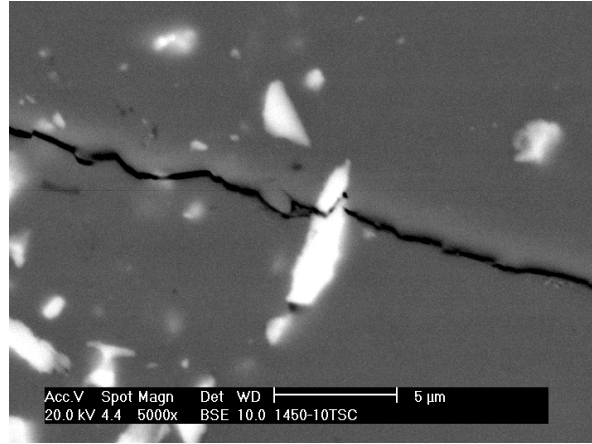


(b)

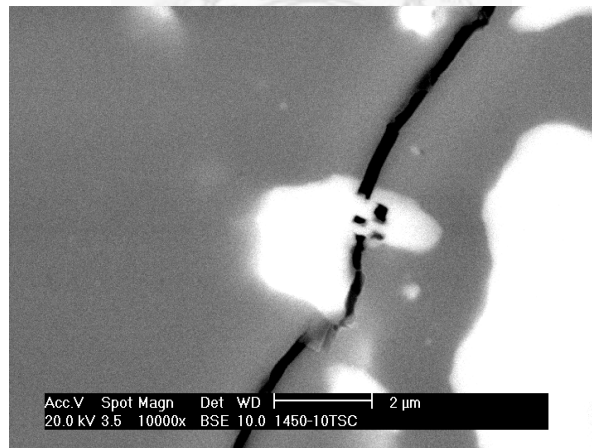


(c)

Fig. 5-7. Fracture surface of (a) monolithic Al_2O_3 and (b) (c) $\text{Al}_2\text{O}_3/10 \text{ vol.}\% \text{Ti}_3\text{SiC}_2$ composites.

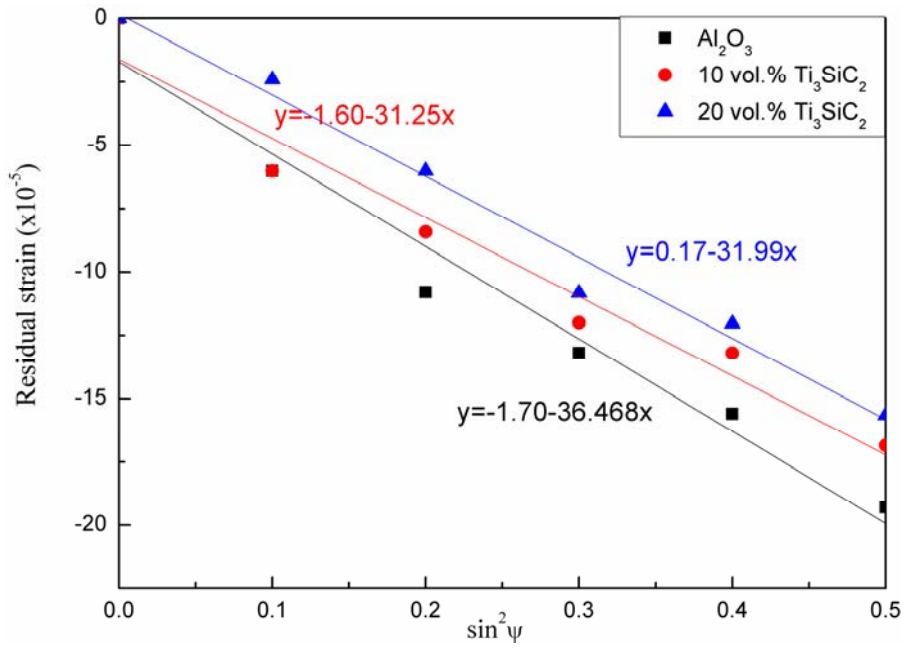


(a)

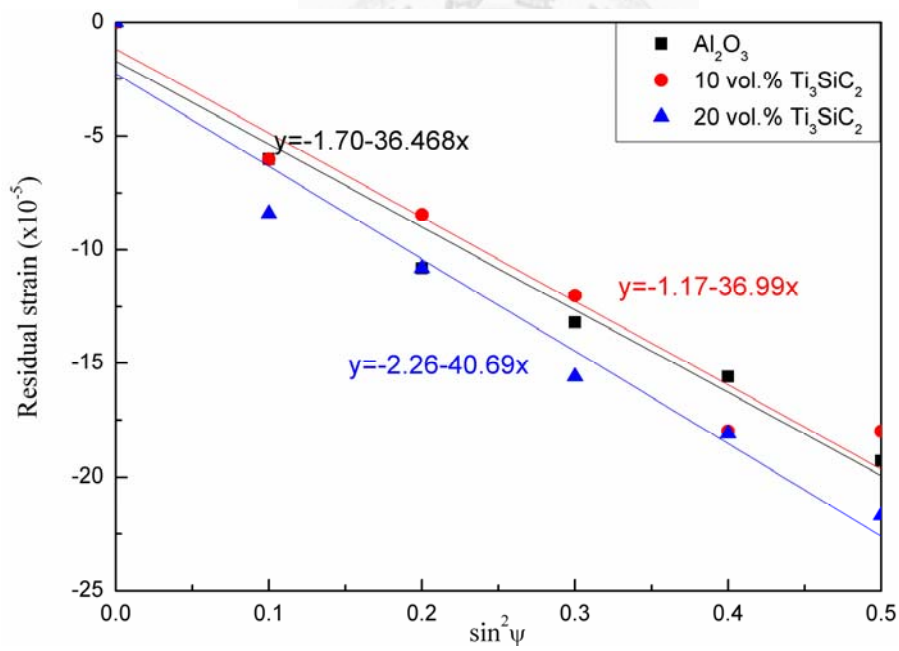


(b)

Fig. 5-8. Interactions between crack induced by indentation and Ti_3SiC_2 inclusions.



(a)



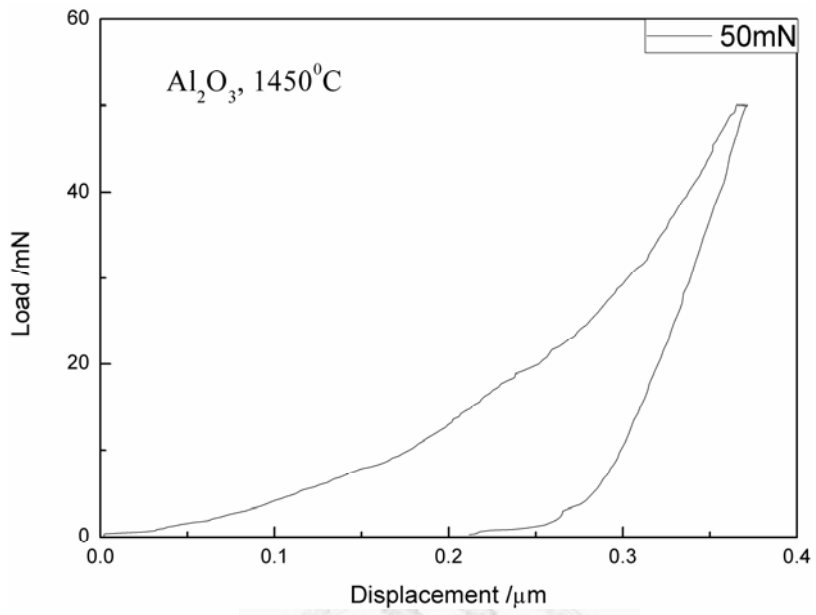
(b)

Fig. 5-9. Relationship of residual strain and the $\sin^2 \psi$ of the monolithic Al₂O₃ and Al₂O₃/Ti₃SiC₂ composites hot-pressed at 1400°C and 1450°C. (a) Hot-pressing at 1400°C with 10 and 20 vol.% Ti₃SiC₂ addition, and (b) Hot-pressing at 1450°C with 10 and 20 vol.% Ti₃SiC₂ addition.

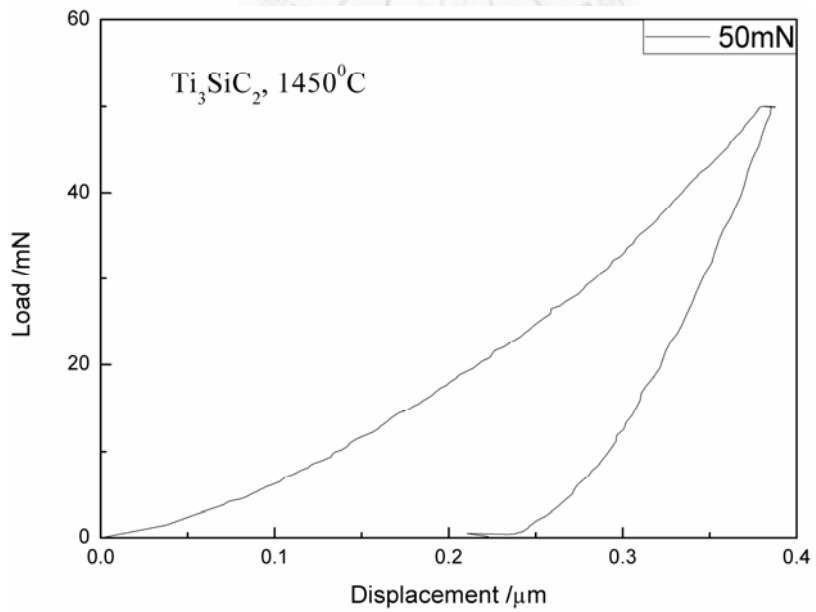
small and varied within a small range, indicating that the addition of Ti_3SiC_2 affects little on the resulting residual stress. It further confirms that the difference between the thermal expansion coefficients of Al_2O_3 and Ti_3SiC_2 is small.

5.3.4 Nanoindentation results

In order to modify the localized toughening effects in the composite, the nanoindentation skill is introduced to analyze the elastic modulus and energy-absorbing ability of the matrix and reinforcement individually. During the nano-indentation test, the load-displacement curve is recorded. Fig. 5-10 shows the typical load – displacement curves by using the nano-indentation with a load of 50 mN. The localized elastic modulus and hardness for Al_2O_3 matrix and Ti_3SiC_2 inclusion within the composite can be calculated from these curves. The fracture energy can also be calculated by measuring the area under the curve. The area under the curve for Ti_3SiC_2 inclusion is larger than that for Al_2O_3 matrix. The calculated results are shown in Table 5-3. Both the elastic modulus and hardness of Ti_3SiC_2 are lower than those of Al_2O_3 . However, the fracture energy absorbed by the Ti_3SiC_2 inclusion is larger than that of Al_2O_3 matrix.



(a)



(b)

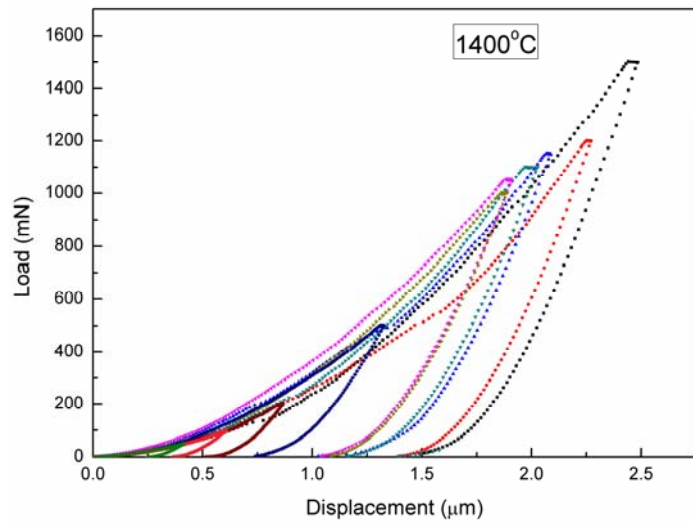
Fig. 5-10. Typical load-displacement curves for (a) Al₂O₃ matrix and (b) Ti₃SiC₂ inclusion in the composite prepared by hot-pressing at 1450°C.

Table 5-3. Localized elastic modulus, hardness and fracture energy of the Al₂O₃ matrix and Ti₃SiC₂ inclusion in the composites as determined by nano-indentation.

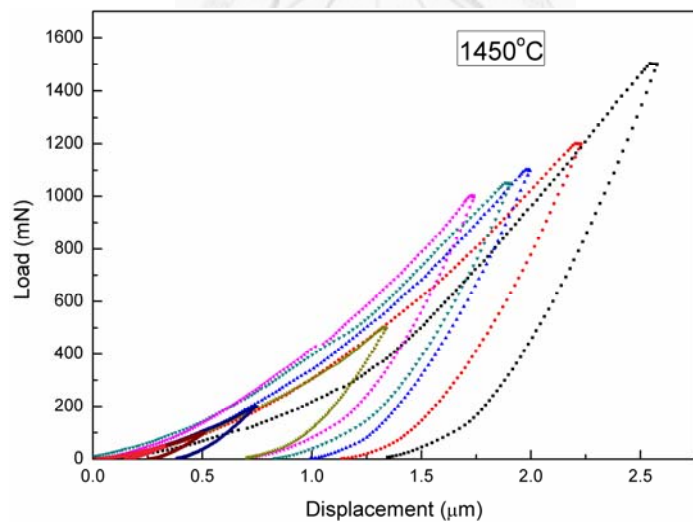
Hot-pressing temperature / °C	1400°C		1450°C	
Materials	Al ₂ O ₃ matrix	Ti ₃ SiC ₂ inclusion	Al ₂ O ₃ matrix	Ti ₃ SiC ₂ inclusion
Elastic modulus / GPa	418±13	378±10	400±3	353±4
Hardness / GPa	21.1±2.7	18.3±1.5	18.5±1.1	15.4±0.3
Fracture energy (load:50 mN)/ nJ	6.0±0.2	6.2±0.5	5.8±0.1	7.1±0.6

Fig. 5-11(a) and Fig. 5-11(b) plot the load – displacement results of Ti_3SiC_2 phase in the $\text{Al}_2\text{O}_3/20 \text{ vol.}\%-\text{Ti}_3\text{SiC}_2$ composite hot-pressed at 1400°C and 1450°C with the load from 50 mN to 1500 mN, respectively. The area under the load-displacement curves increases with the increase of load. The elastic modulus of the Ti_3SiC_2 particles as evaluated from the unloading curve is shown in Fig. 5-12. The elastic modulus is close to a constant value as the maximum load is smaller than 900 mN, then decreases rapidly above 900 mN. It indicates that a load > 900 mN is needed to induce significant delamination within the Ti_3SiC_2 particle. Generally, the elastic modulus of Ti_3SiC_2 phase in the composite hot-pressed at 1400°C is higher than 1450°C , which shows a good agreement to the ultrasonic analysis results in Table 5-2.

Fig. 5-13(a) represents the total fracture energy (W_{tot}) of Ti_3SiC_2 phase in the $\text{Al}_2\text{O}_3/20 \text{ vol.}\%-\text{Ti}_3\text{SiC}_2$ composite hot-pressed at 1400°C and 1450°C measured by nanoindentation with the load from 50 mN to 1500 mN, respectively. The results of W_{tot} were calculated from the measures of the curves shown in Fig. 5-11. The results of elastic fracture energy (W_e) can also be obtained from the elastic region of the total integration area, which is shown in Fig. 5-13(b). To subtract W_e from W_{tot} , we can obtain the plastic fracture energy (W_p), which was plotted in Fig. 5-13(c). A similar trend was observed in these three figures. With lower indentation load (50~500 mN),



(a)



(b)

Fig. 5-11. Load–displacement results of Ti_3SiC_2 phase in the $\text{Al}_2\text{O}_3/20 \text{ vol.}\% \text{-Ti}_3\text{SiC}_2$ composite with the load from 50 mN to 1500 mN. (a) hot-pressed at 1400°C , (b) hot-pressed at 1450°C .

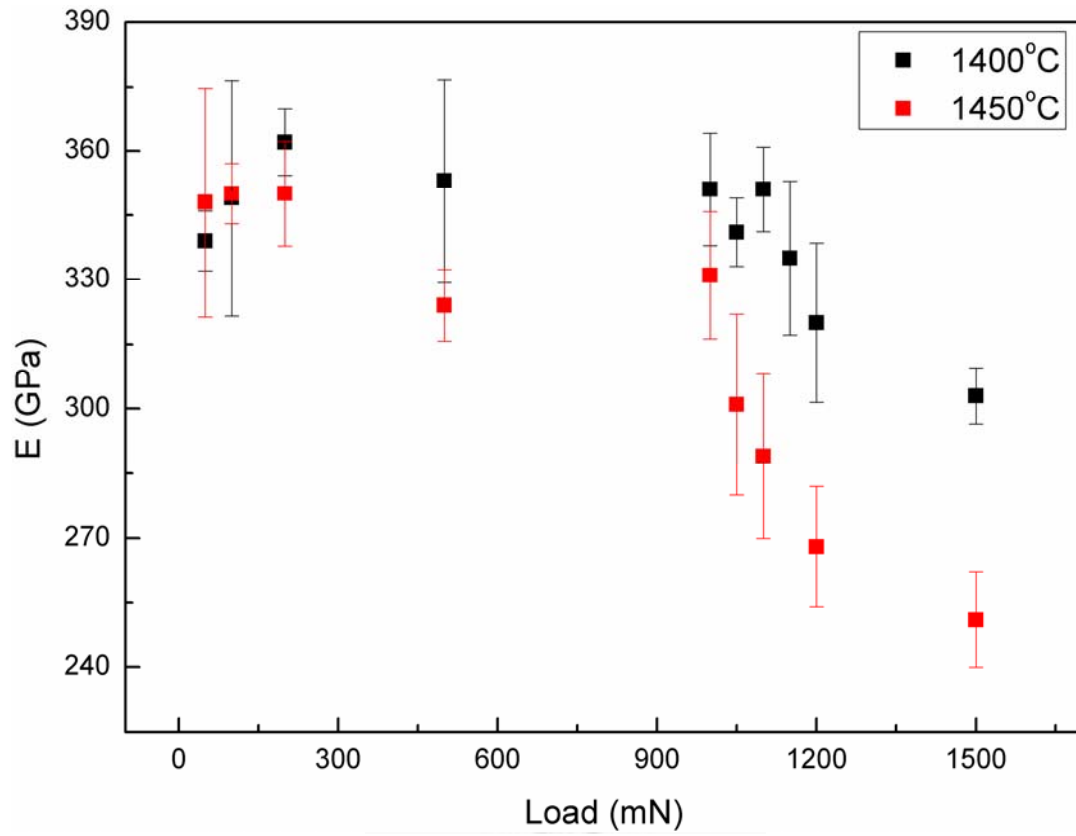


Fig. 5-12. Elastic moduli of Ti_3SiC_2 phase in the $\text{Al}_2\text{O}_3/20 \text{ vol.}\%-\text{Ti}_3\text{SiC}_2$ composites measured by nanoindentation with the load from 50 mN to 1500 mN, respectively.

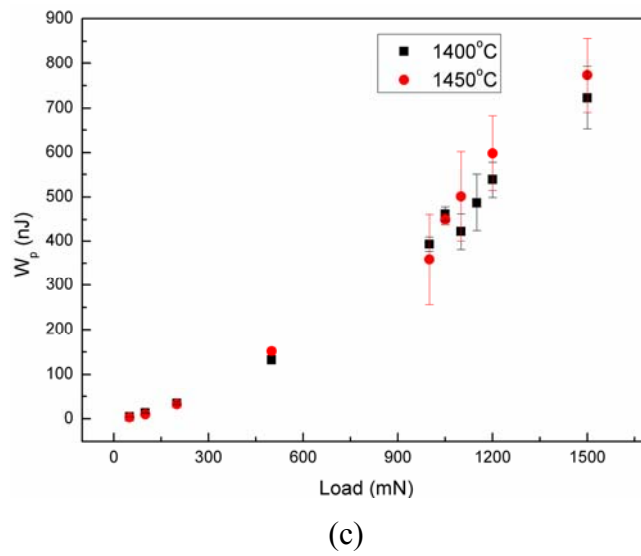
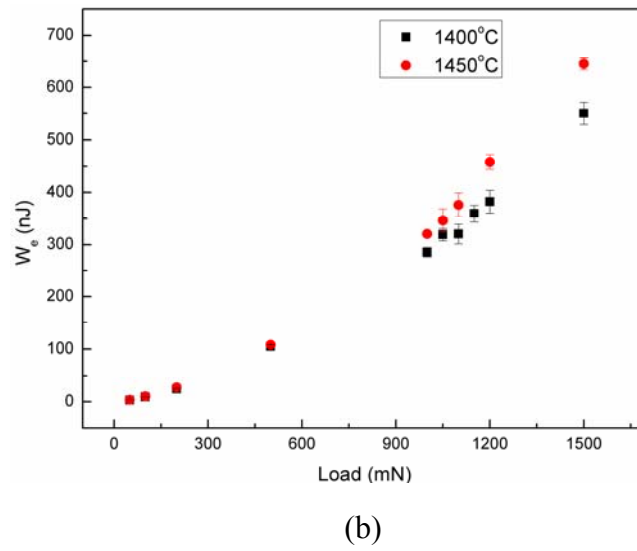
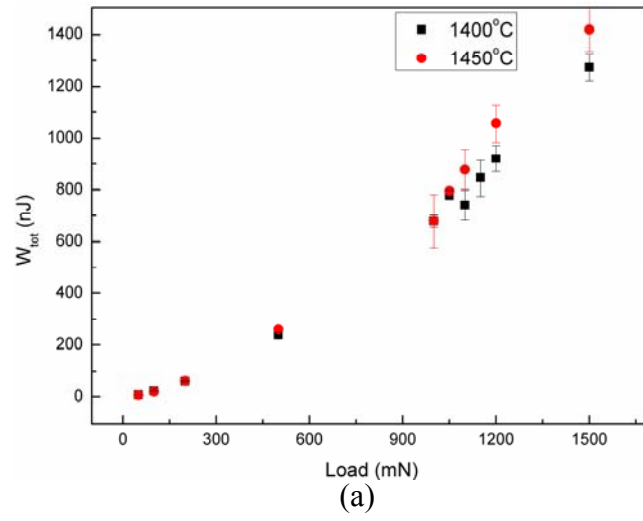
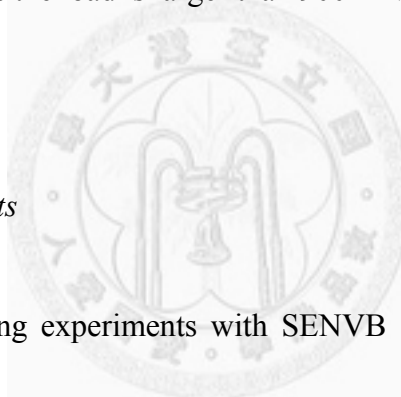


Fig. 5-13. Fracture energy of Ti_3SiC_2 phase in the $\text{Al}_2\text{O}_3/20 \text{ vol.}\% \text{-Ti}_3\text{SiC}_2$ composite hot-pressed at 1400°C and 1450°C measured by nanoindentation with the load from 50 mN to 1500 mN. (a) W_{tot} , (b) W_e and (c) W_p , respectively.



the W_{tot} , W_e and W_p of Ti_3SiC_2 phase in the composite hot-pressed at $1400^\circ C$ are about the same as those in the composite hot-pressed at $1450^\circ C$. With higher indentation load (1000~1500 mN), the W_{tot} , W_e and W_p of Ti_3SiC_2 phase in the composite hot-pressed at $1450^\circ C$ are higher than those in the composite hot-pressed at $1400^\circ C$. Moreover, the W_p of Ti_3SiC_2 phase hot-pressed at $1400^\circ C$ seems to have a sudden decrease at a load of 900 mN and the standard deviation becomes larger from this load. And the W_p of Ti_3SiC_2 phase hot-pressed at $1450^\circ C$ also seems to have a larger standard deviation as the load is larger than 900 mN.



5.3.5 R-curve measurements

The four-point bending experiments with SENVB samples under stable crack growth were successfully performed. The investigated R-curves are given in Fig. 5-14. Due to the possible inaccuracy of the measurement of crack lengths by using in-situ optical microscopy during 4-point bending test under stable crack growth, the optically determined crack length on the sample surface had to be corrected by a constant offset. The first data points in Fig.5-14 for both materials (at $\Delta a = 0$) were calculated by using Eq. 2-3 with the prepared initial crack lengths and the maximum attained force. Assuming that the compliance of the sample changes only due to crack propagation, the offset, which is supposed to be independent of the crack length, can

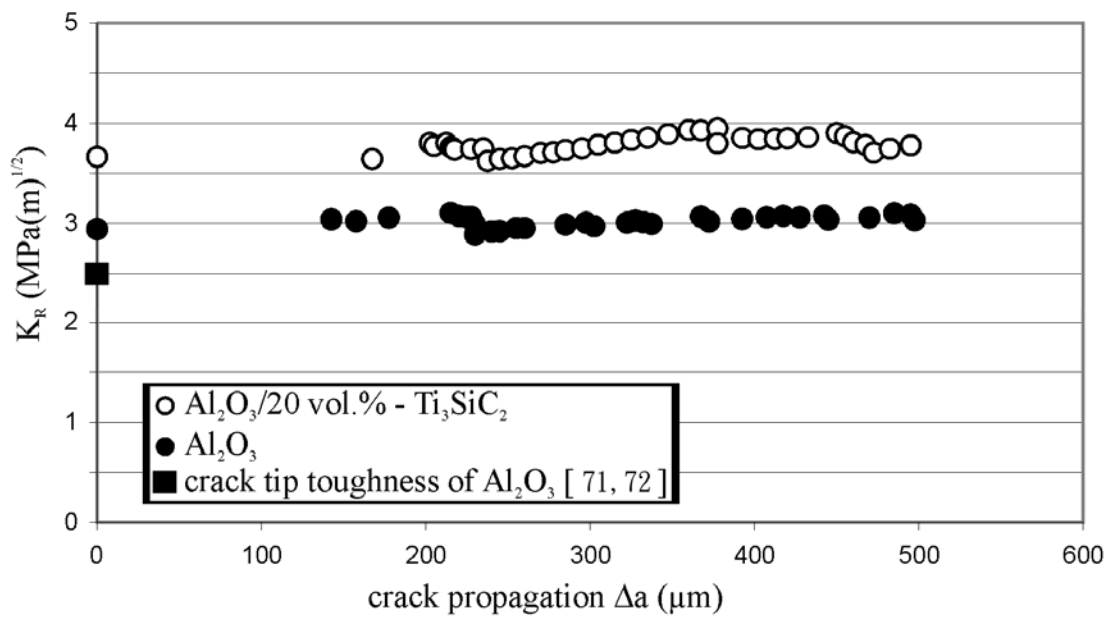


Fig. 5-14. Crack-growth-resistance curves of Al₂O₃ and Al₂O₃/20 vol.%-Ti₃SiC₂ composite hot-pressed at 1450°C under stable-crack-growth behavior. The crack-tip toughness of alumina [71,72] are also added as references.

be determined by comparing two measurements (of the same material) with different initial notch lengths. The details can be found in ref. 69. The constant offset for the present study is 120 μm . This crack length was added to all the optically determined crack lengths during the measurement. The given crack lengths values in Fig. 5-14 were already corrected.

The monolithic alumina exhibits a constant value of toughness, which is equal to (3.02 ± 0.06) $\text{MPa}\sqrt{\text{m}}$. The $\text{Al}_2\text{O}_3/20$ vol.-%- Ti_3SiC_2 composite also shows a constant toughness of (3.90 ± 0.10) $\text{MPa}\sqrt{\text{m}}$, which has the toughness increase of 0.9 $\text{MPa}\sqrt{\text{m}}$. The first data point of the $\text{Al}_2\text{O}_3/20$ vol.-%- Ti_3SiC_2 composite in Fig. 5-14, which is equal to 3.7 $\text{MPa}\sqrt{\text{m}}$, can be influenced and over-estimated by the finite notch root radius [69]. The amount of over-estimation depends on notch radius, r_N , and the pre-existing defect [20]. If the crack has propagated by more than $\Delta a = 1.5 r_N$, there is no more significant influence of notch radius on the fracture toughness [70]. In the present study, each measurement was performed under $\Delta a > 1.5 r_N$. Therefore, the notch effect can be neglected.

The former studies of crack-tip toughness for alumina, which in the range of 2.3~2.8 $\text{MPa}\sqrt{\text{m}}$, are also listed in Fig. 4-14 as a comparison [71,72]. To compare with the measured values, there might be a very steep R-curve before the first data point. Considering the further calculation of theoretical toughness increase in the

present study, the average value of 2.5 MPa \sqrt{m} was shown in this figure as a typical value.

5.4 Discussion

5.4.1 Strengthening mechanism

The thermal expansion coefficient and elastic modulus of Al₂O₃ are very close to those of Ti₃SiC₂, therefore the addition of Ti₃SiC₂ inclusions affects little on the magnitude of the residual stress within the Al₂O₃ matrix. The influence of residual stress can thus be ignored. The Al₂O₃-Ti₃SiC₂ composite can be seen as a model system. The strength of Al₂O₃/Ti₃SiC₂ composites is slightly higher than that of Al₂O₃ alone. The particle size of monolithic Al₂O₃ (~3.5 μm) is slightly larger than that of Al₂O₃ matrix in the composites (~3 μm). The size of the Ti₃SiC₂ inclusions is close to that of Al₂O₃ grains. The pinning effect inserted by the Ti₃SiC₂ inclusions on the growth of Al₂O₃ matrix is thus limited. Nevertheless, the microstructure refinement can contribute partly to the strength enhancement. However, it is also worth noting that the fracture mode is changed from intergranular type for Al₂O₃ to transgranular type for composite. The change of fracture mode may also affect partly the resulting

strength [71-72]. Unlike the other composites, the presence of weak matrix/reinforcement interface is detrimental to the strength of composites. Since the length of weak interface is smaller than that of inclusion, the presence of such weak layers is not harmful to the strength of the brittle ceramic matrix.

5.4.2 Toughening mechanism

Barsoum et al. indicated that polycrystalline Ti_3SiC_2 can be compressed cyclically with a load up to 1 GPa, around 25% mechanical energy is consumed during cyclic loading. It has been related to the formation of kink bands [75]. Apart from kink bands, TEM observation reveals the presence of delamination within single crystal after nano-indentation at a load of >20 mN [53,76]. It suggested that the weak layers within the Ti_3SiC_2 crystal dominated the fracture behavior.

In the present study, it demonstrates that the addition of Ti_3SiC_2 inclusions enhances the toughness of Al_2O_3 . The toughness values as shown in Fig. 5-6 are obtained by using the indentation technique. The crack induced by the indentation is around 200 μm . The length of the indentation crack is much larger than the size of Ti_3SiC_2 inclusions. The large data scatter for the 10% composite (Fig. 5-6) implies that the distribution of the Ti_3SiC_2 inclusions within Al_2O_3 matrix is not very uniform. However, the data scatter is reduced by increasing the Ti_3SiC_2 content to 20%. It

suggests that the microstructure uniformity is improved by adding more Ti_3SiC_2 inclusions.

The elastic modulus (Table 5-2) and Vickers hardness (Fig. 5-5) of alumina is decreased after the addition of Ti_3SiC_2 inclusions. These values represent the average properties of the composites. However, the toughening behaviour of the composite is dominated by the mechanical behaviour of each phase in the composites. In order to determine the mechanical properties of each phase within the composite, the nano-indentation is conducted. The load applied is 50 mN. By using such load, an indent with a displacement of $0.3\ \mu\text{m}$ is introduced into the Al_2O_3 grain and Ti_3SiC_2 inclusion (Fig. 5-10). Such indent size is smaller than the size of Al_2O_3 grain and Ti_3SiC_2 inclusion. The mechanical properties of each phase can thus be measured. From Table 5-2, the elastic modulus of the Ti_3SiC_2 inclusion is indeed lower than that of Al_2O_3 matrix. The hardness of the Ti_3SiC_2 inclusion is therefore lower than that of Al_2O_3 matrix. Since the thermal expansion coefficient is similar for the Al_2O_3 and Ti_3SiC_2 phases, the difference in elastic constant plays an important role on the interaction between crack and inclusions. The crack tends to propagate into the phase with lower elastic modulus [77] and the crack is thus attracted to the Ti_3SiC_2 inclusions, as demonstrated in Fig. 5-8.

Although no reaction layer is observed at the $\text{Al}_2\text{O}_3/\text{Ti}_3\text{SiC}_2$ interface, the interface is suspected to be a strong one. It is based on the fact that the pull-out of complete Ti_3SiC_2 inclusions is hardly observed on the fracture surface (Fig. 5-7(b)). Furthermore, a major crack tends to penetrate into Ti_3SiC_2 inclusions (Fig. 5-8(b)). In any case, it implies that the strength at $\text{Al}_2\text{O}_3/\text{Ti}_3\text{SiC}_2$ interface is higher than the strength of the weak layer within the Ti_3SiC_2 inclusions. Due to the presence of weak layers within the Ti_3SiC_2 inclusions, the major crack can then propagate through the weak layers. The nano-indentation analysis indicates that the Ti_3SiC_2 inclusion can consume more fracture energy (Table 5-3). It can be related to the delamination and fracture of the weak layers within the Ti_3SiC_2 inclusion (Fig. 5-7(c)). The toughness is therefore enhanced. A schematic to demonstrate the toughening mechanism is shown in Fig. 5-15. In the figure, a crack is propagating into a Ti_3SiC_2 inclusion, deflecting by the weak internal layers for several times. The same crack deflection process can also take place in a nearby Ti_3SiC_2 inclusion.

Previous studies indicated that both the strength and toughness of Al_2O_3 can be improved by adding Ti_3SiC_2 inclusions [55-57]. The strengthening effect is related to the pinning effect provided by the Ti_3SiC_2 inclusions. The microstructure refinement contributes to their strength enhancement. In the present study, the microstructure refinement after the addition of Ti_3SiC_2 inclusions is also noted. One more

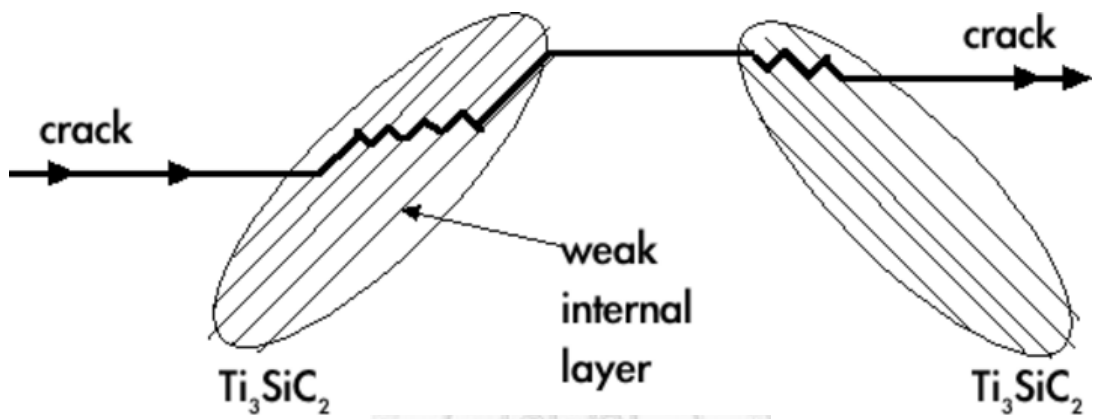


Fig. 5-15. Schematic for the interactions between crack and the reinforcement with weak internal layers. The crack is deflected within the reinforcement.

strengthening mechanism, grain boundary strengthening, may also take place. The toughening mechanism for the $\text{Al}_2\text{O}_3/\text{Ti}_3\text{SiC}_2$ composite has received relatively less attention. In the present study, the nano-indentation analysis reveals that more fracture energy is consumed during the fracturing of Ti_3SiC_2 crystal. Assisted by the detailed microstructure observation, the cleavages within Ti_3SiC_2 inclusion are also observed. It demonstrates that the toughness enhancement is contributed by the delamination at the weak internal layers within the toughening inclusions.

5.4.3 Contribution of plastic deformation of Ti_3SiC_2 to the crack deflection in the $\text{Al}_2\text{O}_3/\text{Ti}_3\text{SiC}_2$ composites

The distribution of the Ti_3SiC_2 particles within Al_2O_3 matrix is uniform. The aspect ratio of the Ti_3SiC_2 particles is larger than unity and thus plays an important role for toughening. A quantitative metallographic technique [78], which had been developed to estimate the aspect ratio of elongated silicon nitride grains, is adopted in the present study to determine the aspect ratio of Ti_3SiC_2 particles. The size of the Ti_3SiC_2 particles and their aspect ratio is shown in Table 5-4. The coarsening of Ti_3SiC_2 particles in the Al_2O_3 matrix after hot-pressing is not observed. The aspect ratio of the Ti_3SiC_2 particles is similar in the 10% and 20% composites. The electrical resistance of the $\text{Al}_2\text{O}_3/20\%\text{Ti}_3\text{SiC}_2$ composite is much lower than that of the

Table 5-4. Microstructure characteristics and mechanical properties of monolithic Al₂O₃ and Al₂O₃/Ti₃SiC₂ composites. The specimens were hot-pressed at 1450°C.

Material	Al ₂ O ₃	Al ₂ O ₃ /10%Ti ₃ SiC ₂	Al ₂ O ₃ /20%Ti ₃ SiC ₂
Relative density / %	99	98	96
Size of Al ₂ O ₃ grains / μm	~3.5	~3	~3
Size of Ti ₃ SiC ₂ particles / μm	-	4~5	4~5
Aspect ratio of Ti ₃ SiC ₂ particles	-	2.4	2.5
Hardness / GPa	22.6±1.2	19.1±2.6	18.6±1.4
Elastic modulus* / GPa	390	375	366
Fracture toughness** / MPam ^{0.5}	4.5±0.1	5.1±0.3	6.2±0.1

*note: determined by ultrasonic reflection technique at 5 MHz.

**note: determined by indentation technique at 98 N.

$\text{Al}_2\text{O}_3/10\%\text{Ti}_3\text{SiC}_2$ composite, indicating that the percolation threshold for the Ti_3SiC_2 particles is in the range between 10 vol% and 20 vol%. The inter-connectivity of the Ti_3SiC_2 particles has little effect on the coarsening of the Ti_3SiC_2 particles. It may be due to that the hot-pressing temperature is not high enough for the Ti_3SiC_2 particles to grow. The size of the Ti_3SiC_2 particles in the composites is the same as that of the starting particles. It suggests that the size and shape of the starting Ti_3SiC_2 particles remain the same after densification. The Ti_3SiC_2 particles were prepared by a reaction process [59-61], followed by a milling process. Since the dislocations can glide only along the basal planes in the Ti_3SiC_2 crystal, fracture tends to take place on the basal plane of the Ti_3SiC_2 particle. The shape of the Ti_3SiC_2 particles is thus elongated, and the long-axis of the Ti_3SiC_2 particles tends to be parallel to the basal plane. As a crack pops into one Ti_3SiC_2 particle within the Al_2O_3 matrix, the crack tends to be deflected along the long-axis of the particle. The change of crack direction reduces stress intensity near crack tip [79]. The crack deflection also increases the length of the crack path [80]. No matter the crack is deflected along the external interface or within the reinforcement, the amount of toughness enhancement increases with the increase of the length of crack path. The length of crack path depends strongly on the shape of the reinforcement. The toughness enhancement increases with the increase of the aspect ratio [79]. The aspect ratio of elongated rod is larger than that of spherical

particles; the toughness enhancement for the fiber-reinforced ceramic is thus higher than that of the particle-reinforced ceramics. For the $\text{Al}_2\text{O}_3/\text{Ti}_3\text{SiC}_2$ composites, the aspect ratio of the Ti_3SiC_2 particles is around 2.5. By using the theory developed by Faber and Evans [79], the fracture energy ratio of the composite over matrix, as induced by crack deflection around cylindrical rods with aspect ratio of 2.5, is 1.8 and 2.0 for the 10% and 20% composite, respectively. The theoretical predictions for the composites containing 10 vol% and 20 vol% elongated rods are 5.9 and $6.2 \text{ MPam}^{0.5}$, respectively. The experimental data, see Table 5-4, match well with the theoretical predictions.

In order to deflect a crack within a Ti_3SiC_2 particle, weak interface or layer are needed. The shear strength of the basal plane of Ti_3SiC_2 crystal is very high, around 3 GPa [81]. Nevertheless, as the Ti_3SiC_2 particle is under an external load, the accumulation of dislocations can induce the formation of delamination on basal plane. Within a polycrystalline Ti_3SiC_2 solid, a normal force around 489 MPa is capable to activate a crack to propagate from the delamination [52]. Therefore, it is very likely that the delamination is formed before the reach of the crack. In order to quantify the conditions for the formation of delamination in Ti_3SiC_2 particle, the load-displacement behaviour for the Ti_3SiC_2 particles within Al_2O_3 matrix under load is investigated. The load was applied through a nano-indenter. The technique is very

valuable to estimate the response of the Ti_3SiC_2 phase under an external load [52,76,81-83].

As reported by Molina-Aldareguia et al [52], a load as small as 30 mN applied by the nano-indentation is enough to introduce delamination into the thin Ti_3SiC_2 film. For polycrystalline Ti_3SiC_2 solid, a load of 500 mN is needed to induce delamination [52]. In the present study, a load of 900 mN is needed to induce significant plastic-deformation within the Ti_3SiC_2 particles (Fig. 5-12). The Ti_3SiC_2 thin film prepared by Molina-Aldareguia et al was deposited onto a MgO substrate, a relatively soft substrate [84]. The constraint on thin film is thus small. For polycrystalline Ti_3SiC_2 solid [52], each Ti_3SiC_2 particle is constrained by its neighboring Ti_3SiC_2 grains. The constraint on each particle is therefore larger; a load of 500 mN is thus needed to induce delamination. The reported values for the elastic modulus of Ti_3SiC_2 solid varied in the range from 280 GPa to 330 GPa [60,85], depending on the amount of impurity. The elastic modulus of the Ti_3SiC_2 is slightly lower than that of Al_2O_3 (400 GPa, Table 4-3), therefore the decrease of the elastic modulus of $\text{Al}_2\text{O}_3/\text{Ti}_3\text{SiC}_2$ composite is due to the addition of Ti_3SiC_2 particles, see Table 5-2. Since the elastic modulus of Al_2O_3 is higher than that of Ti_3SiC_2 , a higher load is needed to allow the plastic deformation to take place.

The strength of monolithic alumina is around 400 MPa. The tensile stress needed to activate the unstable crack growth within Al_2O_3 matrix is expected smaller than the value. For polycrystalline Ti_3SiC_2 solid, a normal stress of 489 MPa is needed to activate unstable crack growth. A higher stress is needed to allow a crack to grow within Ti_3SiC_2 particles as they are embedded within Al_2O_3 matrix. For the $\text{Al}_2\text{O}_3/\text{Ti}_3\text{SiC}_2$ composite, the delamination within the Ti_3SiC_2 particles is thus likely formed before the fracture process. The starting Ti_3SiC_2 particles have been treated with a milling process. The milling force is large enough to fracture large Ti_3SiC_2 particles into small ones. The force is thus also large enough to induce damages, such as dislocations and delaminations, within the Ti_3SiC_2 particles. As the delamination is pre-existed within the Ti_3SiC_2 particle, the crack can then be deflected within the particle as demonstrated in the schematic diagram in Fig. 5-16. Since the delamination is taken place before the preparation of composites, the contribution of the plastic deformation to toughness enhancement is small. The toughness increase for the $\text{Al}_2\text{O}_3/\text{Ti}_3\text{SiC}_2$ composite is mainly contributed from the crack deflection. However, without the pre-existence of plastic deformation, the crack deflection within the Ti_3SiC_2 particles is not possible. Furthermore, the delamination is likely parallel to the long-axis of the Ti_3SiC_2 particle; the crack length induced by crack deflection is therefore long. Though the damage is pre-existed in the Ti_3SiC_2 particles, the strength

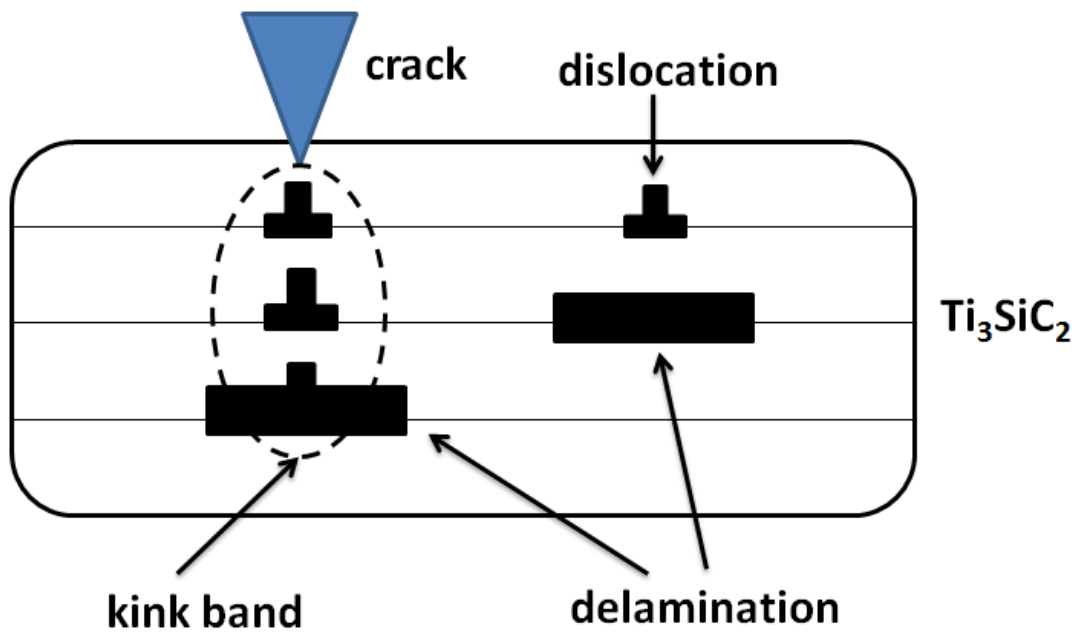


Fig. 5-16. Schematic for the interaction between crack and a Ti_3SiC_2 particle. The dislocations, kink-band and delamination may present within the Ti_3SiC_2 particle before the reach of the crack. The presence of delamination allows the crack to change its propagation direction.

of the Al_2O_3 is not affected after the addition of Ti_3SiC_2 particles. It is mainly due to that the length of delamination is smaller than that of Ti_3SiC_2 particles.

5.4.4 Contribution of crack-deflection-induced pullouts to the toughening effect in Al_2O_3/Ti_3SiC_2 composite

According to the exceptional plastic fracture behavior of Ti_3SiC_2 ceramic and its inner lamellae structure, the energy consumption during fracture may cause pullouts inside the lamellae. The pullout effect is generated by the frictional gliding of cylindrical elongated particles during the crack opening. The energy consumption of one pullout up to a pullout length, l^{po} , is [86] :

$$W = \int_0^{l^{po}} F dl = 2\pi r \Gamma_l (l^{po})^2 \quad (5-3)$$

where F is the applied force, l is the displacement and Γ_l is the interfacial shear stress (friction). Therefore the additional fracture energy ΔG^{po} due to pullout for a fully developed bridging zone under the assumption of small scale bridging zone is [86]:

$$\Delta G^{po} = \frac{NW}{A} = f \Gamma_l \frac{(l^{po})^2}{r} \quad \text{with} \quad N = f \frac{A}{\pi r^2} \quad (5-4)$$

where f is the volume fraction of the reinforcement, N is the number of bridges per unit area A , r is the radius of the bridging ligament. Here we define the fracture toughness K_{Ic} and the fracture energy G_{Ic} of composite are:

$$\begin{aligned} K_{Ic} &= K_{I0} + \Delta K^{po} \\ G_{Ic} &= G_{I0} + \Delta G^{po} \end{aligned} \quad \text{with} \quad \frac{K_{Ic}^2}{E} = G_{Ic} \quad (5-5)$$

where K_{I0} , G_{I0} are the intrinsic fracture toughness and fracture energy without toughening. ΔK^{po} , ΔG^{po} are the increases in fracture toughness and fracture energy due to pullout. E is the elastic modulus of the reinforcement. Therefore ΔG^{po} in Eq. 5-4 can be replaced from Eq. 5-5 as:

$$\Delta G^{po} = f\Gamma_l \frac{(l^{po})^2}{r} = \frac{K_{Ic}^2 - K_{I0}^2}{E} = \frac{2K_{I0} \cdot \Delta K^{po} + \Delta K^{po2}}{E} \quad (5-6)$$

Since the major toughening mechanism in $\text{Al}_2\text{O}_3/\text{Ti}_3\text{SiC}_2$ composite is attributed to crack deflection, the main crack tends to penetrate into Ti_3SiC_2 inclusions and is deflected within the lamellae structure, leading to pullout of debonded rectangular lamellae ligaments. Eq. 5-6 was applied in order to calculate the toughness increase of $\text{Al}_2\text{O}_3/20 \text{ vol.}\% \text{-Ti}_3\text{SiC}_2$ due to the pullout of ligaments. For the special case of the lamellae in Ti_3SiC_2 , the volume fraction f has to be modified because there is typically

a pullout effect in every second lamellae ligament within a Ti_3SiC_2 particle of diameter g . If we assume that there is a typical lamellae ligament of width d , we have $\frac{g}{d}$ ligaments in the lamellae and therefore f has to be replaced by $\frac{1}{2}f\frac{g}{d}$ because we assume that only every second lamellae counts for pullout. A schematic to demonstrate the pullout effect of toughening mechanism from top view is shown in Fig. 5-17. A representative SEM image of pullout during crack propagation demonstrates in Fig. 5-18. Thus Eq. 5-4 can be rewritten as:

$$W = \int_0^{l^{po}} Fdl = (g + d)\Gamma_l(l^{po})^2 \quad (5-7)$$

then Eq. 5-4 can be replaced by Eq. 5-7 such as:

$$\Delta G^{po} = \frac{NW}{A} = \left(\frac{1}{2}f\frac{g}{d}\right)\frac{g+d}{g^2}\Gamma_l(l^{po})^2 = \frac{1}{2}f\frac{g+d}{gd}\Gamma_l(l^{po})^2 = \frac{2K_{I0} \bullet \Delta K^{po} + \Delta K^{po^2}}{E} \quad (5-9)$$

Finally, the theoretical toughness increase by pullouts inside the lamellae of particle ΔK^{po} can be calculated. The following values were used as material constants: the elastic modulus E of Ti_3SiC_2 phase in the composite is 353 GPa (see Table 5-3), the particle size g (diameter) of Ti_3SiC_2 is 5 μm , the average lamellae ligament width d is

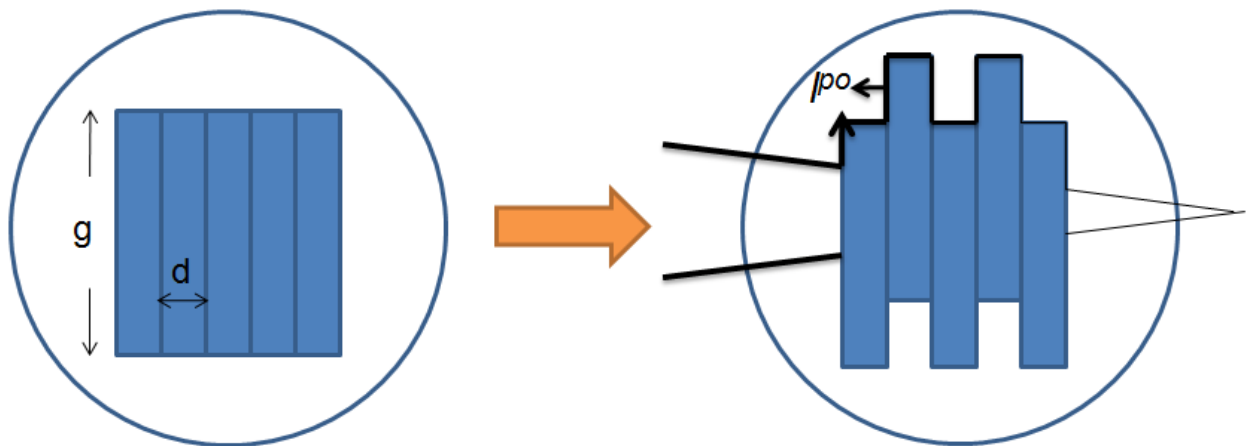


Fig. 5-17. A schematic to demonstrate the pullout effect inside the rectangular lamellae structure for toughening. Left-hand side: before a crack passes; right-hand side: after a crack passes, the pullouts of lamellae consume the fracture energy and the composite is thus toughened.

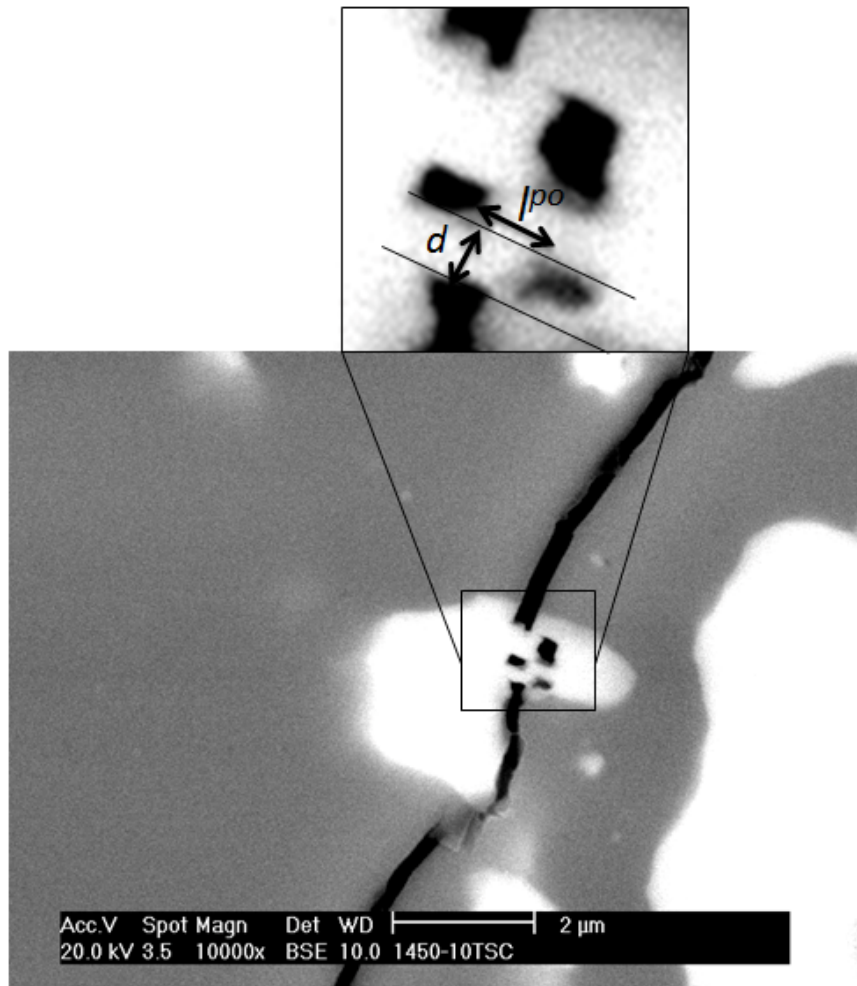


Fig. 5-18. Microstructure of pullouts inside the $\text{Al}_2\text{O}_3/\text{Ti}_3\text{SiC}_2$ composite during crack propagation.

~200 nm and the interfacial shear stress Γ_I is 2.5 GPa [81]. According to the previous study on SiC-whisker-reinforced alumina, the observed upper limit value of l^{po}/d is ~2 (where $d = 2r$) [86]. Thus the maximum l^{po} of Ti_3SiC_2 ligament during fracture is supposed to be 0.4 μm . In the present study, K_{I0} ($= 3.7 \text{ MPa}\sqrt{\text{m}}$) of the composite measured under stable crack growth may due to the presence of a steep R-curve during the original few microns of the crack propagation. Therefore, for theoretical calculation, the value of K_{I0} we use in the present study is $2.5 \text{ MPa}\sqrt{\text{m}}$, which is in the range of $2.3 \sim 2.8 \text{ MPa}\sqrt{\text{m}}$ [71,72]. Therefore, we can make some estimations of the theoretically expected toughness increase by changing the values of Γ_I from 0.1 GPa to 2.5 GPa, which is shown in Fig. 5-19. A comparison with the experimental results from Vickers indentation and the SEVNB method is also added in Fig. 5-19. The toughness increase measured by Vickers indentation is about $1.7 \text{ MPa}\sqrt{\text{m}}$, which indicates there are 27 % pullouts in the composite which contribute to the toughening effect when $\Gamma_I = 2.5 \text{ GPa}$. If $\Gamma_I = 0.5 \text{ GPa}$, the value measured by Vickers indentation is close to the theoretical value. Besides, the toughness increase measured by SEVNB method in the present study is about $0.9 \text{ MPa}\sqrt{\text{m}}$. To compare the SEVNB result with the theoretical calculation while $\Gamma_I = 2.5 \text{ GPa}$, the effective induced pullouts during fracture should be 14 %, which contribute to the toughening effect in $\text{Al}_2\text{O}_3/20 \text{ vol. \%Ti}_3\text{SiC}_2$ composite. If $\Gamma_I = 0.2 \text{ GPa}$, the value measured by SEVNB method is

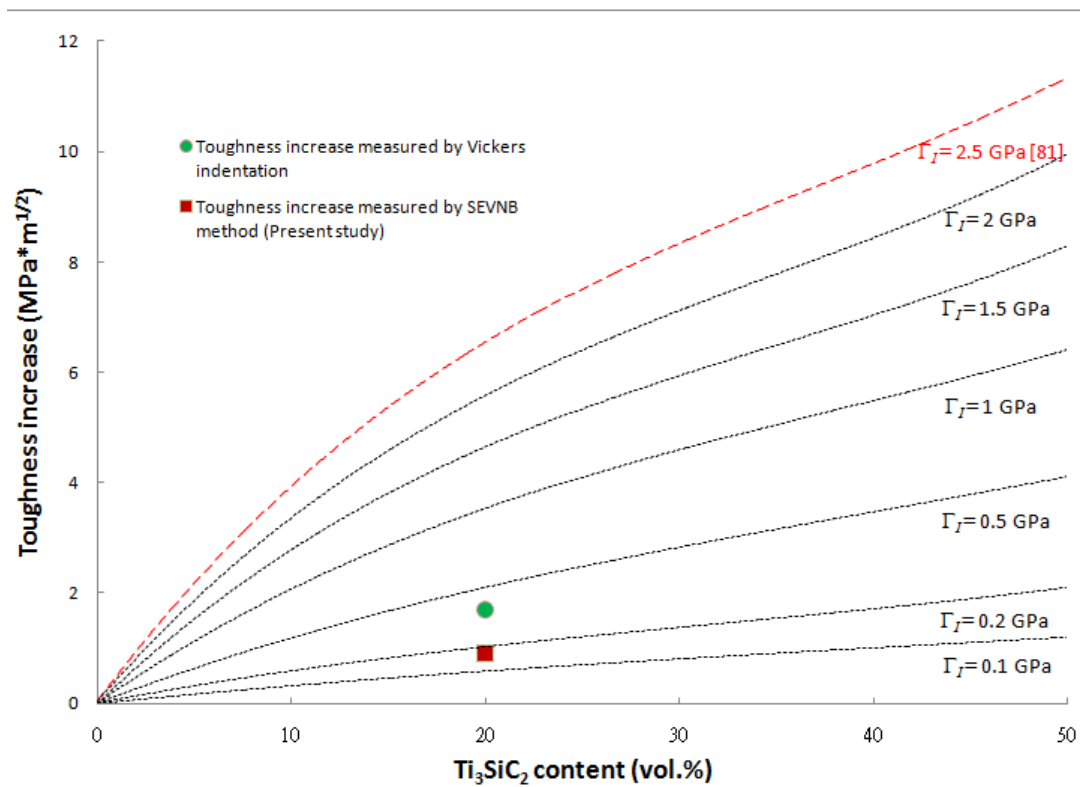


Fig. 5-19. Comparison with the theoretically expected toughness increase of Al₂O₃/Ti₃SiC₂ composite with 10 to 50 vol.% Ti₃SiC₂ content and the experimental results from Vickers indentation and SEVNB method with 20 vol.% Ti₃SiC₂ content.

close to the theoretical value.

According to Eq. 5-8, the parameters g and d also influence the pullout length and the toughness increase. The calculation of theoretical toughness increase influenced by varying particle size g and ligament width d was plotted in Fig. 5-20. However, when Γ_I is a constant value (2.5 GPa [81]), the change of g with a fixed value of d has nearly no influence on the toughness increase. On the other hand, the ligament width d dominates the pullout mechanism and therefore plays a major role in toughening. The toughness increase increases with increasing the ligament width. Comparing the theoretical calculation with the experimental results, the ligament width of pullouts in the composite is ~ 20 nm, which indicates that the former observation of average lamellae ligament width, 200 nm (Fig. 5-7(b)), might contain 10 single ligaments within each effective induced pullout during toughening.

There is one more thing which should be addressed in the present study. The orientation of Ti_3SiC_2 particle in composite also influences the toughening effect. After the sintering process, the orientations of Ti_3SiC_2 particles are randomly arranged in the alumina matrix. If the orientation of Ti_3SiC_2 particle is parallel to the direction of fracture, crack will penetrate directly through the inner weak interfaces between lamellae ligaments with no toughening effect, which can be observed in Fig. 5-21. To compare with the full-developed pullout model which is shown in Fig. 5-17, a

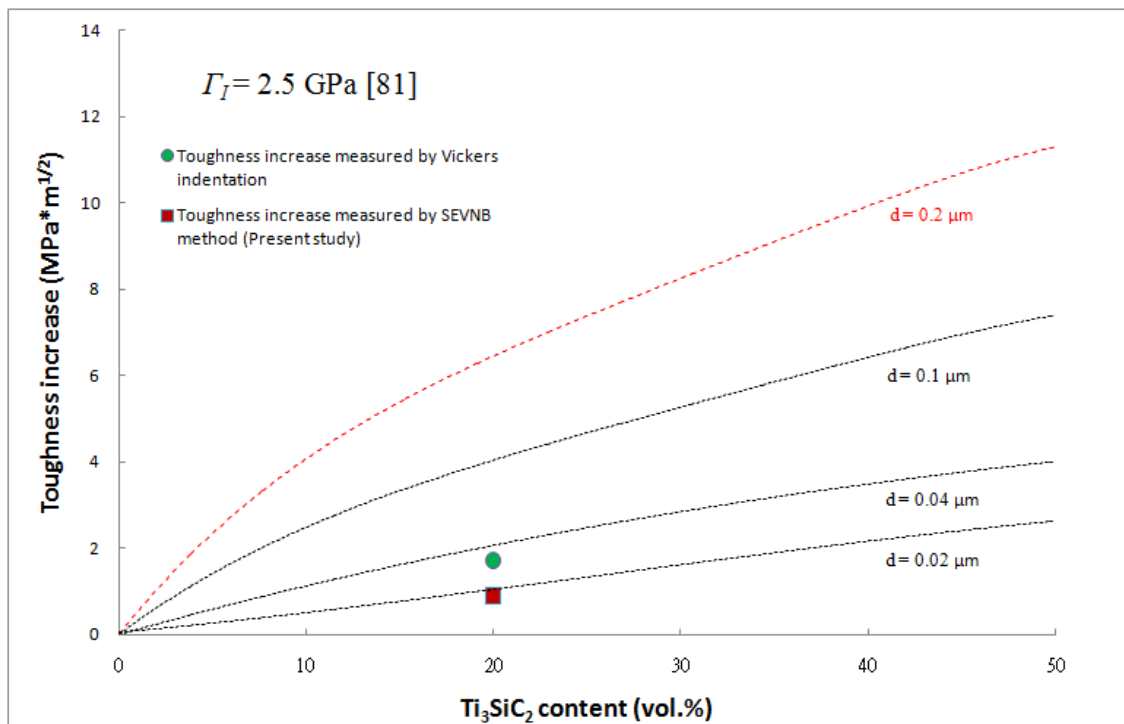


Fig. 5-20. Calculation of theoretical toughness increase with constant Γ_I influenced by varying particle size g and ligament width d . Each hypothetical line includes different values of g with fixed d .

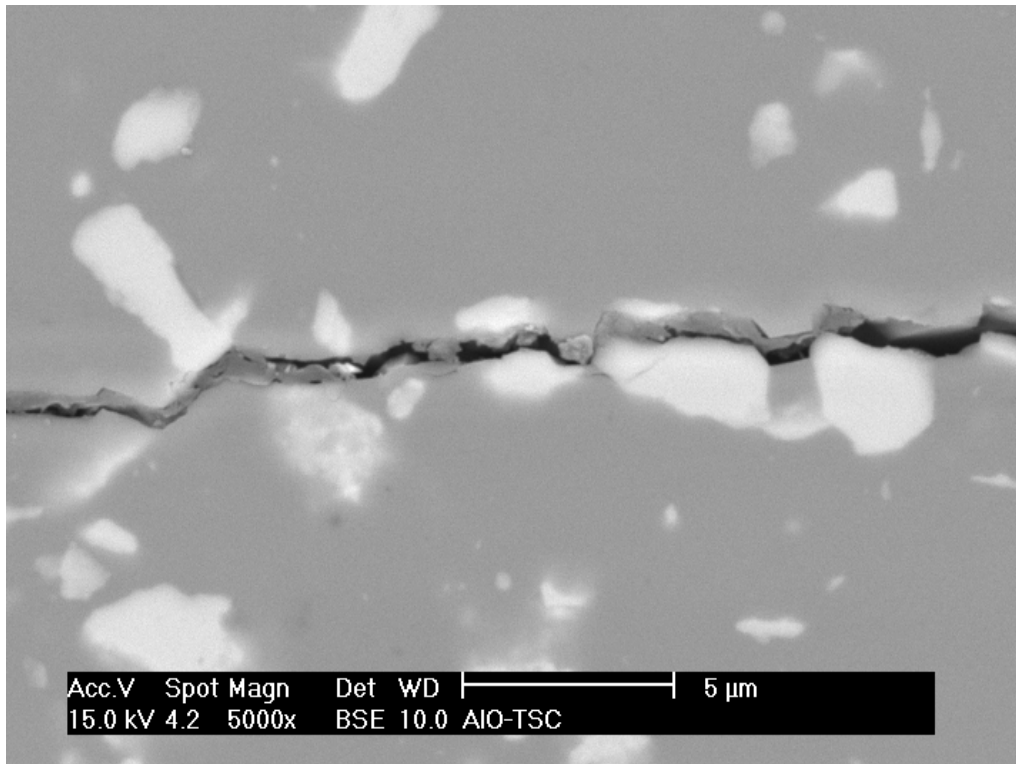


Fig. 5-21. Microstructure of non-pullouts inside the Al₂O₃/Ti₃SiC₂ composite when the orientation of Ti₃SiC₂ particle is parallel to the fracture direction.

schematic of non-toughening effect is demonstrated in Fig. 5-22. To conclude, if we can obtain a well-arranged orientation of Ti_3SiC_2 particles after sintering, the theoretical expected toughness increase of $\text{Al}_2\text{O}_3/20 \text{ vol.}\%-\text{Ti}_3\text{SiC}_2$ composite can be achieved up to $6.4 \text{ MPa}\sqrt{\text{m}}$ by fully generated pullouts when $\Gamma_7 = 2.5 \text{ GPa}$.

5.5 Conclusions

In the present study, a novel concept on the toughening brittle ceramic is proposed. As long as there are weak internal layers within the reinforcement, there is no need to form weak matrix/reinforcement interface. The $\text{Al}_2\text{O}_3/\text{Ti}_3\text{SiC}_2$ system is used as the model system to demonstrate such concept. Many weak internal layers are present within the Ti_3SiC_2 crystal. The cleavages of such weak internal layers can consume more fracture energy than that of the brittle matrix. Furthermore, the crack path is deflected within the Ti_3SiC_2 crystal. The toughness of alumina is therefore enhanced. Since the reaction between the matrix and Ti_3SiC_2 is not necessary to be avoided, the reinforcement with weak internal layers may be added into any brittle materials to improve their toughness. Since the crack deflection is taken place within the Ti_3SiC_2 particle because of the small damages made from the milling process, the ternary compound could be added into many brittle materials even when the particle

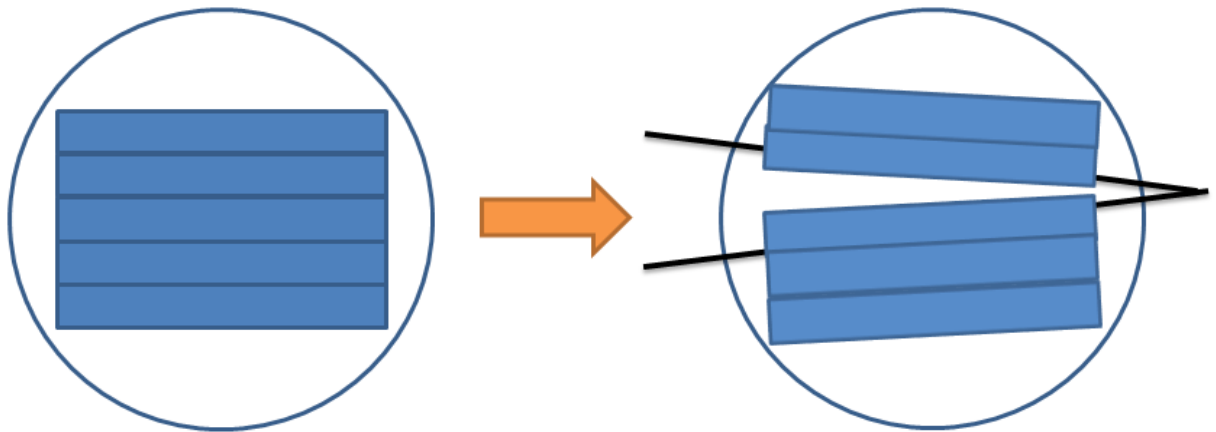
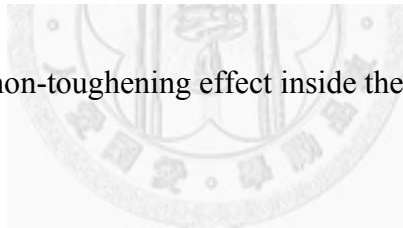


Fig. 5-22. A schematic of non-toughening effect inside the lamellae structure.



is bonded to the matrix materials. The damage within the Ti_3SiC_2 particle tends to be parallel to its long-axis. After densification, as a crack pops into a Ti_3SiC_2 particle within Al_2O_3 matrix, the crack tends to change its direction and propagate along the long-axis of the particle. The length of crack path is therefore long. Therefore, in order to take the advantages of using the Ti_3SiC_2 compound as toughening agent, the aspect ratio of Ti_3SiC_2 particles should be large.

The crack-growth-resistance curves of hot-pressed monolithic Al_2O_3 and $\text{Al}_2\text{O}_3/20$ vol.-%- Ti_3SiC_2 composite were determined via stable crack growth under SEVNB measurement in the present study. Although the composite only shows nearly no rising R-curve behavior during this measurement, it's believed that the toughening phenomenon has already been achieved with a steep curve during the original few microns of the crack propagation which cannot be obtained via in-situ optical microscope during stable crack growth in the 4-pt bending equipment. The measured toughness of the $\text{Al}_2\text{O}_3/20$ vol.-%- Ti_3SiC_2 composite is $3.9 \text{ MPa}\sqrt{\text{m}}$, which is toughened by the crack-deflection-induced pullouts inside the lamellae of Ti_3SiC_2 and dissipates the fracture energy. The effective induced pullouts during fracture should be 14 %, which contribute to the toughening effect in $\text{Al}_2\text{O}_3/\text{Ti}_3\text{SiC}_2$ composite. The theoretical calculation also indicates there's no influence on toughness increase by varying particle size. In contrast, the toughness increase increases with increasing

ligament width. Each effective induced pullout might contain 10 single ligaments during toughening.



Chapter 6: Conclusions

Toughening ceramic-matrix composite by incorporating reinforcements within weak internal layers is investigated by using three model systems in the present study. The general idea and the materials selection are based on using the reinforcements with higher CTE and lower elastic modulus. The compressive hoop stress around the matrix/reinforcement interface and the tensile radial stress are generated after sintering. The reinforcement can thus attract the crack which propagates into the reinforcement and then deflects or forms branches inside. The selected systems are $\text{Al}_2\text{O}_3/\text{BaTiO}_3$ -platelet, LTCC/ BaTiO_3 -platelet and $\text{Al}_2\text{O}_3/\text{Ti}_3\text{SiC}_2$ composites.

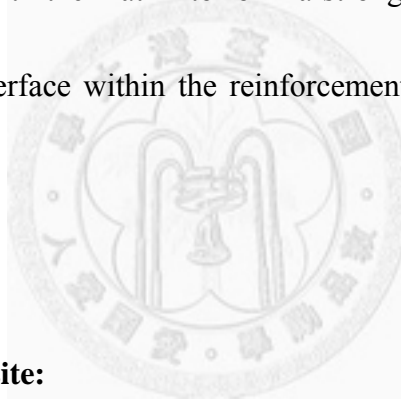
1. $\text{Al}_2\text{O}_3/\text{BaTiO}_3$ -platelet composite:

For $\text{Al}_2\text{O}_3/\text{BaTiO}_3$ -platelet system, the weak interfaces are located within the BaTiO_3 platelet. Although there is a reaction at the $\text{Al}_2\text{O}_3/\text{BaTiO}_3$ -platelet interface, due to the lower elastic modulus and higher energy dissipating ability of the platelet, the crack can penetrate into it and form branches.

2. LTCC/ BaTiO_3 -platelet composite:

For the LTCC/BaTiO₃-platelet system, the R-curve behavior is observed by using the indentation-fracture-strength method. The fracture surface of the composite indicates the fracture direction tends to trespass inside the platelet rather than propagating around it.

From this concept established by the above two material systems, such kind of reinforcement can then be added into any brittle matrices. Even when the reinforcement is reacted with the matrix to form a strong bonding, crack can still be deflected by the weak interface within the reinforcement and the brittle matrix can then be toughened.



3. Al₂O₃/Ti₃SiC₂ composite:

The concept of this study is successfully demonstrated from the above two model systems. Unfortunately, the limit of using the BaTiO₃ platelet is its ultra-large size (length > 500 μm). The Ti₃SiC₂ particles as the second model of reinforcement also exhibit lamellae structure. The toughening mechanisms were carefully investigated by microstructure observation, residual stress analysis and nano-indentation. The main toughening mechanism is attributed to crack deflection. The crack is deflected inside the Ti₃SiC₂ grain and induces pullouts within the lamellae structure when propagating

through the $\text{Al}_2\text{O}_3/\text{Ti}_3\text{SiC}_2$ interface. The residual stress on the interface can be treated as a minor reason of toughening. The energy absorbing (dissipating) ability of both materials in the composite hot-pressed at different temperature is also discussed. The composite prepared at higher temperature can absorb more fracture energy during fracture.

For the $\text{Al}_2\text{O}_3/\text{Ti}_3\text{SiC}_2$ composite, as a crack pops into a Ti_3SiC_2 particle within the Al_2O_3 matrix, the crack tends to change its direction and propagate along the long axis of the particle. The length of crack path is therefore long. The addition of 20 vol% Ti_3SiC_2 particles can enhance the toughness of Al_2O_3 by around 40%. From the theoretical calculation, the effective crack-deflection-induced pullouts during fracture can also be obtained. Since the ligament length and width of the elongated particle dominates the toughening effect, the suggestions of using this concept are the larger aspect ratio and the larger ligament width for any reinforcements with interlayers inside.

Chapter 7: Future Work

Although the study on toughening brittle ceramic by using reinforcements with weak interfaces was accomplished successfully in the present work, there are still some mysteries remained. Although the $\text{Al}_2\text{O}_3/\text{Ti}_3\text{SiC}_2$ composite is our most successful material system, further research is still needed. The recommended research direction will be:

1. Since the present study attributes the toughening mechanism to crack deflection, nanoindentation analysis on monolithic Ti_3SiC_2 and Ti_3SiC_2 in the composite offers information on the elastic/plastic transition point. It can offer an in-depth knowledge to the limit of crack formation within this kind of layered reinforcement. Moreover, a high elastic-to-plastic stress is beneficial for a cutting tool or other structural applications where high contact load are present. Therefore, a further research of elastic-to-plastic transition point is required.
2. The percolation threshold of $\text{Al}_2\text{O}_3/\text{Ti}_3\text{SiC}_2$ composite is in the range of 10~20 vol% of Ti_3SiC_2 addition. Since Ti_3SiC_2 is both thermal and electrical conductive, the thermal and electrical conductivities of the composite are required for further application. For example: the thermal conductive material for the welding torch is a possible area. The breakdown voltage test by DC or AC power can also exhibit

the reliability of this composite. A further research of the matrix/reinforcement interface and the internal layers within Ti_3SiC_2 by TEM is also beneficial.



References

1. G. Mayer, "Rigid Biological Systems as Models for Synthetic Composites," *Science*, 310 [5751] 1144-47 (2005).
2. C. Ortiz, M. C. Boyce, "Bioinspired Structural Materials," *Science*, 319 [5866] 1053-54 (2008).
3. E. Munch, M. E. Launey, D. H. Alsem, E. Saiz, A. P. Tomsia, R. O. Ritchie, "Tough, Bio-inspired Hybrid Materials," *Science*, 322 [5907] 1516-20 (2008).
4. L. J. Bonderer, A. R. Studart, L. J. Gauckler, "Bioinspired Design and Assembly of Platelet Reinforced Polymer Films Materials," *Science*, 319 [5866] 1069-73 (2008).
5. M. E. Launey, R. O. Ritchie, "On the Fracture Toughness of Advanced Materials," *Adv. Mater.* 21 [20] 2103-10 (2009).
6. H. Gao, B. Ji, I. Jaeger, E. Arzt, P. Frazl, "Materials Become Insensitive to Flaws at Nanoscale: Lessons from Nature," *Proc. Natl. Acad. Sci.* 100 [10] 5597-5600 (2003).
7. J. D. Hartgerink, E. Beniash, S. I. Stupp, "Self-Assembly and Mineralization of Peptide-Amphiphile Nanofibers," *Science* 294 [5547] 1684-88 (2001).
8. J. Aizenberg, "Crystallization in Patterns: A Bio-Inspired Approach," *Adv. Mater.*

- 16 [15] 1295-1302 (2004).
9. Z. Y. Tang, N. A. Kotov, S. Magonov, B. Ozturk, “Nanostructured Artificial Nacre,” *Nat. Mater.* 2, 413-18 (2003).
10. A. Sellinger, P. M. Weiss, A. Nguyen, Y. F. Lu, R. A. Assink, W. L. Gong, C. J. Brinker, “Continuous Self-Assembly of Organic–Inorganic Nanocomposite Coatings that Mimic Nacre,” *Nature* 394, 256-60 (1998).
11. P. Podsiadlo, A. K. Kaushik, E. M. Arruda, A. M. Waas, B. S. Shim, J. D. Xu, et al., “Ultrastrong and Stiff Layered Polymer Nanocomposites,” *Science* 318 [5847] 80-83 (2007).
12. M. E. Launey, E. Munch, D. H. Alsem, H. B. Barth, E. Saiz, A. P. Tomsia, R. O. Ritchie, “Designing Highly Toughened Hybrid Composites through Nature-Inspired Hierarchical Complexity,” *Acta Mater.* 57 [10] 2919-32 (2009).
13. S. Deville, E. Saiz, R. K. Nalla, A. P. Tomsia, “Freezing as a Path to Build Complex Composites,” *Science* 311 [5760] 515-18 (2006).
14. M. E. Launey, E. Munch, D. H. Alsem, E. Saiz, A. P. Tomsia, R. O. Ritchie, “A Novel Biomimetic Approach to the Design of High-Performance Ceramic–Metal Composites,” *J. R. Soc. Interface* 7 [46] 741-53 (2010).
15. A. G. Evans, “Perspective on the Development of High-Toughness Ceramics,” *J. Am. Ceram. Soc.* 73 [2] 187-206 (1990).

16. D. B. Marshall, "Strength Characteristics of Transformation-Toughened Zirconia," *J. Am. Ceram. Soc.* 69 [3] 173-80 (1986).
17. D. Shetty, J. Wang, "Crack Stability and Strength Distribution of Ceramics That Exhibit Rising Crack –Growth-Resistance [R-Curve] Behavior," *J. Am. Ceram. Soc.* 72 [7] 1158-62 (1989).
18. R. W. Rice, "Toughening in Ceramics Particulate and Whisker Composites," *Ceram. Eng. Sci. Proc.* 11 [7-8] 667-94 (1990).
19. G. Wei, P. Becher, "Improvement in Mechanical in SiC by the Addition of TiC Particulate," *J. Am. Ceram. Soc.* 67 [8] 571-91 (1984).
20. R. J. Damani, R. Gstrein, R. Danzer, "Critical Notch-Root Radius Effect in SENB-S Fracture Toughness Testing," *J. Eur. Ceram. Soc.* 16 [7] 695-96 (1996).
21. J. Kübler, "Bestimmung der Bruchzähigkeit keramischer Werkstoffe mit der SEVNB Methode: Resultate eines VAMAS/ESIS Ringversuches," in *Proceedings of the Werkstoff-woche, EMPA, Dubendorf, Switzerland* (1998).
22. J. Kübler, "Fracture Toughness of Ceramics Using the SEVNB Method: From a Preliminary Study to a Standard Test Method," in *Fracture Resistance Testing of Monolithic and Composite Brittle Materials*, ASTM STP 1409, J. A. Salem, M. G. Jenkins, and G. D. Quinn, eds., American Society for Testing and Materials, West Conshohocken, PA (2001).

23. D. Munz, T. Fett, "Mechanisches Verhalten keramischer Werkstoffe: Versagens-ablauf, Werkstoffauswahl, Dimensionierung," Springer-Verlag, Berlin (1989).
24. A. G. Evans, T. R. Wilshaw, "Quasi-Static Solid Particle Damage in Brittle Materials," *Acta Metall.* 24 [10] 939-56 (1976).
25. B. R. Lawn, "Fracture Mechanics of Ceramics," edited by R. C. Bradt, A. G. Evans, D. P. H. Hasselman and F. F. Lange (Plenum, New York, 1983) Vol. 5 p.1.
26. C. B. Ponton, R. D. Rawlings, "Vickers Indentation Fracture Toughness Test Part 1 Review of Literature and Formulation of Standardized Indentation Toughness Equations," *Mater. Sci. Tech.* 5, 865 (1989).
27. R. F. Cook, G. M. Pharr, "Direct Observation and Analysis of Indentation Cracking in Glasses and Ceramics," *J. Am. Ceram. Soc.* 73, 787 (1990).
28. M. Saikai, R. C. Bradt, "Fracture Toughness Testing of Brittle Materials," *Inter. Mater. Rev.* 38, 53 (1993).
29. A. G. Evans, E. A. Charles, "Fracture Toughness Determination by Indentation," *J. Am. Ceram. Soc.* 59 [7-8] 371-72 (1976).
30. I. C. Noyan, J. B. Cohen, *Residual Stress Measurement by Diffraction and Interpretation*, Springer-Verlag, NY (1987).
31. M. G. Jenkins, A. S. Kobayashi, K. W. White, R. C. Bradt, "Crack Initiation and

- Arrest in a SiC Whisker/ Al_2O_3 Matrix Composite,” J. Am. Ceram. Soc. 70 [6] 393-95 (1987).
32. Y. S. Chou, D. J. Green, “Silicon Carbide Platelet/Alumina composites: I, Effect of Forming Technique on Platelet Orientation,” J. Am. Ceram. Soc. 75 [12] 3346-52 (1992).
33. Y. S. Chou, D. J. Green, “Silicon Carbide Platelet/Alumina composites: II, Mechanical Properties,” J. Am. Ceram. Soc. 76 [6] 1452-58 (1993).
34. Y. S. Chou, D. J. Green, “Silicon Carbide Platelet/Alumina composites: III, Toughening Mechanisms,” J. Am. Ceram. Soc. 76 [8] 1985-92 (1993).
35. H. Cai, Z. Gui, L. Li, “Low-sintering Composite Multilayer Ceramic Capacitors with X7R Specification,” Mater. Sci. Eng. B 83 [1-3] 137-41 (2001).
36. H. Kishi, Y. Mizuno, H. Chazono, “Base-Metal Electrode-Multilayer Ceramic Capacitors: Past, Present and Future Perspectives,” Jpn. J. Appl. Phys., 42, 1-15 (2003).
37. J. D. Achenbach, “Wave Propagation in Elastic Solids,” American Elsevier Pub. Co. 1973.
38. T. Burgess, M. Ferry, “Nanoindentation of Metallic Glasses,” Materials Today 12 [1-2] 24-32 (2009).
39. S. C. Wang, Y. L. Chin, J. L. Huang, “Microstructure and Mechanical Properties

- of Hot-pressing Chromium Carbide/Alumina Nanocomposite Prepared by MOCVD in Fluidized Bed,” *J. Eur. Ceram. Soc.* 28 [9] 1909-16 (2008).
40. A. C. Dent, C. R. Bowen, R. Stevens, M. G. Cain, M. Stewart, “Effective Elastic Properties for Unpoled Barium Titanate,” *J. Eur. Ceram. Soc.* 27 [13-15] 3739-43 (2007).
41. W. H. Tuan, M. J. Lai, M. C. Lin, C. C. Chan, S. C. Chiu, “The Mechanical Performance of Alumina as a Function of Grain Size,” *Mater. Chem. and Phys.* 36 [3-4] 246-51 (1994).
42. Y. He, “Heat Capacity, Thermal Conductivity, and Thermal Expansion of Barium Titanate-based Ceramics,” *Thermochimica Acta* 419 [1-2] 135-41 (2004).
43. T. Fett, D. Munz, “Subcritical Crack Growth of Macrocracks in Alumina with R-Curve Behavior,” *J. Am. Ceram. Soc.* 75 [4] 958-63 (1992).
44. F. Rossignol, P. Goursat, J. L. Besson, P. Lespade, “Microstructure and Mechanical Behaviour of Self-Reinforced Si_3N_4 and Si_3N_4 -SiC Whisker Composites,” *J. Eur. Ceram. Soc.* 13 [4] 299-312 (1994).
45. A. G. Evans, K. T. Faber, “Crack-Growth Resistance of Microcracking Brittle Materials,” *J. Am. Ceram. Soc.* 67 [4] 255-60 (1984).
46. B. R. Lawn, A. G. Evans, “Elastic/Plastic Indentation Damage in Ceramics: The Median/Radial Crack System,” *J. Am. Ceram. Soc.* 63 [9-10] 574-81 (1980).

47. P. Chantikul, S. J. Bennison, B. R. Lawn, "Role of Grain Size in the Strength and R-Curve Properties of Alumina," *J. Am. Ceram. Soc.* 73 [8] 2419-27 (1990).
48. N. P. Padture, B. R. Lawn, "Toughness Properties of a Silicon Carbide with an In Situ Induced Heterogeneous Grain Structure," *J. Am. Ceram. Soc.* 77 [10] 2518-22 (1994).
49. P. L. Swanson, C. J. Fairbanks, B. R. Lawn, Y. W. Mai, B. J. Hockey, "Crack-Interface Grain Bridging as a Fracture Resistance Mechanism in Ceramics: I, Experimental Study on Alumina," *J. Am. Ceram. Soc.* 70 [4] 279-89 (1984).
50. H. Jantunen, A. Unsimäki, S. Leppävuori, R. Rautioaho, "Effect of Processing Route on Thermomechanical Properties of Low Temperature Firing Ceramic for Electronic Packaging," *Brit. Ceram. Trans.* 101, 22-24 (2002).
51. J. E. Gordon, *The New Science of Strong Materials*; 2nd Ed., Penguin Book, New York, 1976.
52. J. M. Molina-Aldareguia, J. Emmerlich, J-P. Palmquist, U. Jansson and L. Hultman, "Kink Formation around Indents in Laminated Ti_3SiC_2 Thin Films Studied in the Nanoscale," *Scripta Mater.* 49, 155-160 (2003).
53. Q. F. Zan, C. A. Wang, Y. Huang, S. K. Zhao, C. W. Li, "The Interface-Layer and Interface in the Al_2O_3/Ti_3SiC_2 Multilayer Composites Prepared by in situ Synthesis," *Mater. Lett.* 57, 3826-3832 (2003).

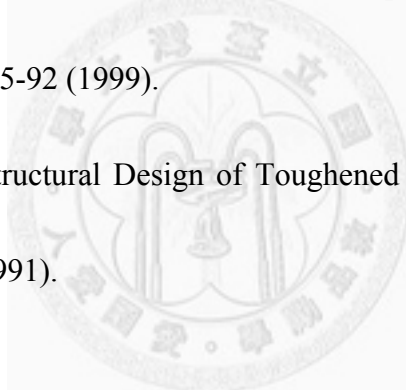
54. K. B. Alexander, P. F. Becher, X. L. Wang and C. H. Hsueh, "Internal Stresses and the Martensite Start Temperature in Alumina-Zirconia Composites: Effects of Composition and Microstructure," J. Am. Ceram. Soc. 78 [2] 291-296 (1995).
55. Y. M. Luo, S. Q. Li, J. Chen, R. G. Wang, J. Q. Li, and W. Pan, "Effect of Composition on Properties of Alumina/Titanium Silicon Carbide Composites," J. Am. Ceram. Soc. 85 [12] 3099 - 3101 (2002).
56. Y. M. Luo, W. Pan, S. Q. Li, R. G. Wang, and J. Q. Li, "Fabrication of Al₂O₃-Ti₃SiC₂ Composites and Mechanical Properties Evaluation," Mater. Lett. 57 [16-17] 2509-2514 (2003).
57. Y. M. Luo, S. Q. Li, J. Chen, R. G. Wang, J. Q. Li, W. Pan, "Preparation and Characterization of Al₂O₃-Ti₃SiC₂ Composites and Its Functionally Graded Materials," Mater. Res. Bull. 38 [1] 69-78 (2003).
58. D. Sarkar, B. Basu, M. C. Chu, S, J. Cho, "R-curve Behavior of Ti₃SiC₂," Ceram. Int. 33 [5] 789-93 (2007).
59. C. Racault, F. Langlais, and R. Naslain, "Solid-State Synthesis and Characterization of the Ternary Phase Ti₃SiC₂," J. Mater. Sci. 29 [13] 3384-92 (1994).
60. J. Lis, Y. Miyamoto, R. Pampuch, and K. Tanihata, "Ti₃SiC₂-Based Materials Prepared by HIP-SHS Techniques," Mater. Lett. 22 [3-4] 163-68 (1995).

61. T. Okano, T. Yano, and T. Iseki, "Synthesis and Mechanical Properties of Ti_3SiC_2 Ceramic," *Trans. Met. Soc. Jpn.*, 14A, 597 (1993).
62. JCPDS, PDF number: 035-0804.
63. M. F. Ashby, F. J. Blunt, M. Bannister, "Flow Characteristics of Highly Constrained Metal Wires," *Acta Metall.* 37 [7] 1847-57 (1989).
64. W. C. Oliver and G. M. Pharr, "An Improved Technique for Determining Hardness and Elastic Modulus Using Load and Displacement Sensing Indentation Experiments," *J. Mater. Res.* 7 [6] 1564-1583 (1992).
65. J. Kübler, Fracture Toughness of Ceramics Using the SEVNB Method: From a Preliminary Study to a Standard Test method. In: J. A. Salem, M. G. Jenkins, G. D. Quinn Editors. *Fracture Resistance Testing of Monolithic and Composite Brittle Materials*. West, Conshohocken, PA: American Society for Testing and Materials; 2002, p. 93-106 [ASTM STP 1409].
66. T. Fett, D. Munz, *Stress Intensity Factors and Weight Functions*. Southampton: Computational Mechanics Publications; 1997, p. 107-108.
67. H. Jelitto, F. Felten, M. V. Swain, H. Balke, G. A. Schneider, "Measurement of the Total Energy Release Rate for Cracks in PZT Under Combined Mechanical and Electrical Loading," *J. Appl. Mech.* 74, 1197-1211 (2007).

68. T. Fett , S. Fünfschilling, M. J. Hoffmann, R. Oberacker, H. Jelitto, G. A. Schneider, “R-Curve Determination for the Initial Stage of Crack Extension in Si_3N_4 ,” J. Am. Ceram. Soc. 91 [11] 3638-42 (2008).
69. H. Özcoban, H. Jelitto, G. A. Schneider, “Influence of Finite Notch Root Radius and Optically Determined Crack Length on the Measured Fracture Toughness of Brittle Materials,” J. Eur. Ceram. Soc. 30 [7] 1579-83 (2010).
70. T. Fett, “Influence of a Finite Notch Root Radius on Fracture Toughness,” J. Eur. Ceram. Soc. 25 [5] 543-7 (2005).
71. T. Fett, D. Munz, G. Thun, “Evaluation of Bridging Parameters in Aluminas From R-Curve by Use of the Fracture Mechanical Weight Function,” J. Am. Ceram. Soc. 78 [4] 949-51 (1995).
72. J. Seidel, J. Roedel, “Measurement of Crack-Tip Toughness in Alumina as a Function of Grain Size,” J. Am. Ceram. Soc. 80 [2] 433-8 (1997).
73. K. Niihara, “New Design Concept of Structural Ceramics-Ceramic Nanocomposite,” J. Ceram. Soc. Jpn. 99 [10] 974-982 (1991).
74. S. Jiao, M. L. Jenkins and R. W. Davidge, “Interfacial Fracture Energy-Mechanical Behaviour Relationship in $\text{Al}_2\text{O}_3/\text{SiC}$ and $\text{Al}_2\text{O}_3/\text{TiN}$ Nanocomposites,” Acta Mater. 45 [1] 149-156 (1997).

75. R. S. Lima and C. P. Bergmann, Structural Changes on Post-sintered Flame Sprayed Alumina and Alumina-Titania, in: C. C. Berndt, S. Sampath (Eds.), Proc. 8th Nat. Thermal Spray conference, September 11-15, Advances in Thermal Spray Science and Technology, ASM, 1995.
76. M. W. Barsoum, T. Zhen, S. R. Kalidindi, M. Radovic, and A. Murugaiah, "Fully Reversible, Dislocation-Based Compressive Deformation of Ti_3SiC_2 to 1 GPa," Nat. Mater. 2, 107-111 (2003).
77. S. Rattanachan, Y. Miyashita and Y. Mutoh, "Microstructure and Fracture Toughness of a Spark Plasma Sintered Al_2O_3 -Based Composite with $BaTiO_3$ Particulates," J. Eur. Ceram. Soc. 23, 1269-76 (2003).
78. G. Wotting, B. Kanka, G. Ziegler, Non-oxide Technical and Engineering Ceramics, ed. by S. Hampshire, Elsevier Applied Sci., London, 1986, pp. 83.
79. K. T. Faber, A. G. Evans, "Crack Deflection Processes--I. Theory," Acta Metall. 31 [4] 565-76 (1983).
80. K. T. Faber, A. G. Evans, "Crack Deflection Processes--II. Experiment," Acta Metall. 31 [4] 577-84 (1983).
81. B. J. Kooi, R. J. Poppen, N. J. M. Carvalho, J. Th. M. De Hosson, M. W. Barsoum, " Ti_3SiC_2 : A Damage Tolerant Ceramic Studied with Nanoindentations and Transmission Electron Microscopy," Acta Mater. 51, 2859-72 (2003).

82. I. M. Low, "Vickers Contact Damage of Micro-layered Ti_3SiC_2 ," J. Eur. Ceram. Soc. 18 [6] 709 - 713 (1998).
83. A. Murugaiah, M. W. Barsoum, S. R. Kalidindi, T. Zhen, "Spherical Nanoindentations and Kink Bands in Ti_3SiC_2 ," J. Mater. Res. 19 [4] 1139-48 (2004).
84. J. L. Loubet, J. M. Georges, O. Marchesini, G. Meille, "Vickers Indentation Curves of Magnesium Oxide (MgO)," J. Tribol. 106 [1] 43-48 (1984).
85. N. F. Gao, Y. Miyamoto, D. Zhang, "Dense Ti_3SiC_2 prepared by reactive HIP," J. Mater. Sci. 34 [18] 4385-92 (1999).
86. P. F. Becher, "Microstructural Design of Toughened Ceramics," J. Am. Ceram. Soc. 74 [2] 255-269 (1991).



Curriculum Vitae

Personal Data

Name: Yuan-Liang Chin (靳元良)

Gender: Male

Hometown: Taipei, Taiwan (R.O.C.)

Date of Birth: 03 Sep. 1980

E-Mail: d94527004@ntu.edu.tw

Education Background

09.2005~03.2011: Ph.D., Dept. of Materials Science and Engineering, National Taiwan University, Taipei, Taiwan.

09.2003~07.2005: M.Sc., Dept. of Materials Science and Engineering, National Cheng Kung University, Tainan, Taiwan.

09.1999~06.2003: B.Sc., Dept. of Materials Science and Engineering, National Cheng Kung University, Tainan, Taiwan.

Publication List

Journal Papers

1. Sheng-Chang Wang, **Yuan-Liang Chin**, Jow-Lay Huang, "Microstructure and mechanical properties of hot-pressing chromium carbide/alumina nanocomposite prepared by MOCVD in fluidized bed," *J. Eur. Ceram. Soc.*, 28 (9) 1909 - 16 (2008).
2. **Yuan-Liang Chin**, Wei-Hsing Tuan, Jow-Lay Huang, Chang-An Wang, "Toughening alumina with layered Ti_3SiC_2 inclusions," *J. Alloys Compd.*, 491, 477 - 82 (2010).
3. **Yuan-Liang Chin**, Wei-Hsing Tuan, "Feasibility of using multilayer platelet as toughening agent," *Materials*, 3(1) 1 - 8 (2010).
4. **Yuan-Liang Chin**, Wei-Hsing Tuan, "Contribution of plastic deformation of Ti_3SiC_2 to the crack deflection in the Al_2O_3/Ti_3SiC_2 composites," *Mater. Sci. Eng. A*, 528 (7-8) 3270 - 74 (2011).

5. Wei-Hsing Tuan, Ya-Jen Yu, **Yuan-Liang Chin**, “From biomimetic concept to engineering reality - a case study on the design of ceramic reinforcement,” *Adv. Eng. Mater.* (2010) In press.
6. **Yuan-Liang Chin**, Wei-Hsing Tuan, “Crack extension resistance behaviour in lamellae inclusions toughened ceramic-matrix composite,” in preparation.
7. **Yuan-Liang Chin**, Hüseyin Özcoban, Gerold A. Schneider, Wei-Hsing Tuan, “Influence on crack-deflection-induced pullouts to the toughening mechanism in MAX-phase incorporated composite”, in preparation.

Conference Papers

1. **Yuan-Liang Chin**, Hao-Tung Lin, Sheng-Chang Wang, Jow-Lay Huang, “Microstructure and mechanical properties of hot-pressing chromium carbide/alumina nanocomposite prepared by MOCVD in fluidized bed,” Annual Meeting of Taiwan Ceramic Society, Tainan, Taiwan (2005).
2. **Yuan-Liang Chin**, Wei-Hsing Tuan, “A New Concept on Toughening Ceramic through the Addition of Weak Inclusions.” 2nd International Congress on Ceramic (ICC2), Verona, Italy (2008).
3. **Yuan-Liang Chin**, Wei-Hsing Tuan, “Feasibility of using multilayer platelet as toughening agent,” Annual Meeting of Taiwan Ceramic Society, Taipei, Taiwan (2009).

Writings

1. **Yuan-Liang Chin**, Wei-Hsing Tuan, Use of MAX particles to improve the toughness of brittle ceramics, a book chapter of *Advances in Science & Technology of $M_{n+1}AX_n$ Phases*, Woodhead Publishing Ltd., Cambridge, UK, to be published in 2011.

Patent

1. Jow-Lay Huang, Shang-Nan Chou, **Yuan-Liang Chin**, Chi-Feng Liu, “COMPOSITE CERAMICS AND METHOD OF PREPARING THE SAME,” accepted in Taiwan (93-009-SP-1239-TW), Japan and USA (093137419) in 2005.